ABSTRACT

The Effects of Fiber Orientation on Stiffness and Thermal Expansion of Large Volume, Anisotropic, Short-Fiber, Composite Material Fabricated by Fused Filament Fabrication

Timothy D. Russell, M.S.M.E.

Mentor: David A. Jack, Ph.D.

Fused Filament Fabrication (FFF) is a rapidly improving 3D printing technology that can be used for manufacturing complex parts. The properties of these parts can be improved by adding short-fibers to the polymer feedstock. The fiber orientation state is critical to know in order to determine the final material properties though. This study investigates the reasonableness of several fiber orientation models based on their use in predicting the effective longitudinal Young's modulus E_{22} and CTE α_{22} of a large volume, short-fiber composite, FFF printed bead. Comparisons are made between computational results from MATLAB (MathWorks, Inc., Natick, MA) and COMSOL Multiphysics (Stockholm, Sweden) to experimental results from samples collected from beads fabricated with an in-house, large scale bead deposition system. Based on comparisons of the computational and experimental results for E_{22} and α_{22}, the Reduced Strain Closure (RSC) model [1] with $\frac{1}{30} \leq \kappa \leq \frac{1}{5}$ seems to be the most reasonable.

The Effects of Fiber Orientation on Stiffness and Thermal Expansion of Large Volume, Anisotropic, Short-Fiber, Composite Material Fabricated by Fused Filament Fabrication

by

Timothy D. Russell, B.S.

A Thesis

Approved by the Department of Mechanical Engineering

_____

Douglas E. Smith, Ph.D., Chairperson

Submitted to the Graduate Faculty of
Baylor University in Partial Fulfillment of the
Requirements for the Degree
of

Master of Science in Mechanical Engineering

Approved by the Thesis Committee

_____

David A. Jack, Ph.D., Chairperson

_____

Douglas E. Smith, Ph.D.

_____

Ronald B. Morgan, Ph.D.

Accepted by the Graduate School

December 2017

_____

J. Larry Lyon, Ph.D., Dean

Page bearing signatures is kept on file in the Graduate School.

TABLE OF CONTENTS

LIST OF FIGURES

LIST OF TABLES

ACKNOWLEDGMENTS

First of all, I would like to thank my advisor Dr. David Jack for the huge role he has played in my education. I don't think I'll ever forget the wonderful times I had in Boy Scouts with him and his wife Trisha when he was my Scoutmaster. His belief in me throughout my master's studies has been a huge encouragement to me to say the least. I am also grateful for his MATLAB codes that have helped me accomplish this thesis.

I thank my parents for raising me, for loving me, for working hard to make sure I got a good education, and most of all for teaching me to fear and love the Lord.

I thank my teachers and fellow graduate students. Special thanks goes to Dr. Douglas E. Smith for giving me a second chance when I needed it, and to my colleagues at the BRIC who helped me so much. Special thanks to Dale Jiang for all of his MATLAB help and Daniel Pulipati for helping build the translation bed of the large scale, bead deposition system used in this research.

I thank HapCo Inc. (Hewitt, TX) for donating the large scale extruder used in this study and PolyOne (Avon Lake, OH) for donating the carbon fiber filled ABS used in this study.

I also thank Dr. David Jack, Dr. Douglas Smith, and Dr. Ronald Morgan for serving on my committee and giving me valuable feedback.

Finally, I would like to thank my Lord and Savior Jesus Christ who changed my life and brought it meaning. I never could have done this without Him.

DEDICATION

To my parents, Bradford and Ann Russell.

CHAPTER ONE

Introduction

For the past several decades, injection molding and compression molding have been used to effectively mass produce parts. More recently however, advances have been made in the development of additive manufacturing (AM) methods. Additive manufacturing, also called 3D printing, is defined by Wohlers Associates as "the process of joining materials to make objects from 3D model data, usually layer upon layer, as opposed to subtractive manufacturing methodologies" [2]. With these advances there is a desire to incorporate chopped fibers within the polymer extrudate to enhance the structural performance of the manufactured parts. Although AM has not caught up to the speed of injection and compression molding when it comes to mass production, there is considerable knowledge that can be transferred from the traditional, existing technologies to the newer 3D printing technology. One of the advantages of 3D printing of unique interest in the present context is the use of 3D printing to produce a new part independent of a mold. This gives additive manufacturing the potential advantage to be more efficient and less costly in the initial phase of manufacturing or in situations where small scale production numbers are desired.

3D printing is often times less wasteful of material than other manufacturing techniques. It is termed an additive manufacturing process as opposed to a subtractive manufacturing process, meaning that material is built up, often with a

layer-by-layer technique, as opposed to starting with a larger volume of material and removing/trimming away the excess as is done in milling. This additive manufacturing process with the absence of a mold has an advantage in that it allows for the making of complex three-dimensional parts that injection and compression molding methods could not. Because of its unique abilities, 3D printing has been exploited in the past as a method of rapid prototyping.

However, with the inclusion of fiber reinforcements, additively manufactured parts can move beyond that of prototypes and may have potential to be structural members, and thus could displace applications where injection and compression molding have dominated. Developers are now looking to be able to use 3D printing for producing functional parts approved for such items as aircraft and automobiles. It is also desirable that 3D printing, which has mainly been used for small scale parts on the order of inches or centimeters, to be able to be used for manufacturing large scale parts on the order of feet or meters. However, in order to do this more effectively and efficiently, the processing of 3D printed parts must be better understood, with specific interest given to the final part performance. Knowledge of the best parameters to use to make a certain part must be gained and improved in order to cut back on time and cost.

One issue to be addressed for large scale 3D printing is how to improve the material properties of a final part. Carbon fiber polymer composites have the potential to displace metallic structures in some applications, due to their high strength to low weight ratios, once the structural behavior of processed composite parts are understood. Mixing fibers within a polymer matrix and imposing a

preferential fiber orientation may give one the ability to produce a composite with superior mechanical ability. Jiang [3] showed that the addition of carbon fibers to several different polymers, including ABS, could increase the strength and modulus of small scale 3D printed parts. In addition, Jiang found that these properties, in general, increased the most in the print direction.

The addition of carbon fibers to the ABS feedstock will also effect other properties of a 3D printed part, such as the thermal properties. Love *et al.* [4] demonstrated that for small scale 3D printing with ABS, the addition of carbon fibers into the ABS can significantly increase stiffness and strength properties, but also that the addition of the carbon fibers could increase thermal conductivity and decrease CTE, thereby helping reduce thermal gradients and strain in the 3D printed parts and, subsequently, the distortion and warpage [4]. It is important to understand how the processing of 3D printed parts affects material properties, such as stiffness and CTE, so that parts can be designed both effectively and efficiently. This is a complicated task since adding short-fibers to a polymer build material will give the resulting composite part anisotropic material properties if there is even a slight directional bias in the fiber orientation state.

1.1 Problem Statement

The goal of this thesis is to predict the effective longitudinal Young's modulus and CTE of an extrudate of carbon fiber reinforced ABS. The demonstration of the effectiveness of the predicted results is provided through a comparison of the experimentally characterized effective longitudinal Young's modulus and effective

longitudinal CTE of a single, short-fiber composite bead fabricated with an in-house, large volume, bead deposition system.

To successfully predict the final part stiffness and CTE values, the final fiber orientation state within the part must be accurately predicted and multiple fiber interaction models are investigated along with variations of their empirical parameters. The fiber orientation states determined at the nozzle exit are assumed to be the fiber orientation states of the final, printed bead across its width. This assumption means that no die swell of the polymer coming out of the nozzle is taken into account. This assumption is not completely valid, but will be made in this study for the purposes of simplifying the computational methods. A future study could incorporate the die swell for more accurate results. For this study, this assumption that the die swell can be neglected leads to the fact that the predicted fiber orientation state does not vary along the length of the final bead, but only along the width. Once the spatially varying fiber orientation state within the bead is known, the spatially varying stiffness and CTE tensors, which are functions of the fiber orientation state, are computed. A simulation in COMSOL Multiphysics using the newly found stiffness and CTE property tensors, is then performed to find the effective longitudinal Young's modulus and CTE of the printed bead. These calculated values are then compared with experimentally determined values to assess the accuracy of the mathematical methods used to make the predictions and the results are in reasonable agreement between the model predictions and the experimental characterization.

1.2 Thesis Overview

This thesis has five chapters. In Chapter Two a review of literature relevant to this study will be covered. Chapter Two will cover the background of 3D printing, the necessary information regarding fiber orientation modeling along with a discussion of multiple fiber interaction models, and the calculation of the stiffness and CTE tensors. Chapter Three discusses the implementation of some of the mathematical models described in Chapter Two. It covers the computational methods used to calculate the fiber orientation state, the stiffness and CTE tensors, and finally, the effective longitudinal Young's modulus and effective longitudinal CTE of a short-fiber composite, large volume, 3D printed bead. Chapter Four explains the experimental methods used. An in-house large scale, bead deposition system was developed during this research effort and was used for the fabrication of the 3D printed beads. Chapter Four presents and discusses the tensile test results and the thermomechanical analyzer (TMA) machine results to obtain, respectively, the effective longitudinal Young's modulus and CTE from samples cut from the beads. Chapter Four culminates with a comparison between the experimental and the modeling predictions for the longitudinal stiffness and CTE values and the results are within, respectively, 5.1% and 16.5% of each other for the best model. Chapter Five then concludes the thesis and discusses potential future work.

CHAPTER TWO

Literature Review

Understanding the relationship between the internal fiber microstructure and the resulting processed 3D printed part requires coupling knowledge of the fast paced field of additive manufacturing and the foundational research in short-fiber reinforced composites. This chapter focuses on two main topics, the background information on 3D printing, sometimes called Additive Manufacturing (AM), and the foundations for the mathematical analysis of fiber orientation modeling during the polymer melt flow along with the resulting processed part performance. There are several categories of 3D printing and Fused Filament Fabrication (FFF) is the focus of the present efforts in this thesis. Specifically, this work focuses on Big Area Additive Manufacturing (BAAM) which is often considered as a FFF process on a size scale that makes fiber reinforcement practical. As the technology currently stands, the BAAM process is being considered for utilization in processed parts up to the size scale of a complete automobile. When it comes to modeling the fiber orientation state within a polymer flow in the BAAM printer nozzle, also referred to as the extruder tip, the foundational model is Jeffery's equation. Jeffery's equation is fundamental in understanding the motion of a single fiber suspended in a polymer flow, a dilute suspension. However, the Jeffery model needs to be expanded upon as the suspension transitions from dilute and non-interacting fibers to a concentrated suspension with fiber interaction. Once the fiber orientation state at a coordinate location within a sample is derived from an appropriate fiber orientation kinematics model, the

stiffness and thermal expansion tensors can be calculated as functions of the orientation state at the same locations as well. This will lead to spatially varying, and often monoclinic, stiffness and thermal expansion tensors. Thus to fully understand the impact of the fiber motion during the melt flow, an additional post processing step, such as a finite element thermal and/or structural analysis, is required to properly relate the final part behavior to that of the processing conditions.

2.1 Background of 3D Printing

In the following section, the current trends in the 3D printing market will be covered, followed by applications, types of 3D printers, and structural property limitations of 3D printed parts. Particular attention will be paid to the Big Area Additive Manufacturing process and the associated extrudate swell problem as this plays an important role within the resulting fiber orientation state and thus the part performance.

2.1.1 The Trends in the 3D printing Market

The 3D printing industry has grown significantly over the past several years. Patents on some of the early 3D printer parts and processes have expired, which has helped lead to a boom in many new companies [5]. According to the Wohlers Report of 2017 as cited in [6,7], there were 49 AM system companies manufacturing and selling in 2014, 62 in 2015, and 97 in 2016. Also according to the 2017 Wohlers Report as cited in [6,7], although the 3D printing industry's worldwide revenue growth dipped from 25.9% in 2015, it still grew at a rate of 17.4% in 2016. The Wohlers Report is considered by many to be a very reputable source on 3D printing. This annual report is so respected that some have called it a "bible" on AM that virtually covers everything to do with the

industry: applications, history, market trends, underlying technology, advancements in the last year, etc. [6,7].

2.1.2 Applications of 3D Printing

There are a wide range of reasons for the increasing use of 3D printing, with the most significant being efficiency, cost, and the breadth of applications. The 3D printing process of polymers often does not require the use of a mold, whereas many traditional manufacturing methods such as injection and compression molding do. The design process can often be performed without the use of a dedicated fabricator by creating a design using a computer aided design (CAD) package and then directly uploading the digital file to the 3D printer. This not only cuts down on the time required to take an idea for a part from conception to fabrication, but also cuts down on cost due to reduced tooling and personnel. This is why for the past several decades, 3D printing has been a valuable method for "rapid prototyping." However, industries are broadening their mindset to consider using 3D printing for more than prototyping purposes. The technology has advanced to a point where industries can produce functional parts via 3D printing. Some of the biggest industries that have transitioned part of their manufacturing process over to 3D printing are the automotive, aerospace, and medical industries [8].

One of the reasons 3D printing is appealing to the automotive and aerospace industries is that making light weight parts while maintaining high mechanical ability is very important. 3D printing enables people to manufacture topology optimized structures much more easily than traditional manufacturing methods (see e. g., [3,9]). Topology optimization is a method of determining the optimal structure given a certain structural domain, knowledge of the loads, support conditions, and the volume of material to be

used as well as any other constraints that may be specific to the desired part [10]. Many topology optimized parts are so complex that they are extremely hard or virtually impossible to manufacture using traditional molding techniques. However, 3D printing is not stopped by this since it does not require a mold and can be used to print very intricate parts. In addition, topology optimization algorithms can be relatively simple to code as shown by O. Sigmund who wrote one in only 99 lines using MATLAB [11]. Hoglund [9] and Jiang [3] established, respectively, a 2D and 3D topology optimization procedure for parts formed using fiber reinforce 3D filament. Not only does 3D printing allow unique interior cavities within a structure, but Hoglund and Jiang demonstrated that the increased material anisotropy observed in fiber reinforced filament allows for additional design features to further reduce the structure's load carrying capacity. A unique feature of Hoglund's and Jiang's subsequent work is the ability to incorporate the print path, and thus the direction of material anisotropy, within the topological optimization algorithms.

The ability to manufacture topology optimized parts and make them out of a material with high mechanical properties is helping the 3D printing industry transition from being used exclusively for prototyping to that of producing functional load-bearing parts. In the past few years, the 3D printing industry has developed to a point where the manufacturing of purposeful load-bearing parts has already become a reality. For example, recently, multiple flight-approved parts have been developed for a satellite using 3D printing and topology optimization in as little as 8 weeks [12].

In the field of medicine, 3D printing has been used to make replicas of internal body parts based on imaging data for educational purposes or for surgical planning (see e.g., [9]). 3D printing has also been used to make prosthetics (see e.g., [4]) and even used

in tissue engineering where 3D printed implants that have cells in them allow the printed parts to combine with a human body over time (see e.g., [8,13]). Hearing aids and Invisalign, which are patient-specific, have also benefitted from the AM technique [8]. The field of dentistry is a prime candidate for dramatic growth in 3D printing since it requires the manufacturing of patient-specific parts [5].

2.1.3 Types of 3D Printers

When it comes to the types of 3D printers in existence, there are several. Most of these involve building a 3D structure using a layer by layer technique either by curing the build material with an ultra violet laser, fusing the build material with a CO_2 laser, or by extruding a molten material that solidifies during cooling to ambient conditions. Some of the types include a stereolithography apparatus (SLA), digital light projection (DLP), continuous liquid interface production (CLIP), selective laser sintering (SLS), selective heat sintering (SHS), Fused Filament Fabrication (FFF), and laminated object manufacturing (LOM) (see e.g., [5]). SLA 3D printing is where 3D printing got its start commercially in 1986 with 3D Systems [5]. This type of 3D printing involves a liquid resin that is cured by a concentrated ultraviolet laser [5]. It was 3D Systems that invented the Standard Tessellation Language file (.STL file) that is so commonly required by other 3D printers nowadays for storing a part's design data [5]. In addition to SLA, DLP printers are able to cure a whole layer of liquid resin build material at once making them faster than SLA [5]. CLIP printers are also very fast and they use a continuous cure method as opposed to the common layer by layer technique [5]. SLS and SHS involve melting the build material and fusing it together layer by layer [5]. FFF, one of the most common types of 3D printing in industry and in the past few years for home use, involves

extruding molten polymer through a nozzle onto a build platform layer by layer. There is much that can be said about the different types of 3D printing and the advances in the technology that have been made. This thesis will focus on a variant of the FFF process known as Big Area Additive Manufacturing (BAAM). The BAAM process moves the commonly employed FFF process to the large scale, with typical deposited beads growing from the sub millimeter scale to length scales over 10 mm. This larger length scale allows for the incorporation of fiber reinforcements to enhance the structural and thermal properties, and allows for the production of large scale production products.

2.1.4 Materials Used in 3D Printing

3D printing is a viable manufacturing process for many different types of materials including metals, composites, polymers, and even organic matter. It has been shown that 3D printing of metal parts is a viable option for many scenarios, such as for aerospace components [12]. Biocomposites have also been successfully printed and could be used in more aesthetic roles such as for car components [14], but they are not a good candidate for structural parts due to their limited ability to carry loads. Polymers without reinforcements have great impact and dampening abilities, but they are not viable candidates for load bearing applications due to the inherent inability of polymers to support large loads per unit mass. Although 3D printing provides good opportunities for prototyping, when it comes to manufacturing parts that are capable of carrying loads, the present day options relying on 3D printing as a primary production method are limited.

Materials that are capable of withstanding loads must be used in order for 3D printing to seriously be considered as a means for producing functional parts. In addition to metal parts, an exciting development in 3D printing is that of printing composite

materials. A composite material is a material that is made up of “two or more materials [that] are combined on a macroscopic scale to form a useful third material” [15]. Composite materials by themselves are a topic of intense research interest at the present for a wide range of industries due to their high strength to weight ratios. They come in different types including laminated, fibrous, particulate, and different combinations of these three (see e.g., [15]). As Robert M. Jones put it in his book on composite materials, “The advantage of composite materials is that, if well designed, they usually exhibit the best qualities of their components or constituents and often some qualities that neither constituent possesses” [15]. The design permutations with composites are seemingly endless, and the final produced product can be made according to the specific characteristics that are desired for the application. In many instances composite materials can be designed to outperform even metals in terms of strength to weight or stiffness to weight ratio (see e.g., [11]). Jones also stated, “composite materials can be made that have the same strength and stiffness as high-strength steel, yet are 70% lighter! Other advanced composite materials are as much as three times as strong as aluminum, the common aircraft structural material, yet weigh only 60% as much! Moreover…composite materials can be tailored to efficiently meet design requirements of strength, stiffness, and other parameters, all in various directions” [15]. This ability to tailor a composite’s properties in a directional sense is important. In this way, a fibrous composite material, for example, could be designed so that it does not have to “waste” its strength in non-loaded directions (as isotropic metals do) and have maximum strength in the direction of maximum load.

With all of this being said, between metals and polymer composites there is potential for 3D printing to be used to manufacture useful parts that can actually stand loads. This thesis is focused on 3D printed short fiber composite materials and some of their directionally dependent properties. The directionally dependent properties of stiffness and coefficient of thermal expansion will be inspected closely in Chapter Three.

2.1.5 Big Area Additive Manufacturing

Common Fused Filament Fabrication (FFF) printers have found many applications in industries that need the fabrication of small parts, but the effectiveness for large-scale parts or load bearing parts is prohibitive due to the time required for printing. This is where large volume FFF known as Big Area Additive Manufacturing (BAAM) comes into the industrial scene.

In the past, 3D printing has had size limitations for the parts that can be manufactured. Many small scale 3D printers are limited to the size of their build chamber which is usually on the order of inches or sometimes feet. The BAAM configuration, however, is not restricted to any build chamber and is not limited to only one extruder either [16]. BAAM is designed for allowing multiple extruders that are secured to robotic arms in the open air [16]. This allows the volume capability to be virtually “unbounded” since it is not dependent on a build chamber of prescribed dimensions or on a set number of extruders with limited movement capability [16]. Attaching a BAAM extruder to an enclosed, x-y-z translation system is also feasible too though [16].

Cincinnati Incorporated is the leading company in the BAAM industry and uses enclosed BAAM systems. A comparison of the size of small-scale printers to enclosed BAAM printers can be found by looking at 3dhubs.com and Cincinnati Inc.’s website.

The top 3D printers for professionals for 2017, as given by 3dhubs.com, were the Ultimaker 2+, Form 2, and Zortrax M200 (made by Ultimaker, Formlabs, and Zortrax, respectively) [17]. The biggest of these is the Ultimaker 2+ which has a build volume of 223 x 223 x 205 mm (8.78 x 8.78 x 8.07 in) [17]. On the other hand, the largest BAAM printer produced by Cincinnati Inc. (Harrison, OH) in partnership with Oak Ridge National Laboratory (Oak Ridge, TN) has a build volume of 240 x 90 x 72 in [18]. This yields a build volume nearly 2500 times larger than that of the Ultimaker 2+. As another comparison, the amount of material deposited for an average small-scale 3D printer is about 0.01-0.081 kg/hr (0.0220-0.1786 lbs/hr), whereas BAAM systems created by Oak Ridge National Laboratory (ORNL) and Cincinnati Inc. can deposit material at a rate of 5-50 kg/hr (11-110 lbs/hr) [19]. This means they can deposit about 600 times more material per hour than a typical small scale printer in terms of weight.

BAAM is also welcoming to composite materials and metals and does not require them to be processed into spools of filament [16]. Instead, raw material pellets and other additives can be fed directly into a BAAM extruder system [16]. The ability to print composite materials and metals is, of course, advantageous for building load-bearing parts.

The effectiveness of the BAAM process has been demonstrated through several automotive platforms. Of note are the full size Strati car, a Shelby Cobra, a kayak, a utility vehicle, an excavator cab, and replicas of an F-22 Raptor and Orion Spacecraft [5,19,20].

The progress in the BAAM technology has been significant and fast-paced, however, just as is the case with small-scale 3D printing, there exist many challenges that

must be overcome. Spinnie has addressed the effects of processing parameters on large scale bead deposition [21,22], but the trial and error methodology to determine the optimal parameters for the manufacturing of a part is not as economical with BAAM printers (since they would waste a lot of material) as it is with small-scale printers. It is desirable that computational methods be developed to predict the thermal and mechanical properties of fiber reinforced BAAM parts [19], and it is this last point that formulates the primary objective of this thesis. The computational techniques used in this thesis for the large scale bead deposition system are a step towards computational techniques to be applied to actual BAAM systems in the future.

2.1.6 Extrudate Swell in FFF

An issue that has not been fully addressed within the literature is that of the swell of the extrudate as it exits the nozzle of the printer. This will happen for small and large scale FFF, and will have a significant impact both on the deposited bead upon the platform and, in the present context, the internal fiber orientation state [23]. The extrudate swell must be considered if high accuracy is desired in the fiber orientation calculations.

According to Heller[23], although multiple people have considered extrudate swell problems in fields outside of the FFF process, the extrudate swell problem in FFF had not been addressed. Yet including the effects on the velocity field due to the swell does have a significant impact upon the fiber orientation state within the polymer flow [23]. This altered fiber orientation state will have an impact on the final structural and thermal properties of the printed bead. Heller *et al.*, in a journal paper more recent than Heller's thesis, extended his thesis work to include structural property predictions [24] and for the present work, both structural and thermal properties will be addressed. For his

thesis, Heller made an axisymmetric model of the nozzle/extrudate swell problem in COMSOL Multiphysics, where the boundaries of the flow domain were the inner dimensions of the nozzle and the surface of the extrudate swell was defined by a polynomial. The model was axisymmetric and cylindrical coordinates were used. Thus the surface of the die swell could be represented by a 2 dimensional curve. The nozzle was defined as a "no-slip" boundary whereas the surface of the extrudate swell, which in reality would be exposed to the open air, was defined as a no stress boundary. Heller's work was for small scale FFF systems using Newtonian fluids and he did not provide experimental validation.

Heller desired to find the proper shape of the extrudate swell using an optimization technique. Although the shape of the extrudate swell looked like it could potentially be represented by an exponential function, Heller found that a 4^{th} order polynomial gave better results. The correct shape of the extrudate swell should, in theory, allow both the normal and shear stresses on the surface of the extrudate swell to be zero since the extrudate swell is in open air. Thus an optimization algorithm was used to minimize the stress state on the surface of the extrudate swell by altering the shape of the polynomial.

The optimization algorithm chosen for the purpose of minimizing the extrudate swell surface stress was MATLAB's `fmincon` function. This function takes as inputs an objective function to be minimized, design variables, which are the variables that are allowed to change (for this case these variables would define the shape of the extrudate swell), information regarding constraints on the design variables, and additional options a user may want to specify. Using an iterative process, this function can then output the

minimum (the optimized) objective function value and the design variables that produced it. Heller linked COMSOL and MATLAB via LiveLink. This way the optimized shape of the extrudate swell could be calculated in MATLAB and automatically accepted by COMSOL with no need for manually entering the updated geometry in COMSOL. Then COMSOL could use this newly found shape and do a finite element analysis on the flow domain and calculate the surface stress of the extrudate swell. This process was continued until the stress state was minimized across the extrudate swell surface. There were some small singularity issues that prevented Heller from obtaining a zero stress state, but these occurred at the corner elements at the interface between the wall, the fluid, and the zero-stress domain. Heller's method of modeling the extrudate swell produced reasonable dimensions that agreed with the dimensions observed in the literature for the die swell.

2.2 Fiber Orientation Modeling

When it comes to fiber orientation modeling in a flow, Jeffery's equation [25] is often taken as the basis for the analysis (see e.g., [26–32]). Jeffery's equation describes the motion of a single fiber in a dilute suspension where the motion of the fiber is unaffected by the presence of any surrounding fiber. Unfortunately, his equation is ineffective for a semi-concentrated or concentrated suspension where there are many fibers in the flow and their presence impacts the motion and position of the surrounding fibers. Thus, Jeffery's model is often extended to incorporate a rotary diffusion term to more accurately predict the fiber orientation state in polymer short fiber composite flows (see e.g., [1,29,33]). Predicting the fiber orientation state is a very complicated problem and the literature base on different aspects of it has been growing since the early part of the 19th century beginning with Jeffery's model of 1922.

2.2.1 Jeffery's Equation

To formulate the techniques for determining the fiber orientation state within a bead printed by FFF, the first item to be addressed is Jeffery's equation [25]. Jeffery built on work done by Einstein [34][32] who provided an equation for the increase in viscosity of a fluid due to suspended spherical particles in the fluid ([34] as cited in [25]). In 1922, Jeffery published his work titled "The Motion of Ellipsoidal Particles Immersed in a Viscous Fluid" in which he derives the equation of motion for the direction of a single, rigid ellipsoidal fiber in a flowing viscous fluid. The direction of the fiber is described by the unit vector **p**, which is depicted in FIG. 2.1 as the blue vector from the origin directed along the major axis of the fiber. The unit vector **p** is easily derived from the figure and is given by the equation

$$\mathbf{p} = \begin{Bmatrix} \sin\theta\cos\phi \\ \sin\theta\sin\phi \\ \cos\theta \end{Bmatrix} \tag{2.1}$$

The angle ϕ in FIG. 2.1 and Equation (2.1) ranges from 0 to 2π radians and the θ ranges from 0 to π radians.

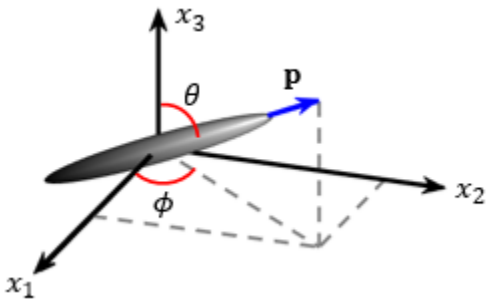

FIG. 2.1. Unit vector (in blue) from the origin along the major axis of the fiber

Jeffery's equation is a set of three, first order, differential equations which describe the rate of change with respect to time of the three components of the unit vector **p** and is cast as

$$\frac{Dp_i}{Dt} = -\frac{1}{2}\Omega_{ij}p_j + \frac{1}{2}\lambda\left(\Gamma_{ij}p_j - \Gamma_{jk}p_jp_kp_i\right) \tag{2.2}$$

In Equation (2.2), p_i represents the i^{th} component of the unit vector **p**, λ is a term that relates to the fiber aspect ratio, Ω_{ij} represents the (i, j) component of the vorticity tensor and Γ_{ij} represents the (i, j) component of the rate of deformation tensor. The $\frac{D}{Dt}$ in Jeffery's equation is the material derivative, which means that the coordinate system follows the center of the fiber as it travels with the fluid. Throughout this text, all indices range from 1 to 3 and designate the respective component of the tensor to which they are appended. In addition, throughout this text repeated indices imply summation on the index, thus $p_ip_i = p_1p_1 + p_2p_2 + p_3p_3$. The vorticity and the rate of deformation tensors are functions of the velocity field **v** through the gradient as, respectively,

$$\Omega_{ij} = \frac{\partial v_j}{\partial x_i} - \frac{\partial v_i}{\partial x_j} \tag{2.3}$$

$$\Gamma_{ij} = \frac{\partial v_j}{\partial x_i} + \frac{\partial v_i}{\partial x_j} \tag{2.4}$$

Note that Γ_{ji} is equivalent to Γ_{ij} as the rate of deformation tensor is symmetric. Additionally, the vorticity tensor is skew symmetric such that $\Omega_{ij} = -\Omega_{ji}$. The vorticity tensor takes into account the spin of the fluid and the rate of deformation tensor takes into account how the strain-rate of the fluid.

Jeffery's equation, presented in Equation (2.2), contains the outer product of the unit vector **p** with the resulting tensor from the outer product of **p** with itself in the term

$p_j p_k p_i$. We could write this as **ppp** recognizing that it implies there are two outer products and is expressed as $p_j p_k p_i$ in index notation. However, index notation is perhaps clearer and will be used when possible in this thesis. The term $p_j p_k p_i$ yields a third order tensor with dimensions of 3x3x3.

The operations in the terms $\boldsymbol{\Omega_{ij}} p_j$ and $\boldsymbol{\Gamma_{ij}} p_j$ in Equation (2.1) are simply linear transformations. If index notation had not been used and instead tensor notation is used, these terms could be expressed as $\boldsymbol{\Omega} \cdot \mathbf{p}$ and $\boldsymbol{\Gamma} \cdot \mathbf{p}$ where "·" denotes the dot product. In any case, these products are contracted along the j^{th} dimension and produce vectors of length 3 along the i^{th} dimension so that they are consistent with the left hand side of Equation (2.2).

The next operation to note in Equation (2.2) is a double contraction between $\boldsymbol{\Gamma_{jk}}$ and $p_j p_k p_i$ in the $\boldsymbol{\Gamma_{jk}} p_j p_k p_i$ term. As was the case earlier, it is also perhaps clearer to write a double contraction in index notation, but one could alternatively write $\boldsymbol{\Gamma_{jk}} p_j p_k p_i$ as $\boldsymbol{\Gamma}$: **ppp** where "**:**" denotes a double contraction. The double contraction operator can be thought of as a higher order version of the dot product. For example, a double contraction of two second-order tensors of equal dimensions is found by multiplying the corresponding components of the tensors together and then summing all of these products. For example, given two 3x3 tensors A and B, $A_{ij} B_{ji} = A : B = A_{11} B_{11} + A_{12} B_{21} + A_{13} B_{31} + \cdots + A_{33} B_{33}$. The double contraction is not limited to second order tensors, however. To define a double contraction more formally, the last two dimensions of the tensor to the left of the "**:**" are contracted with the first two dimensions of the tensor to the right of the "**:**", for example, a double contraction of two fourth order tensors $\mathbb{A}$ and $\mathbb{B}$ is equal to

$$\mathbb{A}:\mathbb{B} = A_{ijkl}B_{lkmn} = C_{ijmn} \tag{2.5}$$

where there is a sum on k and l (see e.g., [26]).

The final effect on fiber orientation of Jeffery's equation of motion, as provided in Equation (2.2), is that it takes into account the actual shape of the fiber through the term λ. As stated earlier, Jeffery derived the model for an ellipsoidal fiber, such as that depicted in FIG. 2.1, but in many industrial applications the fibers are better represented by cylinders as depicted in FIG. 2.2. Trevelyan and Mason experimentally validated Jeffery's model for spheres and extended the form, with experimental validation, to include cylinders [27]. Trevelyan and Mason were able to measure the periods of short-fibers in a fluid under a pure shear flow. They show that since

$$T = \frac{2\pi r_e}{G} \tag{2.6}$$

represents the equation of the period of a prolate spheroid with a moderately high aspect ratio, the measured period T and the shear rate G of the flow can be inserted into this equation and an *equivalent* ellipsoidal aspect ratio r_e can be calculated for the *cylindrical* fibers, where the aspect ratio of a cylindrical fiber is defined as $r = L/d$ where L and d are, respectively, the length and diameter of the fiber. Thus, Equation (2.6) and, subsequently, Jeffery's equation as provided in Equation (2.2), is valid for cylindrical fibers as long as the equivalent ellipsoidal aspect ratio r_e for the cylindrical fiber is used. The equivalent ellipsoidal aspect ratio is then used to compute the geometric parameter λ from Jeffery's equation as

$$\lambda = \frac{{r_e}^2 - 1}{{r_e}^2 + 1} \tag{2.7}$$

Zhang, Smith, and Jack [35] extended the initial work of Trevelyan and Mason [27] to provide finite element validated analytic expressions for the relationship between the cylindrical aspect ratio r and the equivalent ellipsoidal aspect ratio r_e. Zhang *et al.* [35] also extended the application to account for other axisymmetric geometries such as those from the Bead-rod models for flexible fibers (see e.g., [35]).

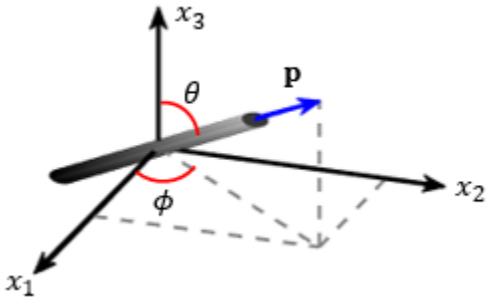

FIG. 2.2. Unit vector (in blue) along the major axis of a cylindrical fiber

2.2.2 Jeffery Orbits

Jeffery's equation predicts that a fiber in a shearing flow will exhibit periodic motion. This periodic motion is commonly referred to as a Jeffery orbit and can be visualized by tracing the path of the tip of the unit vector directed along the fiber. To gain a better understanding of what Jeffery orbits may look like, two Jeffery orbits are shown in FIG. 2.3. The first for a fiber initially pointing along the direction $\mathbf{p} = \left(0, \frac{\sqrt{2}}{2}, \frac{\sqrt{2}}{2}\right)$ is shown in FIG. 2.3(a) and the second fiber with an initial direction of $\mathbf{p} = \left(-\frac{1}{2}, -\frac{1}{2}, -\frac{\sqrt{2}}{2}\right)$ is shown in FIG. 2.3(b). Both fibers have an aspect ratio of $r = \frac{L}{d} \approx 13.57$ which yields an equivalent ellipsoidal aspect ratio of $r_e = 10$ using the equation suggested by Zhang *et al.* [35]. Thus, the value of the geometric parameter λ in the Jeffery equation of Equation (2.2) is

$$\lambda = \frac{{r_e}^2 - 1}{{r_e}^2 + 1} \approx 0.98 \tag{2.8}$$

The fibers are both subjected to the same pure shear flow in the x_1 direction $\mathbf{v} = \{Gx_3, 0, 0\}$, where G is a constant and in this case is the same as the rate of deformation. The velocity field is depicted in FIG. 2.3 by the gray velocity field vectors and the tips of the fibers would follow the paths outlined in blue and red as viewed from the center of the fiber. To understand the fiber paths depicted in FIG. 2.3, it is important to remember that the coordinate system follows the center of the fiber. There are special cases for this particular flow such as if one of the fibers in FIG. 2.3 had been initially aligned in the $x_1 - x_3$ plane (i.e., $\phi = 0$), then its Jeffery orbit would have been the unit circle in the $x_1 - x_3$ plane. Another special case is when one fiber is aligned along the x_2 axis ($\phi = \pi/2$ or $3\pi/2$ and $\theta = \pi/2$). In this case, the fiber would essentially roll in the $x_1 - x_3$ plane, but its Jeffery orbit of the end to end vector would simply be the point (0, 1, 0) or (0, -1, 0) along the x_2 axis. It is important to note that any rolling effects are not included within the Jeffery model as the fibers are assumed to be axisymmetric. It is also important to note that FIG. 2.3 was made for visualization purposes only. Thus, the velocity field vectors shown were chosen based on their visual appearance and not in connection to how Jeffery's equation was solved. The fibers themselves were also chosen to be twice the length of their unit vectors for visualization purposes. The unit vector itself does not have any actual units, and thus the values on the axes do not have meaning. Only the actual shape of the orbits has context.

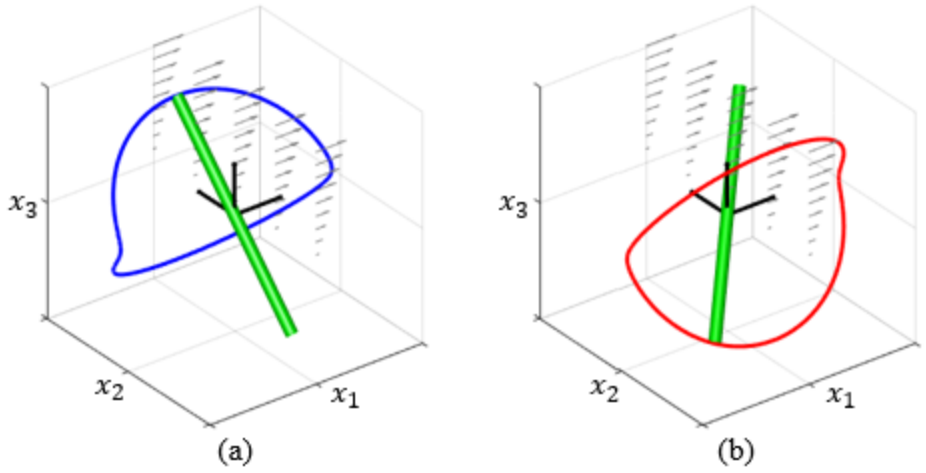

FIG. 2.3. Jeffery orbits for two different initial orientations, (a) $\mathbf{p} = \left(0, \frac{\sqrt{2}}{2}, \frac{\sqrt{2}}{2}\right)$ and (b) $\mathbf{p} = \left(-\frac{1}{2}, -\frac{1}{2}, -\frac{\sqrt{2}}{2}\right)$

FIG. 2.4(a) shows how the components of the unit vector of the fiber given in FIG. 2.3(a) change over time. Likewise, FIG. 2.3(b) shows how the components of the unit vector for the fiber given in FIG. 2.3(b) change over time. An observer may notice that the p_1 component of both unit vectors tends to spend most of its time close to ± 1 for this particular velocity field. As the parameter λ approaches 1, the duration of time that p_1 spends near ± 1 increases, but as the parameter λ decreases to 0, the fibers will spend less time over a single period in alignment. This means that under pure shear flow in the x_1 direction, a fiber will tend to align more with the x_1 direction than with the x_2 or x_3 directions, and, although this is not shown in the figures, higher aspect ratios correspond to longer amounts of time that p_1 will spend near ± 1. In other words, for this velocity field, when a fiber is not aligned closely to the x_1 direction it will rotate very rapidly towards the x_1 axis, slow down while it is near the x_1 axis, and then as it gets farther away from the x_1 axis, it will speed up again. The other components of the unit vectors do not do this. They will tend to spend most of their time near zero and when they come

close to their maximum magnitudes they will not stay there very long but quickly revert towards zero again. Only p_1 and p_2 were graphed in FIG. 2.4 for simplicity.

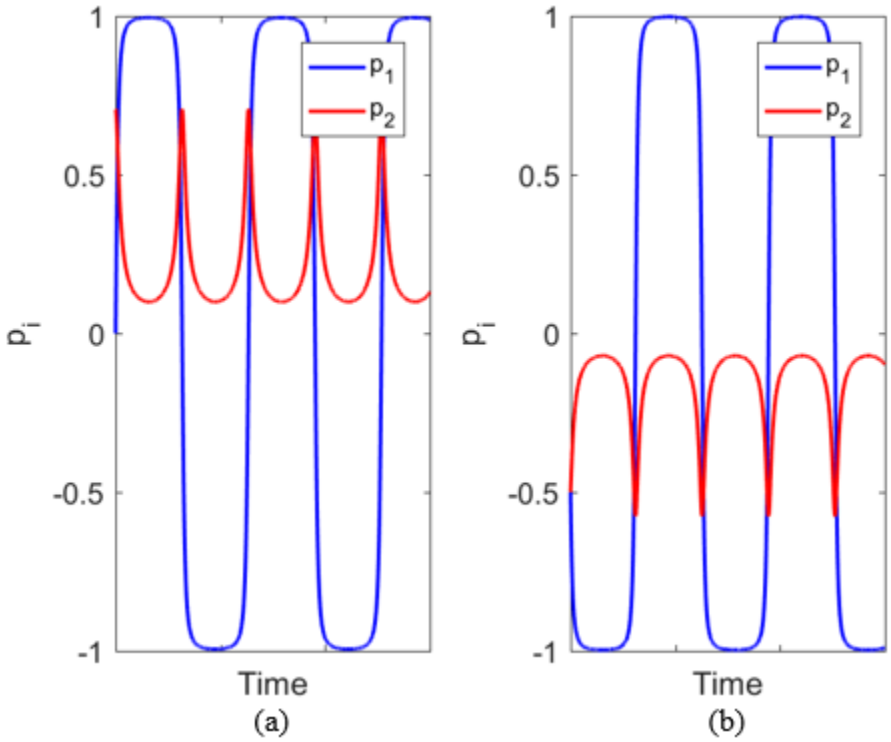

FIG. 2.4. Change in the components of **p** over time given initial orientations, (a) $\mathbf{p} = \left(0, \frac{\sqrt{2}}{2}, \frac{\sqrt{2}}{2}\right)$ and (b) $\mathbf{p} = \left(-\frac{1}{2}, -\frac{1}{2}, -\frac{\sqrt{2}}{2}\right)$

2.2.3 Orientation Tensors

Though Jeffery's model can be solved with a computer very quickly for a single fiber, it is hardly a suitable model in industrial settings where polymer composite parts are made with a very large number of fibers. Therefore a statistical approach is often preferred to solve the fiber orientation problem. Suresh G. Advani and Charles L. Tucker III proposed the use of the computationally efficient orientation tensor approach [28].

A general way to describe the fiber orientation state within a volume containing short, rigid fibers dispersed in a material matrix with a spatially constant fiber

concentration is to use a probability density function (PDF) called ψ [28]. This ψ is a continuous function within the short-fiber composite part and can describe the orientation state at any point. It is a function of both coordinate location within the part and a function of the unit vector $\mathbf{p}$, which is itself a function of ϕ and θ as shown in Equation (2.1). Consequently $\psi(\mathbf{p})$ can also be written in terms of the spherical coordinates as $\psi(\phi, \theta)$. Since there are an infinite number of ways a fiber could be oriented in 3 dimensional space, the probability that a fiber will be oriented exactly along $\mathbf{p}$ is actually zero. Formally, we say the probability that a fiber will be directed between angles ϕ and $d\phi$ and θ and $d\theta$ is

$$P(\theta \leq \theta' \leq \theta + d\theta, \phi \leq \phi' \leq \phi + d\phi) = \psi(\mathbf{p}) \sin\theta \, d\theta d\phi \tag{2.9}$$

where $\sin\theta \, d\theta d\phi$ is an infinitesimally small area on the unit sphere. The unit sphere represents all of the possible points where the tip of the unit vector could be located and thus, accounts for all of the directions that the fiber could be pointing. The expression $\sin\theta \, d\theta d\phi$ is often expressed as $d\mathbf{p}$ and will be used interchangeably throughout the remainder of this text.

It would be convenient to be able to rewrite Jeffery's equation for the motion of individual fibers, Equation (2.2), for a distribution of fibers $\psi(\mathbf{p})$. This can be done using Folgar and Tucker's model (see e.g., [29,30,36,37]), with no fiber interaction terms, as

$$\begin{aligned} \frac{D\psi}{Dt} = &- \frac{\partial \psi}{\partial \theta}\left(\frac{\lambda - 1}{2}\boldsymbol{\kappa}^T : \mathbf{p}\widehat{\boldsymbol{\theta}} + \frac{\lambda + 1}{2}\boldsymbol{\kappa} : \mathbf{p}\widehat{\boldsymbol{\theta}}\right) \\ &+ \frac{1}{\sin\theta}\frac{\partial \psi}{\partial \phi}\left(\frac{\lambda - 1}{2}\boldsymbol{\kappa}^T : \mathbf{p}\widehat{\boldsymbol{\theta}} - \frac{\lambda + 1}{2}\boldsymbol{\kappa} : \mathbf{p}\widehat{\boldsymbol{\theta}}\right) \\ &+ \psi(3\lambda\boldsymbol{\kappa} : \mathbf{pp}) \end{aligned} \tag{2.10}$$

where $\boldsymbol{\kappa}$ is the second-order, velocity gradient tensor $\kappa_{ij} = \frac{\partial v_i}{\partial x_j}$, and $\widehat{\boldsymbol{\theta}}$ is a spherical coordinate unit vector. (Technically $\mathbf{p}$ is equivalent to the spherical coordinate unit vector $\hat{\mathbf{r}}$ as well.) Notice that Equation (2.10) contains the velocity gradients to incorporate the flow field effects and also the geometric parameter λ as in the Jeffery equation, Equation (2.2). However, no longer is the equation of motion just for an individual fiber but for a distribution of fibers. Unfortunately, solving the evolution of Equation (2.10) for the PDF is unreasonable for 3 dimensional cases in the real world as even the simplest of flows require many hours to days to solve (see e.g., [36,38]).

To address the overwhelming computational burden of solving Equation (2.10) for even the most simple of flows, the orientation tensors were introduced by Advani and Tucker [28]. Orientation tensors are the moments of the orientation distribution function $\psi(\mathbf{p})$ and are defined as

$$A_{ijkl\ldots} = \oint p_i p_j p_k p_l \ldots \psi(\mathbf{p}) d\mathbf{p} \tag{2.11}$$

where $\mathbf{p}$ is the unit vector directed along the major axis of the fiber. The indices take on values from 1 to 3 and designate the respective component of the tensor they are appended to, and the integral is over the entire surface of the unit sphere (which includes all of the possible directions the unit vector could be pointing). Thus the second-order orientation tensor is

$$A_{ij} = \oint p_i p_j \psi(\mathbf{p}) d\mathbf{p} \tag{2.12}$$

and the fourth-order is

$$A_{ijkl} = \oint p_i p_j p_k p_l \psi(\mathbf{p}) d\mathbf{p} \tag{2.13}$$

and so on. The orientation tensors are said to be orientation averaged because they involve multiplication by the probability density function and integration over all space. Orientation averaging will be used later in defining the stiffness tensor and coefficient of thermal expansion tensor for an anisotropic composite material. It is also important to note that the orientation tensor notation does not introduce any new physics to the problem but is intended to represent the orientation state of many fibers concisely [28]. For example, the second order orientation tensor is fully described through the use of 9 terms, and, as will be discussed below, this can be reduced to only five terms by accounting for symmetry and normalization.

It turns out that the orientation tensors defined in Equation (2.11) are actually connected to the coefficients in a multiple dimensional series representation of ψ using the complex spherical harmonics (see e.g., [28,39]). Just as the complex spherical harmonic series is infinite, there are an infinite number of orientation tensors also. In addition, as opposed to extracting the orientation tensors from the coefficients of the series representation of ψ, ψ may be reconstructed if given the orientation tensors first. If only a finite number of orientation tensors were given, then the reconstruction of ψ would only be an approximation, however, and the more orientation tensors there are, the more accurate the approximation [37]. The number of orientation tensors needed depends on what they are being calculated for. It turns out that a given, n^{th} order orientation tensor, where n is even, provides all of the even ordered orientation tensors up to the n^{th} order, and provides all of the information needed to calculate any n^{th} order, orientation averaged, material property (see e.g., [28]). This is very helpful to know so that valuable computation time will not be lost on achieving unnecessarily high accuracy. For this

thesis, the fourth-order stiffness tensor is needed along with the second-order CTE tensor which is a function of the fourth-order stiffness tensor. Since *fourth*-order tensor properties are needed, we only need to calculate up to the *fourth*-order orientation tensor and nothing higher because no higher order orientation tensors will help with our accuracy. Actually, when it comes to calculating the fourth-order orientation tensor, we will not even calculate it directly. Instead we use a closure method to approximate the fourth-order orientation tensor in terms of the second-order orientation tensor. This will be discussed in Section 2.2.4.

The probability distribution function ψ is an even function [28], i.e., the probability of finding a fiber pointing along the direction **p** is the same as finding a fiber pointing along – **p**. Thus, $\psi(\mathbf{p}) = \psi(-\mathbf{p})$ must be true and this fact indicates that ψ is an even function. Thus, the only orientation tensors of importance are the even-ordered ones as all odd ordered expressions of Equation (2.11) will integrate to zero [28].

Due to normalization of the unit vector $p_i p_i = 1$, it is easily shown that a higher ordered orientation tensor contains all information regarding the lower orders as

$$A_{ijkk} = \oint p_i p_j p_k p_k \psi(\mathbf{p}) d\mathbf{p} = \oint p_i p_j \psi(\mathbf{p}) d\mathbf{p} = A_{ij} \tag{2.14}$$

Similarly, $A_{ijkl} = A_{ijklmm}$, $A_{ijklmn} = A_{ijklmnpp}$, etc. Other important properties of orientation tensors include the facts that they are entirely symmetric by the construction of Equation (2.11), meaning

$$A_{ij} = A_{ji} \tag{2.15}$$

$$A_{ijkl} = A_{jikl} = A_{kijl} = A_{lijk} = A_{klij}$$

In addition, the trace of the second-order orientation tensor is always equal to one as can be observed from

$$A_{ii} = \oint p_i p_i \psi(\mathbf{p}) d\mathbf{p} = \oint \psi(\mathbf{p}) d\mathbf{p} = 1 \tag{2.16}$$

as the integral of the probability distribution function over all space is equal to one.

The components A_{11}, A_{22}, and A_{33} along the main diagonal of the second order orientation tensor can be physically interpreted as how much of the fibers are oriented in the x_1, x_2, and x_3 directions, respectively. Therefore, one of these components being higher than the others can be interpreted as meaning that the fibers are more biased in that one direction than in the other two directions. For example, if $A_{11} = 1$, then $A_{22} = A_{33} = 0$ (because $A_{11} + A_{22} + A_{33} = 1$ must hold true according to Equation (2.13)). In this case, there would be perfect alignment in the x_1 direction and no fiber alignment in the x_2 and x_3 directions. This scenario is shown in FIG. 2.5(a). FIG. 2.5(b) shows the case where $A_{22} = 1$ and $A_{11} = A_{33} = 0$. The graph for the distribution where $A_{33} = 1$ would contain only vertical fibers. The graph for a perfectly random orientation distribution, i.e., $\psi = constant$, will yield $A_{11} = A_{22} = A_{33} = \frac{1}{3}$ (since the orientation is not biased in any particular direction). This random orientation state for a discrete number of fibers is depicted in FIG. 2.5(d). If one of the diagonal components of A_{ij} is zero, this implies that the orientation distribution is planar in the plane normal to the coordinate direction associated with the zero diagonal component. FIG. 2.5(c) portrays a random planar distribution where $A_{11} = A_{22} = \frac{1}{2}$ and $A_{33} = 0$. In a thin cavity, where the cavity thickness is much less than the fiber length, it is possible to have a fiber orientation state that is planar with no out of plane orientation. However, for this thesis the more general, three-dimensional definitions for the probability density function and orientation tensors will be used as the fiber length is smaller than the cavity thickness of the extruder nozzle

in the 3D printed bead. If one were to try to visualize the probability density function, it may look something like a shaded unit sphere that is shaded darker in the regions where the orientation distribution is biased. For example, for a distribution that is nearly aligned along the x_1 axis, the sphere would be shaded darker near the points $(\pm 1,0,0)$ and lighter between these points, which would be the area around the circular cross section in the x_2-x_3 plane.

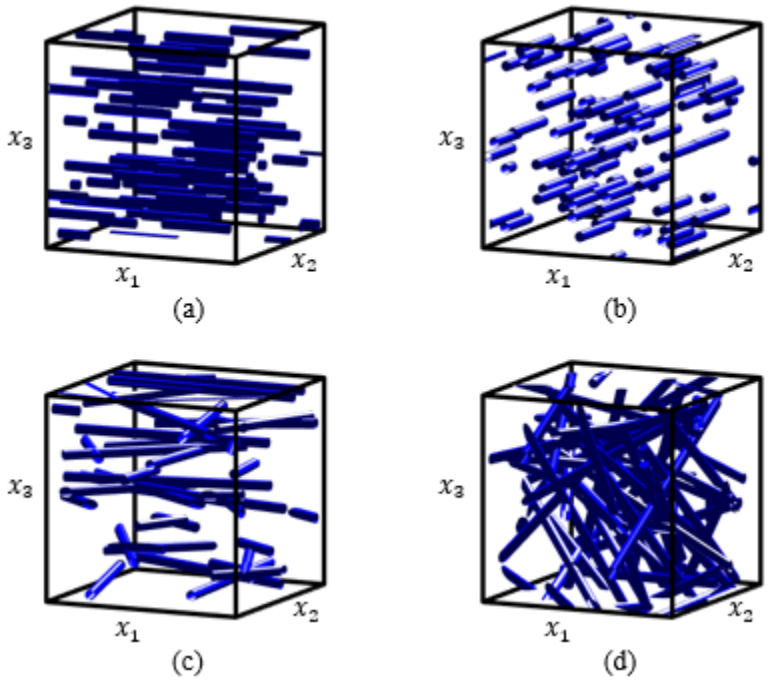

FIG. 2.5. Fiber orientation distributions; (a) uniaxial alignment in x_1 direction, (b) uniaxial alignment in x_2 direction, (c) random distribution in $x_1 - x_2$ plane, (d) completely random distribution

Like the unit vector and the probability density function, the orientation tensors can also be written into evolution equations and were presented in [40] and derived in [36] for the fully anisotropic rotary diffusion form. These are slightly different for the case of planar fiber orientation distribution, but, again, we will stick to the more general,

three-dimensional case for this thesis. The evolution equation for the second order orientation tensor for a three-dimensional distribution is

$$\frac{DA_{ij}}{Dt} = -\frac{1}{2}\left(\Omega_{ik}A_{kj} - A_{ik}\Omega_{kj}\right) + \frac{1}{2}\lambda\left(\Gamma_{ik}A_{kj} + A_{ik}\Gamma_{kj} - 2\Gamma_{kl}A_{ijkl}\right) + \oint \nabla_{\mathrm{p}}(D_r\psi)\cdot\nabla_{\mathrm{p}}\left(p_i p_j\right)d\mathbf{p} \tag{2.17}$$

The Ω_{ij}, Γ_{ij}, and λ terms are defined as they were before for Jeffery's equation, and the δ_{ij} term is the unit tensor. The D_r term in Equation (2.5) is a rotary diffusivity term and can be used to account for fiber-to-fiber interactions. For the case when the rotary diffusivity is independent of the coordinate directions, the integral term can be simplified to the classical expression from Folgar and Tucker [29] of $2D_r\left(\delta_{ij} - 3A_{ij}\right)$, giving

$$\frac{DA_{ij}}{Dt} = -\frac{1}{2}\left(\Omega_{ik}A_{kj} - A_{ik}\Omega_{kj}\right) + \frac{1}{2}\lambda\left(\Gamma_{ik}A_{kj} + A_{ik}\Gamma_{kj} - 2\Gamma_{kl}A_{ijkl}\right) + 2D_r\left(\delta_{ij} - 3A_{ij}\right) \tag{2.18}$$

Fiber interactions significantly affect the fiber orientation in a concentrated fiber-polymer mixture but are not accounted for in Jeffery's original equation. (This topic will be returned to in Section 2.2.5 on fiber interaction models.)

It is important to notice that the fourth-order orientation tensor A_{ijkl} appears in Equation (2.5), which is the evolution equation for A_{ij}. In a similar way, the sixth-order orientation tensor A_{ijklmn} appears in the evolution equation for the fourth-order orientation tensor A_{ijkl} (see e.g., [28,37]):

$$\begin{aligned}\frac{DA_{ijkl}}{Dt} = &-\left(\Omega_{im}A_{mjkl} - A_{ijkm}\Omega_{ml}\right)\\ &+ \lambda\left(\Gamma_{im}A_{mjkl} + A_{ijkm}\Gamma_{ml} - 2\Gamma_{mn}A_{ijklmn}\right)\\ &+ D_r\left[-20A_{ijkl}\right.\\ &+ 2\left\{A_{ij}\delta_{kl} + A_{ik}\delta_{jl} + A_{il}\delta_{jk} + A_{jk}\delta_{il} + A_{jl}\delta_{ik}\right.\\ &\left.\left.+ A_{kl}\delta_{ij}\right\}\right]\end{aligned} \tag{2.19}$$

This pattern is repeated: the evolution equation for any even ordered orientation tensor requires the knowledge of the following higher, even-ordered, orientation tensor (see e.g., [40]). This problem may be resolved by approximating the higher order orientation tensor, and this is usually done in terms of the lower order orientation tensor thereby "closing" the series.

2.2.4 Closure Methods

There exist many closure methods for approximating A_{ijkl} in terms of A_{ij} in order to solve for A_{ij} in the second-order evolution equation. Mathematically one could say the closure method we need is $A_{klmn} \approx f_{klmn}(A_{ij})$ where f is some function that produces a fourth order tensor from the components of the second order orientation tensor [30]. Once the fourth order orientation tensor (A_{klmn}) at a given instant has been found, it can be inserted into Equation (2.17) to solve for the time evolution of A_{ij}. The fourth order tensor will also be needed later on when solving for the stiffness and coefficient of thermal expansion tensors.

Perhaps the simplest of the closures is the quadratic closure. This closure simply approximates A_{ijkl} with the outer product of the second order tensor with itself, $A_{ijkl} \approx A_{ij}A_{kl}$ [41]. The quadratic closure is exact for distributions of perfectly aligned fibers,

but is not very accurate for highly random distributions compared to other models (see e.g., [28]). Another closure is the linear closure of Hand [42]. This closure has the opposite characteristic of the quadratic closure in that it is exact for perfectly random distributions of fibers, but performs more poorly for highly aligned states than other models (see e.g., [28]). This closure approximates A_{ijkl} using all of the possible products of the second order orientation tensor A_{ij} and the second order unit tensor δ_{ij},

$$\begin{aligned} A_{ijkl} = &-\frac{1}{35}\left(\delta_{ij}\delta_{kl} + \delta_{ik}\delta_{jl} + \delta_{il}\delta_{jk}\right) \\ &+ \frac{1}{7}\left(A_{ij}\delta_{kl} + A_{ik}\delta_{jl} + A_{il}\delta_{jk} + A_{kl}\delta_{ij} + A_{jl}\delta_{ik}\right. \\ &\left. + A_{jk}\delta_{il}\right) \end{aligned} \tag{2.20}$$

The hybrid closure combines the strengths of the quadratic closure and linear closure. The hybrid closure is equivalent to the quadratic closure for perfectly aligned orientation states and equivalent to the linear closure for the perfectly random orientation state, and linearly interpolates between the two for orientation states between the two extremes. This can be accomplished mathematically using a function f that is equal to one for completely aligned states and zero for the completely random state [28]. This results in the following closure approximation $A_{ijkl} = (1-f)A_{ijkl}^{linear} + fA_{ijkl}^{quadratic}$, where the form of the parameter f as suggested by Advani and Tucker is $f = \frac{3}{2}A_{ij}A_{ji} - \frac{1}{2}$. When using the hybrid closure to predict mechanical properties, it is, understandably, most inaccurate partway in between the highly aligned and very random orientation states (since neither the linear or quadratic closures are very accurate at this point) [28]. Any of these three closures, the quadratic, the linear, or the hybrid, could be used for calculating the higher order tensor A_{ijkl} in Equation (2.17) and if given the choice between any of

these three closures, the hybrid closure is definitely the best for general orientation cases as it performs reasonably well over the whole range of possible orientation states.

One of the most accurate closure methods available is the orthotropic closure method. This closure method will be used for this thesis. There is actually a whole family of orthotropic closures, as opposed to just one. In the present context, an orthotropic closure is one in which the fourth-order orientation tensor is related in some fashion to the eigenvalues or invariants of the second-order orientation tensor and the principal directions of the fourth-order orientation tensor as assumed to coincide with those of the second-order orientation tensor. Most orthotropic closures involve fitting functions to known data. This allows for variability since multiple functions could be fit to the same data points. Cintra and Tucker developed the first orthotropic closure method based on the idea that all closure methods for approximating A_{ijkl} must be orthotropic and the principal axes of A_{ijkl} must be the same as the principal axes of A_{ij} [30]. This assumption comes at a small loss as short-fiber composites may have monoclinic properties (see e.g., [43]). Monoclinic materials only have a single axis of symmetry, whereas orthotropic materials have three mutually orthogonal axes of symmetry. Since short-fiber composites may experience a material state with fewer symmetries than orthotropic, the orthotropic closures cannot be exact for these materials. Nevertheless, when it comes to fourth order closure methods, the orthotropic closure method can produce approximations that are quite exceptional (see e.g., [44]).

The orthotropic closure method begins with finding the eigenvalues and eigenvectors of the second-order orientation tensor A_{ij}. The eigenvectors denote the principal axes of A_{ij} and the eigenvalue corresponding to the largest eigenvector denotes

the direction of highest fiber alignment. We will call the eigenvalues of the second-order tensor $a_{(1)}$, $a_{(2)}$, and $a_{(3)}$ and designate $a_{(1)} \geq a_{(2)} \geq a_{(3)}$. Writing A_{ij} in its principle reference frame will produce a diagonal matrix with these eigenvalues on the diagonal. Because the trace of a second-order orientation tensor is always one, only two of them are independent, say $a_{(1)}$ and $a_{(2)}$. The second-order tensor rotated into the principal reference frame can be written as

$$\overline{\mathbf{A}} = \begin{bmatrix} a_{(1)} & 0 & 0 \\ 0 & a_{(2)} & 0 \\ 0 & 0 & a_{(3)} \end{bmatrix} \tag{2.21}$$

where the bar accent indicates a principal reference frame value. In order to write the fourth-order orientation tensor, it is convenient to use a contracted notation which is allowable due to Equation (2.15). The fourth-order orientation tensor written in contracted notation and in the principal reference frame can be written in the following way (see e.g., [30])

$$\overline{\mathrm{A}}_{mn} = \begin{vmatrix} \bar{A}_{11} & \bar{A}_{12} & \bar{A}_{13} & 0 & 0 & 0 \\ \bar{A}_{21} & \bar{A}_{22} & \bar{A}_{23} & 0 & 0 & 0 \\ \bar{A}_{31} & \bar{A}_{32} & \bar{A}_{33} & 0 & 0 & 0 \\ 0 & 0 & 0 & \bar{A}_{44} & 0 & 0 \\ 0 & 0 & 0 & 0 & \bar{A}_{55} & 0 \\ 0 & 0 & 0 & 0 & 0 & \bar{A}_{66} \end{vmatrix} \tag{2.22}$$

In essence, an orthotropic closure calculates the components of $\overline{\mathrm{A}}_{mn}$ as functions of the principal values $a_{(1)}$ and $a_{(2)}$ [30]. This means that the form and the coefficients of the functions must be chosen well in order for the orthotropic closure to be accurate. In order to ensure that these functions are chosen well, the probability density function is numerically evaluated for discrete flows using either a control volume or finite element approach, and select points along each of the flows are selected for the fitting. As noted

before, calculating ψ for many points can be computationally prohibitive. The data from the true A_{ijkl} obtained from ψ at different points in time can be used to fit the closure approximation using a least-squares regression technique (see e.g., [30]). Wetzel [45] and VerWeyst *et al.* [46] improved upon the original work of Cintra and Tucker and formulated a new orthotropic closure that behaved well over all possible orientation states. In this thesis we will use the closure used by Wetzel and VerWeyst *et al.* termed the ORT closure.

The natural closures of Verleye and Dupret [47] are similar to the orthotropic closure method (as noted in [30]), along with the invariant based closure of Chung and Kwon [32] (based on the form of the natural closures) and they each yield results comparable to the orthotropic closure results. The natural closures are based on the invariants of the orientation tensor, however, instead of the eigenvalues and eigenvectors like the orthotropic closures. The invariant closures avoid the costly rotations of the tensors, but at the expense of computing a series of higher-order expressions of all possible permutations of the orientation tensor with itself.

Another closure worth noting is the Fast Exact Closure by Montgomery-Smith *et al.* [48] that is able to calculate the orientation state exactly as long as fiber interaction is not taken into account. This model is able to bypass any approximations of A_{ijkl} in terms of A_{ij} by simultaneously solving a set of coupled differential equations [48]. This closure is also computationally efficient and, when accounting for fiber interactions, yields results more accurate than those of the best orthotropic closures for nearly all orientation states (see e.g., [48]).

2.2.5 Fiber Interaction Models

In the industrial world, short fiber composites are often concentrated rather than dilute and it is clear that the fibers will and do interact with each other in the flow of the composite as it is being processed, whether in injection or compression molding or 3D printing. In order to accurately model the changes in fiber orientation, we must account for these fiber interactions. It can be experimentally observed that interaction between fibers not only effects the trajectory of the motion of the fibers, but it also leads to a "steady state" where the bulk average of the fibers maintain an overall constant orientation state. That is not to say the there is no motion by individual fibers, but when observing the overall average orientation state there is no net change. Since Jeffery's equation predicts that a single fiber will not interact with any other fibers and that it will rotate periodically in "Jeffery orbits" forever, Jeffery's model is insufficient for industrial use and an additional expression must be used that incorporates fiber interaction so that orientation states can be more accurately predicted.

Folgar and Tucker presented a fiber interaction model which we will refer to as the Isotropic Rotary Diffusion model or IRD model [29]. Fiber interactions would be extremely complicated and hard to model if all of the forces and torques on each fiber were taken into account. Folgar and Tucker came up with a relatively simple model that intentionally does not go that route, but instead looks at the overall net effect on the orientation state. They added a rotary diffusivity term D_r to the end of Jeffery's equation, represented in Equation (2.2) to account for fiber interactions. They further defined this term as $D_r = C_I\dot{\gamma}$, where C_I is an empirical parameter based on the fluid and the fibers and $\dot{\gamma}$ is the scalar magnitude of the rate of deformation defined as $\dot{\gamma} = \sqrt{\frac{1}{2}\gamma_{ij}\gamma_{ji}}$. The

interaction term behaves like a diffusion term and randomizes the fiber motion. Folgar and Tucker made the following assumptions for their model, taken verbatim, as:

1. The fibers are rigid cylinders, uniform in length and diameter.
2. The fibers are sufficiently large that Brownian motion is negligible.
3. The suspension is incompressible.
4. The matrix fluid is sufficiently viscous that particle inertia and particle buoyancy are negligible.
5. The centers of mass of the particles are randomly distributed.
6. There are no external forces or torques acting on the suspension. [29]

Folgar and Tucker construct their distribution function evolution equation by combining Jeffery's equation, with the added fiber interaction term and a continuity condition. In their original work, they define their interaction coefficient as $C_I = \frac{1}{2}\overline{(\Delta\phi)^2}(l/d)^2 c$ where $\overline{(\Delta\phi)^2}$ is the mean of the squares of the angle changes caused by the fiber interactions, l and d are the fiber length and diameter, respectively, and c is the volume fraction of fibers. But there have been other authors who have come up with different expressions for the relationship between the interaction coefficient and the fiber and melt behavior (see e.g., [49,50]). The evolution equation for the second-order tensor according to the IRD model is

$$\frac{DA_{ij}}{Dt} = -\frac{1}{2}\left(\Omega_{ik}A_{kj} - A_{ik}\Omega_{kj}\right) + \frac{1}{2}\lambda\left(\Gamma_{ik}A_{kj} + A_{ik}\Gamma_{kj} - 2\Gamma_{kl}A_{ijkl}\right) + 2C_I\dot{\gamma}\left(\delta_{ij} - 3A_{ij}\right) \tag{2.23}$$

Equation (2.23) is the same as Equation (2.18) mentioned earlier, where $D_r = C_I\dot{\gamma}$ [28]. Typical values for C_I range from $10^{-4} - 10^{-2}$ (see e.g., [30,51]).

One aspect of the IRD model that is accurate is the irreversibility of the fiber orientation. According to Jeffery's model, when an initial orientation state A evolves into orientation state B during a flow, then the original state A can be returned to if the flow is

reversed. Thus, any orientation state that once existed along a streamline in the polymer flow can be recalculated if the flow were said to go in the opposite direction. Folgar and Tucker's IRD model is not reversible. If an initial orientation state A at a coordinate point 1 evolved into an orientation state B at coordinate point 2 and then the flow was reversed, the IRD model for any non-zero C_I will not necessarily yield orientation state A when the flow returns to point 1.

In addition, there is another point where the IRD model outperforms Jeffery's. As mentioned before, Jeffery's model predicts perpetual periodic motion which is not accurate in the real world. The IRD model, on the other hand, allows for the overall orientation to achieve a steady state value and does not require that the steady orientation state be perfectly aligned [1]. The IRD model will also achieve the same steady state for a particular flow regardless of the initial orientation state [29].

The IRD model is not perfect, however. The major issue is that it predicts that the fibers will achieve a steady orientation state faster than they actually do. In addition, their model requires experimentation for the determination of C_I for new blends of fibers within a polymer matrix.

In 2008, Wang *et al.* [1] proposed a new fiber interaction model that predicted a slower fiber alignment than the IRD model. Their method, termed as the Reduced Strain Closure (RSC) model, takes an intriguing approach to the problem. Instead of addressing just the interaction term of the IRD model, Wang *et al.* decided to break down the second order orientation tensor in Equation (2.18) into its eigenvalues and eigenvectors and write the evolution equations for these. The eigenvalues are what define how much alignment is in the direction of the eigenvectors. Thus, they wanted to change the rate of change of

the eigenvalues but leave the rate of change of the eigenvectors alone. Wang *et al.* then include an empirical term in the eigenvalue equation, which is $\kappa < 1$. This κ value reduces the strain effects on the fiber orientation, which is how the model got its name [1], and in turn will reduce the rate of alignment. This fiber interaction model does indeed slow down the approach to steady state and still yields close to the same steady state values as the IRD would have [1]. The second-order orientation tensor evolution equation for the RSC model can be written as

$$\begin{aligned}\frac{DA_{ij}}{Dt} = &-\frac{1}{2}\left(\Omega_{ik}A_{kj} - A_{ik}\Omega_{kj}\right) \\ &+\frac{1}{2}\lambda\{\Gamma_{ik}A_{kj} + A_{ik}\Gamma_{kj} \\ &-2\Gamma_{kl}\left[A_{ijkl} + (1-\kappa)\left(\mathbb{L}_{ijkl} - \mathbb{M}_{ijmn}A_{mnkl}\right)\right]\} \\ &+2\kappa C_I\dot{\gamma}\left(\delta_{ij} - 3A_{ij}\right)\end{aligned} \tag{2.24}$$

where $\mathbb{L} = \sum_{m=1}^{3}\lambda_m \mathbf{e}_m\mathbf{e}_m\mathbf{e}_m\mathbf{e}_m$ and $\mathbb{M} = \sum_{m=1}^{3}\mathbf{e}_m\mathbf{e}_m\mathbf{e}_m\mathbf{e}_m$ are fourth-order tensors formed by the outer products of the eigenvectors. Here, λ_m is the m^{th} eigenvalue of A_{ij} and $\mathbf{e}_m$ is the associated eigenvector. Note for the $\mathbb{L}$ and the $\mathbb{M}$ expressions we do not use index notation since m is used to express which eigenvector of A_{ij} we are using. Equation (2.24) is very similar to the IRD Equation (2.18) except that A_{ijkl} has been replaced with $\left[A_{ijkl} + (1-\kappa)\left(\mathbb{L}_{ijkl} - \mathbb{M}_{ijmn}A_{mnkl}\right)\right]$ and the interaction term is multiplied by the factor κ. Wang and Jin use a κ value of $1/30$ [52], and when $\kappa = 1$ the RSC model is equivalent to the IRD model.

2.2.6 Micromechanics Models

To calculate the stiffness of the composite given the final fiber orientation state, one can first start with a micromechanical model for the stiffness of a part composed exclusively of a unidirectional fiber orientation state. Once the transversely isotropic properties have been found, they can be averaged, also termed homogenized, over a fiber orientation state that is not unidirectional. This last step will be addressed in Section 2.2.7.

When it comes to calculating the stiffness of a short-fiber composite with a unidirectional fiber orientation state, Tucker and Liang [53] present a review of the available models. Before reviewing a model, they limited their investigation to those models that met the following conditions, taken verbatim, as:

- The fibers and the matrix are linearly elastic, the matrix is isotropic, and the fibers are either isotropic or transversely isotropic.
- The fibers are axisymmetric, identical in shape and size, and can be characterized by an aspect ratio l/d.
- The fibers and matrix are well bonded at their interface, and remain that way during deformation. Thus, we do not consider interfacial slip, fiber/matrix debonding or matrix micro-cracking. [53]

Tucker and Liang investigate Eshelby's dilute model based on an equivalent inclusion [54], the Mori-Tanaka [55,56] model, the bounding model [57], the shear lag model (see e.g., [58]), the self-consistent model [59,60], and the Halpin-Tsai equations (see e.g., [61]).

To describe the micromechanics models, Tucker and Liang [53] define the strain-concentration and the stress-concentration tensors, respectively, Q_{ijkl} and R_{ijkl}, as according to Hill [62]. These tensors are used to relate bulk, or average fields, to those of the individual fibers as

$$\bar{\varepsilon}_{ij}^{f} = Q_{ijkl}\bar{\varepsilon}_{kl} \tag{2.25}$$

and

$$\bar{\sigma}_{ij}^{f} = R_{ijkl}\bar{\sigma}_{kl} \tag{2.26}$$

In these equations, the tensors with the bar accents are average quantities and the superscript f denotes a property of the fiber. Tucker and Liang also define a tensor $\hat{Q}_{ijkl}$ to relate the matrix average strain to that of the fiber average strain as

$$\bar{\varepsilon}_{ij}{}^{f} = \hat{Q}_{ijkl}\bar{\varepsilon}_{kl}{}^{m} \tag{2.27}$$

Here, the superscript m refers to a property of the material matrix and $\hat{Q}_{ijkl}$ can be related to the strain-concentration through the equation

$$Q_{ijkl} = \hat{Q}_{ijkl}[(1 - v_f)\delta_{ijkl} + v_f\hat{Q}_{ijkl}]^{-1} \tag{2.28}$$

In this equation, v_f is the volume fraction of fibers in the composite. At this point, Tucker and Liang reach the main equation we desire derived by Hill [62], where the stiffness of the bulk material is expressed in terms of the stiffness of the fibers and the matrix as

$$C_{ijkl} = C_{ijkl}^{m} + v_f(C_{ijkl}^{f} - C_{ijkl}^{m})Q_{ijkl} \tag{2.29}$$

Equation (2.29) gives us the average stiffness tensor of a short-fiber composite with a unidirectional fiber orientation state. There is a similar equation which expresses the fourth order compliance tensor in terms of the stress concentration factor R_{ijkl} [62],

$$S_{ijkl} = S_{ijkl}^{m} + v_f(S_{ijkl}^{f} - S_{ijkl}^{m})R_{ijkl} \tag{2.30}$$

Now that we have Equation (2.29) we can look at some of the theories leading up to this equation. The first to be considered is Eshelby's dilute model. Eshelby came up with a model to predict the stiffness of a composite of a lone fiber engulfed in an

infinitely extended matrix. This model can therefore be applied to dilute systems. The strain-concentration tensor according to this model can be expressed as

$$Q_{ijkl}^{Eshelby} = \left[\delta_{ij} + E_{ijkl}S_{ijkl}^{m}\left(C_{ijkl}^{f} - C_{ijkl}^{m}\right)\right]^{-1} \tag{2.31}$$

In this equation, E_{ijkl} is Eshelby's tensor. Once $Q_{ijkl}^{Eshelby}$ has been calculated with Equation (2.30) it can be inserted into Equation (2.29) for Q_{ijkl} to get the transversely isotropic stiffness. $Q_{ijkl}^{Eshelby}$ in this model does not depend on v_f so the stiffness solution is predicted to grow linearly with v_f and should not be trusted for fiber volume fractions over 1% [26]. In the present study we focus on composites with higher volume fractions, and this model is not applicable in the present context.

The Mori-Tanaka strain-concentration tensor can be written in terms of the Eshelby strain-concentration tensor as,

$$Q_{ijkl}^{MT} = Q_{ijkl}^{Eshelby}[\left(1 - v_f\right)\delta_{ijkl} + v_f Q_{ijkl}^{Eshelby}]^{-1} \tag{2.32}$$

Tandon and Weng [63] were able to come up with equations for all of the elastic constants (E_{11}, E_{22}, μ_{12}, μ_{23}, k_{23}) for a short-fiber composite using a variant of the Mori-Tanaka model [53]. Although Tandon and Weng state that k_{23} can be calculated iteratively [63], there is also a closed form method of calculating k_{23} that Tucker and Liang suggest [53]. It is the closed form version of Tandon and Weng's Mori-Tanaka approach as expressed in Zhang [64] that is used in the computation of the transversely isotropic stiffness tensor in this thesis. Tucker and Liang recommend the Mori-Tanaka approach as the best of all for predicting the stiffness tensor of a short-fiber composite with an aligned fiber orientation state [53].

Bounding models are different in concept. The point of these models is to provide lower and upper bounds on the stiffness [53]. For example, if the fiber within a short-fiber composite is stiffer than the matrix material, one could say

$$\hat{Q}_{ijkl}^{lower} = [\delta_{ijkl} + E_{ijkl}^{m} S_{ijkl}^{m} (C_{ijkl}^{f} - C_{ijkl}^{m})]^{-1} \tag{2.33}$$

Equation (2.33) could then be inserted into Equations (2.28) and (2.29) to get the lower bound on the stiffness. The upper bound would be

$$\hat{Q}_{ijkl}^{upper} = [\delta_{ijkl} + E_{ijkl}^{f} S_{ijkl}^{f} (C_{ijkl}^{m} - C_{ijkl}^{f})] \tag{2.34}$$

If the matrix material was stiffer than the fiber, Equation (2.33) would provide the upper bound and Equation (2.34) would provide the lower bound instead [53]. Lielens *et al.* [65] developed a model for interpolating between lower and upper bounds in such a way that the stiffness is biased towards the lower bound for small volume fractions and towards the upper bound for large volume fractions [53,65]. The strain-concentrator $\hat{Q}_{ijkl}$ given by Lielens *et al.* [65] and cited in Tucker and Liang [53] is

$$\hat{Q}_{ijkl}^{Lielens} = \left\{(1-f)\left[\hat{Q}_{ijkl}^{lower}\right]^{-1} + f\left[\hat{Q}_{ijkl}^{upper}\right]^{-1}\right\}^{-1} \tag{2.35}$$

where $f = \frac{v_f + v_f^2}{2}$.

Shear lag theories do not predict all of the elastic constants, just E_{11}. Tucker and Liang address them since they have been used a lot though and they usually predict

$$E_{11} = \eta_l v_f E_f + (1 - v_f) E_m \tag{2.36}$$

but Tucker and Liang mention that this is actually not consistent with average strain and stress theories [53]. Thus, the following equation (which is consistent with these concepts) is better

$$E_{11} = E_m + v_f\left(E_f - E_m\right)\eta_l \tag{2.37}$$

In Equations (2.36) and (2.37), η_l represents an efficiency term that depends on the fiber length.

Self-consistent theories use the concept of a particle (or a "fiber" in our case) in an infinitely extended matrix where the matrix has the averaged properties of the whole composite [53]. The strain-concentrator is given by

$$Q_{ijkl}^{SC} = \left[\delta_{ijkl} + E_{ijkl}S_{ijkl}\left(C_{ijkl}^{f} - C_{ijkl}\right)\right]^{-1} \tag{2.38}$$

where the C_{ijkl} and S_{ijkl} tensors without the f or m superscripts refer to the properties of the whole composite.

The Halpin-Tsai equations (see e.g., [53]) can be written in a general form,

$$\frac{P}{P_m} = \frac{1 + \zeta\eta v_f}{1 - \eta v_f} \tag{2.39}$$

$$\eta = \frac{(P_f/P_m) - 1}{(P_f/P_m) + 1} \tag{2.40}$$

In Equation (2.22) the P can be any of five moduli, k_{23}, G_{23}, G_{12}, K, or G. These are, respectively, the plane strain bulk modulus, the transverse shear modulus, the longitudinal shear modulus, the bulk modulus, and the shear modulus [53]. The P's with the subscripts m and f are the same moduli for the matrix and fiber, respectively. ζ is a term that varies depending on which modulus is being calculated. Nielsen and Lewis [66] modified Halpin and Tsai's equations to be the following

$$\frac{P}{P_m} = \frac{1 + \zeta\eta v_f}{1 - \psi\left(v_f\right)\eta v_f} \tag{2.41}$$

where ψ is a function of the volume fraction and contains the maximum volume fraction as a parameter [53,67]. ψ is constructed so that it gives accurate values near the lower

and upper limits of the volume fraction [53]. The form of Equation (2.41) was actually found by Ingber and Papathanasiou [68] to better represent the effective longitudinal modulus for short-fiber composites with aligned fiber orientation states than Equation (2.39) (as noted in [53]).

The transversely isotropic stiffness tensor C_{ijkl} for a short-fiber composite with the fibers aligned along x_1 can be related to the five material constants in contracted notation as (see e.g., [15,36])

$$\mathbf{C} = \begin{vmatrix} \frac{1}{E_{11}} & \frac{-\nu_{12}}{E_{11}} & \frac{-\nu_{12}}{E_{11}} & 0 & 0 & 0 \\ \frac{-\nu_{12}}{E_{11}} & \frac{1}{E_{22}} & \frac{-\nu_{23}}{E_{22}} & 0 & 0 & 0 \\ \frac{-\nu_{12}}{E_{11}} & \frac{-\nu_{23}}{E_{22}} & \frac{1}{E_{22}} & 0 & 0 & 0 \\ 0 & 0 & 0 & \frac{1}{G_{23}} & 0 & 0 \\ 0 & 0 & 0 & 0 & \frac{1}{G_{12}} & 0 \\ 0 & 0 & 0 & 0 & 0 & \frac{1}{G_{12}} \end{vmatrix}^{-1} \tag{2.42}$$

with $\nu_{23} = \frac{E_{22}}{2G_{23}} - 1$.

2.2.7 Stiffness and Thermal Expansion Tensors

Although most short-fiber composite material being extruded with FFF is fairly well aligned in the direction of the print path after extrusion, the fibers will not be perfectly aligned. However, once the transversely isotropic stiffness of a particular composite is known, we can do an orientation averaging procedure, also termed orientation homogenization, to find the stiffness of that composite for an arbitrary orientation state. Thus, if we know the theoretical transversely isotropic stiffness of a short-fiber composite and the anisotropic fiber orientation state at an arbitrary point

within the actual composite part, we can calculate the anisotropic fourth-order stiffness tensor at that point. This statement could be made even more general: the orientation average of a tensor property of arbitrary order n is completely found by the n^{th}-order orientation tensor and the unidirectional form of that property tensor (see e.g., [28,40]). If **T** is a property tensor of arbitrary order then its orientation average is

$$\langle \mathbf{T} \rangle = \oint \mathbf{T}(\mathbf{p})\psi(\mathbf{p})d\mathbf{p} \tag{2.43}$$

In this equation, **p** is the unit vector describing the orientation direction. When it is calculated, a fourth-order, transversely isotropic tensor property can be written in the form

$$\begin{aligned} T_{ijkl}(\mathbf{p}) = {} & B_1\left(p_i p_j p_k p_l\right) + B_2\left(p_i p_j \delta_{kl} + p_k p_l \delta_{ij}\right) \\ & + B_3\left(p_i p_k \delta_{jl} + p_i p_l \delta_{jk} + p_j p_l \delta_{ik} + p_j p_k \delta_{il}\right) \\ & + B_4\left(\delta_{ij}\delta_{kl}\right) + B_5\left(\delta_{ik}\delta_{jl} + \delta_{il}\delta_{jk}\right) \end{aligned} \tag{2.44}$$

But Jack and Smith showed in [39] that Equation (2.44) was not a prerequisite for the analytic evaluation of Equation (2.43). Through the use of spherical harmonics, Jack and Smith [39] demonstrated that the material stiffness tensor expectation can be cast exactly as a function of the fourth-order and lower order orientation tensors. The homogenized stiffness in terms of these orientation tensors is (see, e.g. [36])

$$\begin{aligned} \langle C_{ijkl} \rangle = {} & B_1\left(A_{ijkl}\right) + B_2\left(A_{ij}\delta_{kl} + A_{kl}\delta_{ij}\right) \\ & + B_3\left(A_{ik}\delta_{jl} + A_{il}\delta_{jk} + A_{jl}\delta_{ik} + A_{jk}\delta_{il}\right) + B_4\left(\delta_{ij}\delta_{kl}\right) \\ & + B_5\left(\delta_{ik}\delta_{jl} + \delta_{il}\delta_{jk}\right) \end{aligned} \tag{2.45}$$

where the brackets indicate the orientation average of the term inside the brackets. In Equation (2.45) for the underlying transversely isotropic stiffness tensor, the coefficients

B_i from Jack and Smith [39] are the same as those originally presented in Advani and Tucker [28] as

$$\begin{Bmatrix} B_1 \\ B_2 \\ B_3 \\ B_4 \\ B_5 \end{Bmatrix} = \begin{Bmatrix} C_{11} + C_{22} - 2C_{12} - 4C_{66} \\ C_{12} - C_{23} \\ C_{66} + 0.5(C_{23} - C_{22}) \\ C_{23} \\ 0.5(C_{22} - C_{23}) \end{Bmatrix} \tag{2.46}$$

The C_{ij}'s correspond to the components of the contracted version of the transversely isotropic stiffness tensor in Equation (2.42).

Once the fourth-order homogenized stiffness tensor $\langle C_{ijkl} \rangle$ has been determined, the second-order homogenized coefficient of thermal expansion tensor can also be determined [69]. With the effects of thermal stress included,

$$\langle C_{ijkl} \alpha_{kl} \rangle = D_1 A_{ij} + D_2 \delta_{ij} \tag{2.47}$$

where $C_{ijkl} \alpha_{kl}$ is a double contraction of the transversely isotropic stiffness and the transversely isotropic CTE tensors and the coefficients D_1 and D_2 are given as

$$D_1 = A_1(B_1 + B_2 + 4B_3 + B_5) + A_2(B_1 + 3B_2 + 4B_3) \tag{2.48}$$

$$D_2 = A_1(B_2 + B_4) + A_2(B_2 + 3B_4 + B_5) \tag{2.49}$$

where

$$A_1 = \alpha_{11} - \alpha_{22} \tag{2.50}$$

$$A_2 = \alpha_{22} \tag{2.51}$$

The α_{11} and α_{22} correspond to the CTE tensor of the unidirectional composite along, respectively, the x_1 and x_2 direction. These transversely isotropic CTE coefficients can be found using micromechanical theories. In the present study we use the method introduced by Schapery [70] and refined by Halpin [71] as expressed in Stair and Jack

[72]. To find the homogenized CTE tensor by itself, Equation (2.30) is right-multiplied by $\langle C_{ijkl} \rangle^{-1}$ to yield

$$\langle \alpha_{ij} \rangle = \langle C_{ijkl} \alpha_{kl} \rangle \langle C_{ijkl} \rangle^{-1} \tag{2.52}$$

where $\langle C_{ijkl} \rangle^{-1}$ is the inverse of the fourth order orientation averaged stiffness tensor. This is not a trivial calculation as $\langle C_{ijkl} \rangle$ must be written in contracted form, then inverted in the 6x6 contracted form, and then recast back to fourth-order.

CHAPTER THREE

Computational Methods

The following chapter presents the solution methodology for predicting the final bead stiffness and coefficient of thermal expansion tensors for dilute and concentrated short-fiber suspensions. The chapter begins with an overview of the solution methodology with emphasis given to the analysis of the orientation state. The methodology is demonstrated through an example of planar flow without including the die swell effects on the extrudate. The focus on the planar flow without the die swell is given to highlight the differences in the orientation state and the final part performance between the dilute suspension model of Jeffery, and then the concentrated suspension models of Folgar and Tucker [29] and Wang *et al.* [1].

3.1 Computational Methodology Overview

In order to predict the effective longitudinal stiffness and coefficient of thermal expansion of a 3D printed, short-fiber reinforced composite bead, both COMSOL and MATLAB were used according to the flow chart in FIG. 3.1. First, the flow geometry, boundary conditions, and initial conditions are defined in COMSOL to be roughly based on the dimensions of a large scale 3D printer nozzle. COMSOL is then used to calculate the velocities and velocity gradients along several streamlines during the melt flow. The velocity profile as a function of spatial location is calculated at many points along each streamline and then the data is exported to files that are loaded in MATLAB. In MATLAB, in-house programs have been written to calculate the orientation tensors

following Equation (2.2) for individual fiber motion in a dilute suspension and Equations (2.23) and (2.24) for the motion of the fibers in a concentrated suspension. After the orientation tensors are found along each streamline, they are input into in-house MATLAB codes that calculate the spatially varying stiffness tensor, C_{ijkl}, using Equations (2.45)-(2.46) and the coefficient of thermal expansion tensor, α_{ij}, using Equations (2.45)-(2.52) along the streamlines. As the final step, MATLAB and COMSOL are linked via LiveLink™, so that the stiffness and thermal expansion tensors calculated at the end of each streamline, corresponding to the end of the flow within the 3D printer nozzle, are used to define the stiffness and thermal expansion properties of two samples in COMSOL. One of these samples is used to simulate a tensile test of a 3D printed bead and the other is to simulate a test for the coefficient of thermal expansion. After these tests have been simulated in COMSOL, the effective longitudinal Young's modulus and effective longitudinal coefficient of thermal expansion can be derived from the numerical results in COMSOL. These latter results will be compared to the tensile testing and the thermo-mechanical test results of physical specimens in Chapter Four.

The model assumptions made in this chapter include the following.

1. The fibers are short, rigid cylinders and they all have the same aspect ratio and are uniformly distributed throughout the composite.
2. The upstream section of the nozzle is sufficiently long enough such that the orientation state from the screw can be neglected when defining the flow geometry.
3. The polymer melt flow is decoupled from the fiber inclusions, is isothermal, and is represented by a Newtonian fluid.

4. The change in the velocity gradient is sufficiently small such that it can be assumed constant over the length scale of an individual fiber.
5. The fiber and matrix are assumed to be linearly elastic, their material properties are isotropic, and the fiber and matrix are well bonded after processing.

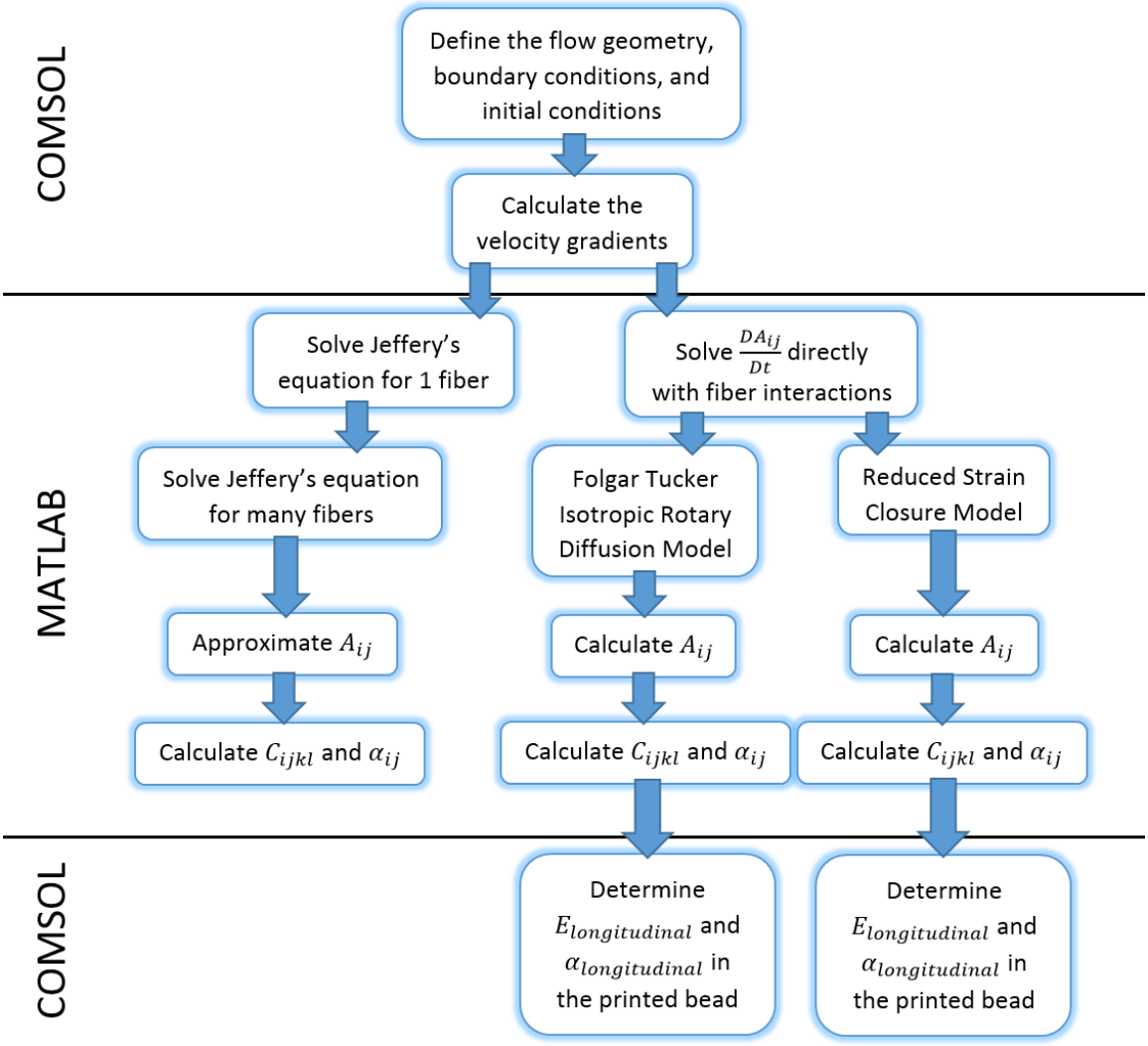

FIG. 3.1. Flow chart of the computational process

3.2 Flow Geometry, Boundary Conditions, and Initial Conditions

In order to predict the effective longitudinal modulus and CTE in a short-fiber composite printed with a BAAM system, the first step is to model the flow geometry (i.e.,

the inner dimensions of the BAAM nozzle) in COMSOL. Rough dimensions for the nozzle geometry came from measuring the actual large scale, FFF extruder, a Strangpresse Extruder Model 19, which was used in the experimental phase of this study. This extruder is the same brand and model extruder, with a slightly reduced flow rate, used by Oak Ridge National Laboratory as part of the broader work in commercializing the BAAM process. The actual interior geometry of the nozzle is very complicated up-stream near the screw, so it was decided that for modeling purposes the up-stream flow features would be neglected and a simpler geometry would be used with roughly the same diameters for the nozzle exit and before the nozzle exit. As will be shown by the results later in this chapter, the dominating features dictating the orientation state are the contraction zone and the tip length after the contraction zone where shear flow dominates. The 3 mm and 12 mm diameters depicted in FIG. 3.2 are approximations taken directly from the Strangpresse nozzle.

In addition to the inner geometry of the nozzle, the proper boundary conditions and initial conditions need to be defined. It should be noted for this first example that although this problem could be modeled as axisymmetric, it is instead modeled in COMSOL in two dimensions and can thus be viewed as an infinite channel, extending infinitely in the positive and negative x_3-directions. The top of the geometry is defined as an inlet condition in COMSOL as Laminar Inflow with an average velocity of 7.66 mm/s. The outlet condition is prescribed to have a pressure of zero and the flow direction constrained to the direction normal to the surface. The other boundaries are walls with no slip with a velocity vector $\boldsymbol{v} = \mathbf{0}$.

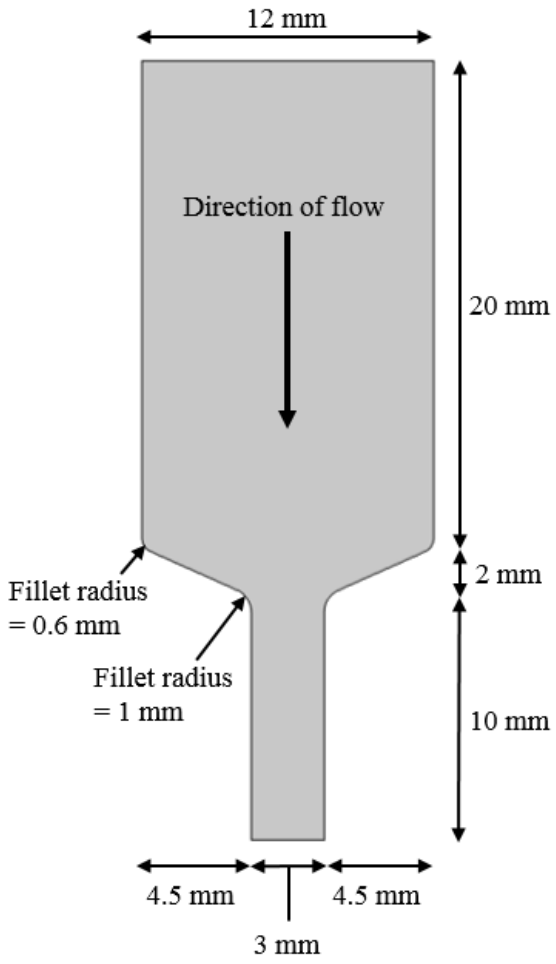

FIG. 3.2. COMSOL flow geometry roughly based on a Strangpresse Extruder Model 19

As for initial conditions, the average inlet velocity is approximately 7.66 mm/s. This is determined by first manually measuring the throughput of the physical extruder. This was done with a hand held stopwatch on an iPhone 4s. The throughput for 13% carbon fiber filled ABS was determined to be approximately 60 grams/min. At first glance, this value might seem too low when compared to the advertised output for the Strangpresse Extruder Model 19, which is said to be 20 lbs/hr (about 151 grams/min), but this advertised value is for neat ABS [73]. Thus, it is important to remember that these measurements were taken from two different materials. After the throughput value was found, the density of the material was approximated using the following equation

$$(fiber\ density) * (\%\ fiber) + (ABS\ density) * (\%\ ABS) = density$$

$$\left(1.85\ \frac{g}{cm^3}\right) * (13\%) + \left(1.05\ \frac{g}{cm^3}\right) * (87\%) = 1.154 * 10^{-3}\ \frac{g}{mm^3} \qquad (3.1)$$

The inlet flow speed could then finally be determined using the following equation

$$inlet\ flow\ speed = \frac{(throughput/density)}{(inlet\ cross\sim sectional\ area)}$$
$$= \frac{(60\ g/min)/(1.154 * 10^{-3}\ g/mm^3)}{\pi * (0.5 * 12\ mm)^2} \approx 7.66 \frac{mm}{s} \qquad (3.2)$$

3.3 Calculation of the Velocity Gradients

Once the geometry, boundary conditions, and initial conditions have been defined in COMSOL, COMSOL is used to do a finite element analysis (FEA) to obtain the velocity profile during the melt process along individual streamlines. In Section 3.2 up to Section 3.6.2, 20 streamlines are used for the calculation as well as an extra fine mesh with 332,805 degrees of freedom. The computation takes about 25 seconds to obtain the velocity profile and the solution along the various streamlines is shown in FIG. 3.3. In this plot, 20 colored streamlines can be seen where the blue side of the color spectrum indicates smaller velocity magnitudes and the red side of the color spectrum indicates larger velocity magnitudes. Thus, as shown in the figure, the velocity of the fluid tends to speed up as the nozzle diameter gets smaller. The velocity is also faster towards the center of the nozzle as opposed to the walls which have a no slip boundary condition, with the greatest speed near the nozzle exit. Streamlines 0 and 8 have been pointed out since they will be used later in the analysis done in this chapter. They are specifically chosen since they represent the polymer melt flow near the wall of the nozzle as well as near the center of the nozzle.

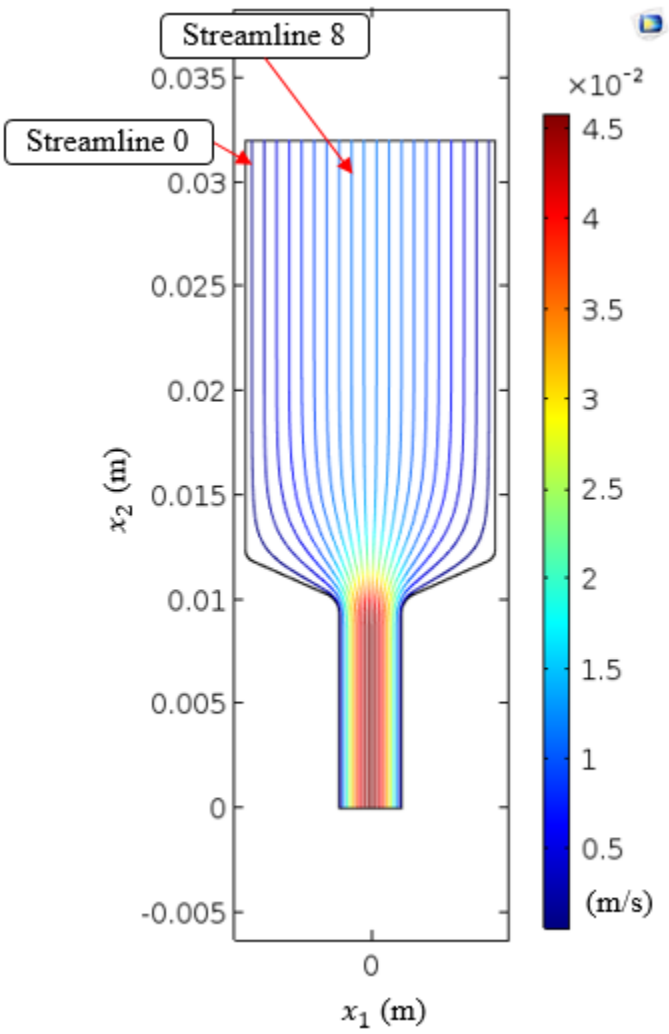

FIG. 3.3. Streamlines; the color scheme depicts velocity magnitude

Once the finite element analysis is done, the velocity gradient data is exported from COMSOL into a text file in columnar format. The first two columns give x_1 and x_2 coordinate locations, respectively, the third column gives the streamline number, and the fourth column gives the value of the specified velocity gradient. In the case of 20 streamlines, COMSOL would number them by default as 0-19 and increasing from left to right. The velocities in the x_1 and x_2 directions can also be exported in this exact same

format and they are useful in converting the spatial location over to units of time for use in the time solution of the fiber orientation equations of motion.

Once the velocity gradient data has been exported from COMSOL it is loaded into a MATLAB file which makes plots of the velocity gradients for a user-selected streamline. The results for streamline 0, which is the leftmost streamline, and streamline 8 which is slightly left of the center of the nozzle, are shown in FIG. 3.4 and FIG. 3.5, respectively.

In FIG. 3.4 and FIG. 3.5 the left side of the plot is the inlet, at about $x_2 = 0.012\ m$ the flow moves to the contraction region, and at about $x_2 = 0.010\ m$ the flow enters the straight region of the extruder immediately before the exit. As can be seen in Figure 3.4, the velocity gradients start out as constant and the only component that is not zero is $\frac{dv_2}{dx_1}$. This means that in this initial region of the nozzle, the velocity in the x_1-direction, v_1, is not changing across streamline 0 with respect to the positive x_1 or x_2 directions. (This should be obvious since there is no horizontal movement.) The velocity in the x_2-direction, v_2, also does not change with respect to the positive x_2-direction in this region. However, the velocity in the x_2-direction does change with respect to the x_1-direction in this region because the flow is going slightly faster downward in the center of the nozzle than it is along the no slip walls. It is harder to notice this detail if we only look at FIG. 3.3 instead of FIG. 3.4, but with careful examination of FIG. 3.3 one can see that the blue streamlines are, indeed, a slightly lighter shade of blue in the center of the nozzle than they are closer to the edges. This means that the flow is slightly quicker in the center of the nozzle than it is on the edges.

At an x_2-coordinate of about $0.012\ m$, the nozzle starts to taper and large changes in the velocity gradients can be observed in FIG. 3.4. $\frac{dv_1}{dx_1}$ quickly increases because the velocity in the positive x_1-direction increases with respect to the positive x_1-direction across streamline 0 as the flow moves inward toward the middle of the nozzle and not just vertically downward. It then levels out at 0 after $x_2 \approx 0.01\ m$ because the flow enters the narrow part of the nozzle and the flow is again directed only in the vertical direction. For this geometry, $\frac{dv_1}{dx_2}$ also increases along streamline 0 because the x_1-velocity increases positively with respect to the positive x_2-direction. The most dynamic velocity gradient is $\frac{dv_2}{dx_1}$, which rises slightly and then dips dramatically, meaning that from left to right across streamline 0, the x_2-velocity decreases in magnitude just before the nozzle starts to taper and then increases in magnitude dramatically at the beginning of the tapered section. Thus, the flow is much faster in the center of the tapered part of the nozzle than it is near the walls. $\frac{dv_2}{dx_1}$ then rises slightly again and flat lines in the straight region at the end of the nozzle, meaning that after the tapered part of the nozzle, in the straight, end section, the change in the x_2-velocity from left to right is not as dramatic as it was at the end of the tapered part of the nozzle. In addition, after sometime, the change in the x_2-velocity from left to right will stay constant across streamline 0 in the straight, end section of the nozzle, but will still be more dramatic than it was to begin with in the larger, straight section of the nozzle. This, in essence, means that there are larger shear rates in the small, end section than there are in the large, beginning section of the nozzle. Finally, the fact that $\frac{dv_2}{dx_2}$ goes negative in FIG. 3.4 in the tapered-nozzle region means that the velocity is accelerating downward along streamline 0 in this region. It then settles to a

constant value. Of note, these velocity gradients will affect the orientation state, but as will be shown below, the elongational gradient terms ($\frac{dv_1}{dx_1}$ and $\frac{dv_2}{dx_2}$) will dominate the flow when they are present.

Similar types of explanations that were made regarding FIG. 3.4 can also be made for FIG. 3.5. Again, the large changes in the velocity gradients in FIG. 3.5 are in the tapered part of the nozzle. The biggest difference between the two is the relative values of the shearing gradients, $\frac{dv_1}{dx_2}$ and $\frac{dv_2}{dx_1}$, versus the elongational gradients, $\frac{dv_1}{dx_1}$ and $\frac{dv_2}{dx_2}$. The impact of this will become more obvious when looking at the orientation state whereby the fibers become highly aligned in the center channel of the flow due to the relatively high elongational effects within the tapered part of the nozzle.

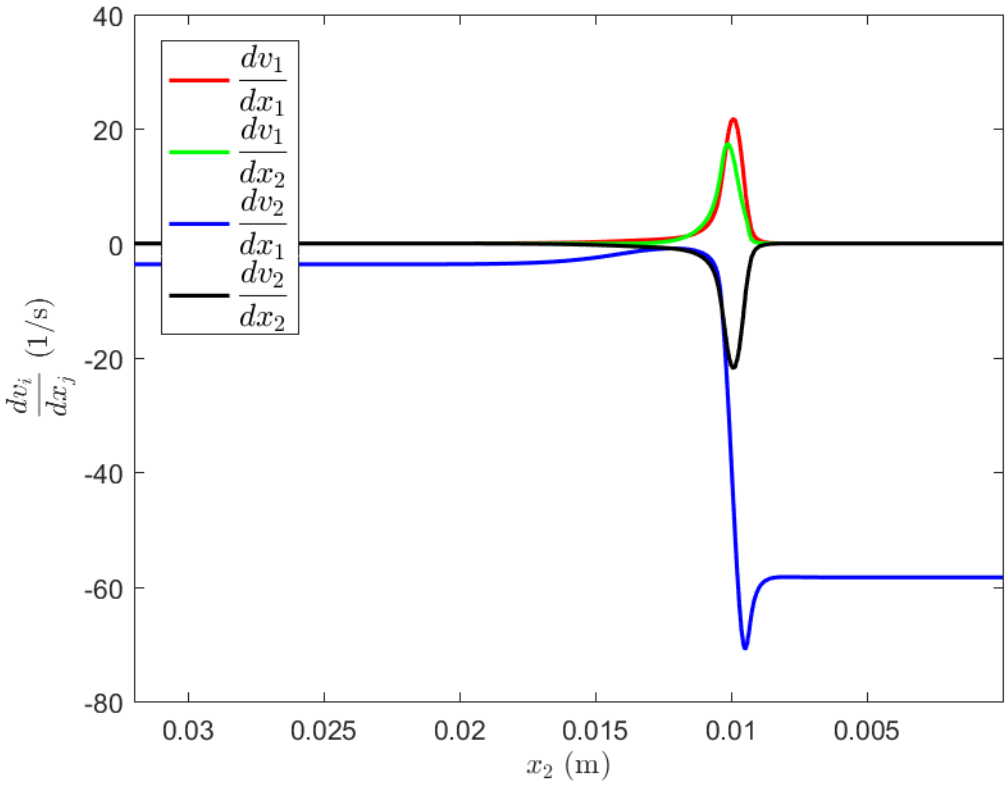

FIG. 3.4. Velocity gradients along streamline 0

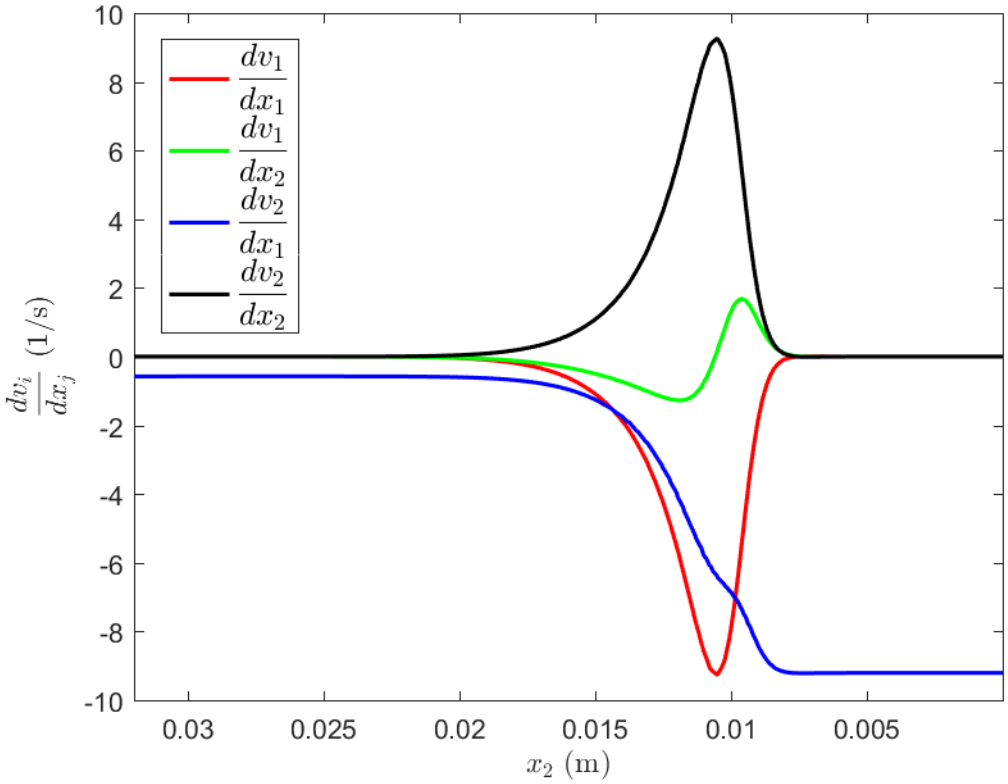

FIG. 3.5. Velocity gradients along streamline 8

3.4 Evolution of the Unit Vector

Once the velocity gradients have been calculated for a streamline, it is possible to calculate the vorticity and rate of deformation tensors also from Equations (2.3) and (2.4). More importantly, it is also possible to solve Jeffery's Equation, from Equation (2.2), directly, which depends on the vorticity and rate of deformation tensors. In this way, the change in orientation of a single fiber moving along a single streamline can be studied.

To solve Jeffery's Equation, it is programmed as a function file in MATLAB. This function file is solved in a script file by using a built-in ordinary differential equation (ODE) solver in MATLAB called `ode45`. An ODE solver is needed because Jeffery's Equation is actually a coupled system of three ODEs. However, before solving Jeffery's Equation with the ODE solver, one of the first steps to be done in the script file

is to load the velocity and velocity gradient data from the COMSOL simulation. It is also necessary to find at what moments in time the velocity and velocity gradient data is given by COMSOL, since this information is needed later but is not exported by COMSOL. Since COMSOL exports the velocity data such that the x_1 and x_2 velocities are given at the same coordinate points, one can obtain not only the velocity magnitudes between points, but also the distance between points. From these values, the formula

$$time = \frac{distance\ between\ points}{average\ magnitude\ of\ velocity} \tag{3.3}$$

can be used to find at what moments in time the velocities and velocity gradients are known.

When everything has been properly defined and Jeffery's Equation is ready to be solved with `ode45` within the script file, `ode45` will accept several inputs. The first input defines the time span and at which points in time the solution will be returned by the solver. The number of points does not state the time stepping scheme used by MATLAB's solver as `ode45` is an adaptive step size solver, but only determines the points at which the solution is returned for later use. For this case, 500 time steps were chosen to provide sufficient smoothness in later plotting. The next input is the initial unit vector of the individual fiber being analyzed. The initial orientation is defined by the unit vector given in Equation (2.1) where $\theta = \pi/4$ radians and $\phi = \pi/4$ radians. The third input contains various solver options that can be specified for the ODE solver. For this case, the only option that is chosen is that the relative error tolerance be 10^{-8}. The next input into the `ode45` function is λ, where λ is defined by Equation (2.7) and in the present studies the parameter r_e, the equivalent ellipsoidal aspect ratio, to define λ is

chosen to be 10. The last two inputs are the times calculated from the COMSOL data along with the velocity gradient data.

After all the necessary information has been accounted for, Jeffery's Equation can be solved in MATLAB with `ode45` for a single, user-selected streamline. To produce FIG. 3.6 and FIG. 3.7, streamline 0 was chosen and streamline 8 was chosen when producing FIG. 3.8. These plots show two components of the unit vector **p** as they change with x_2-location and time. It is worth noting that although the flow is modeled as planar, Jeffery's model does not constrain the fiber to rotate in this plane – that is, p_3 is not always 0 and could be shown to vary if it was graphed in FIG. 3.6 and FIG. 3.7. However, for simplicity, only p_1 and p_2 are graphed.

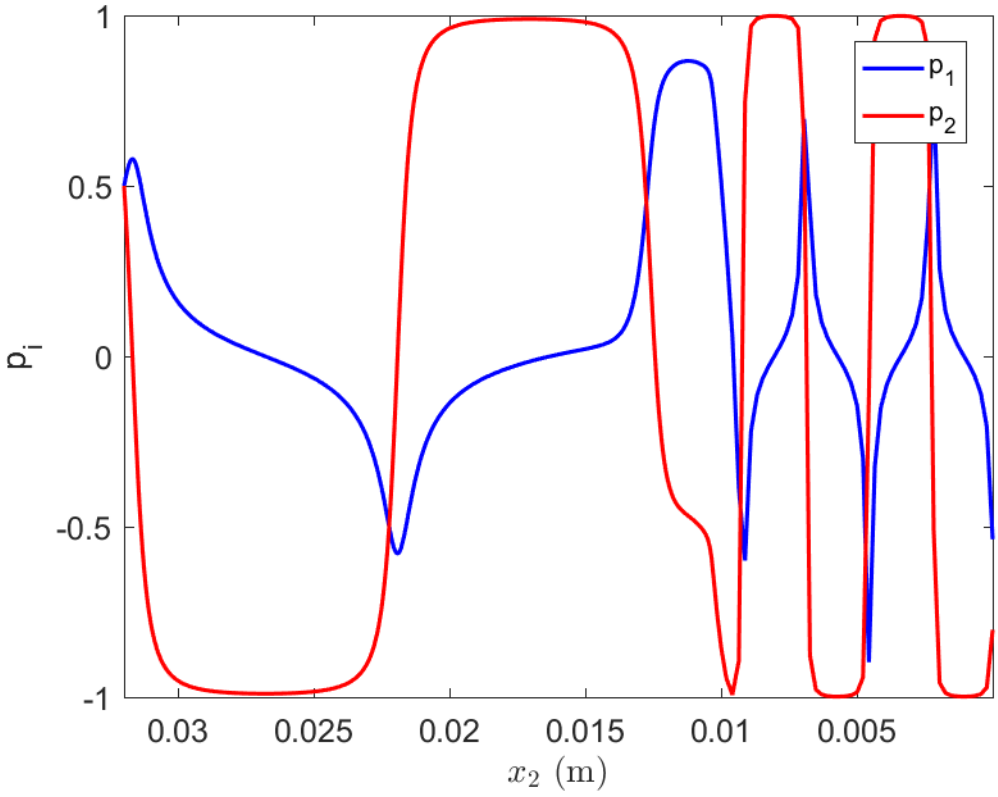

FIG. 3.6. Components of **p** as a function of x_2 – streamline 0

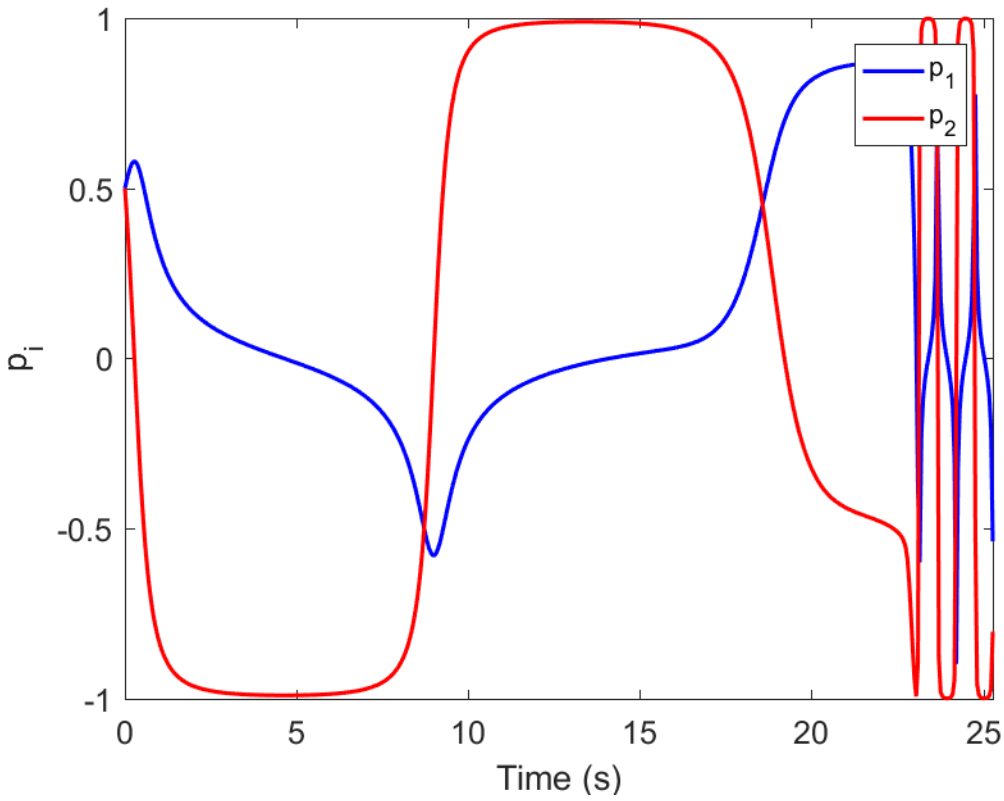

FIG. 3.7. Components of **p** as a function of time – streamline 0

It can be observed in FIG. 3.6, for **p** as a function of position within the extruder, and FIG. 3.7 for **p** as a function of time within the extruder, that the components of **p** tend to oscillate in the initial phase of the flow due to the periodic motion predicted by Jeffery's Equation (the Jeffery orbits) for a fiber in a shearing flow. Then around $x_2 = 0.012\ m$, which corresponds to 20 seconds into the flow, where the nozzle begins to taper and the flow transitions to elongational, the alignment state rapidly changes. After the taper is ended and the flow transitions back to shear dominated, the flow acclimates to the final straight portion of the nozzle. The periods of the curves near the exit, for values of $x_2 < 0.01\ m$, or equivalently for $t > 20\ s$, are shorter than they are before $x_2 > 0.012\ m$, or equivalently for $t < 20\ s$, due to the larger magnitude of the shear in the end of the nozzle, where the diameter is smaller. The shear is not as large at the beginning of

the nozzle, where the diameter of the nozzle is larger. The primary difference between FIG. 3.6 and FIG. 3.7 is that in time the oscillations are very closely packed for the later flow within the narrow portion of the nozzle.

The oscillations in FIG. 3.6 and FIG. 3.7 are relatively frequent for streamline 0 because the shear rates are relatively high near the wall of the nozzle. We do not see this behavior for all streamlines, however. For example, FIG. 3.8 for the flow along streamline 8 occurring near the center of the channel does not show any periodic oscillations at all.

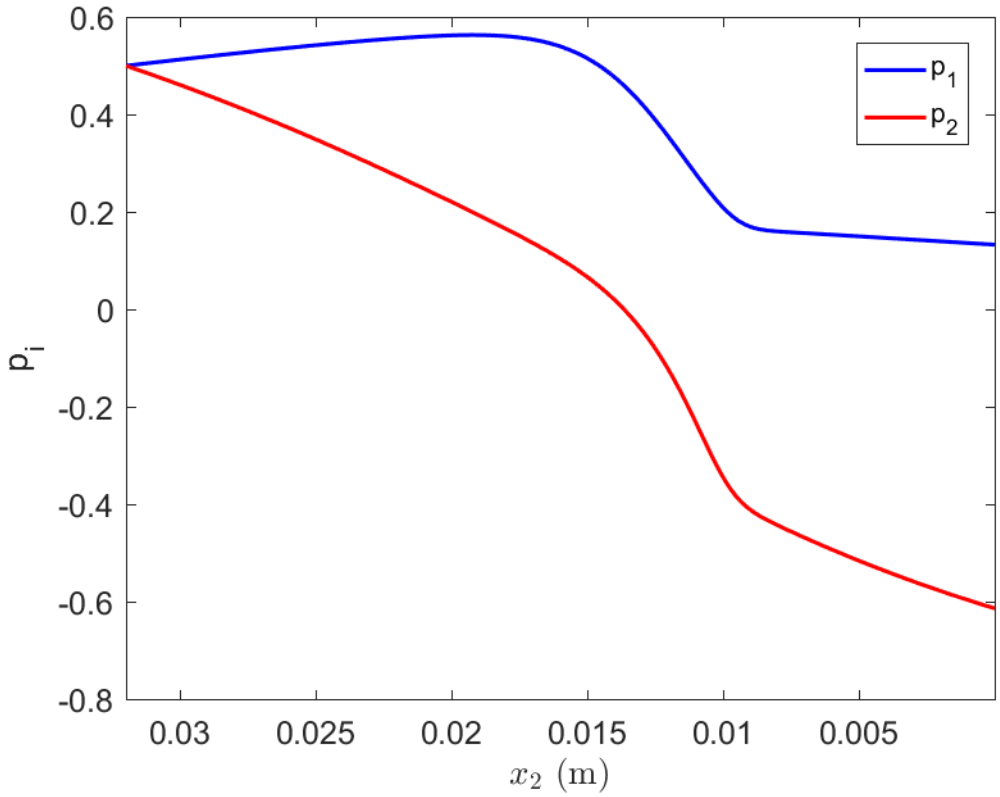

FIG. 3.8. Components of **p** as a function of x_2 – streamline 8

Close to the center of the nozzle the shear forces are not as strong and because of this, the orientation of the fiber does not change rapidly enough for the periodic motion to even be detectable in FIG. 3.8. There is a slow increase in the orientation alignment during the

initial phase of the flow prior to the nozzle contraction zone at $x_2 = 0.012\ m$ and $t = 1.6\ s$, but the elongational effects within the contraction zone completely negate any alignment and dominate the final orientation state even though the elongation region occupies a very small duration of the entire flow history. Another figure showing the plot of the components of **p** as a function of time along streamline 8 could also be shown, but it would not offer much additional insight to this analysis and will thus not be included.

3.5 Orientation Tensors – Jeffery Approach

Calculating the change in orientation of one fiber is a good place to start building up one's understanding of fiber orientation modeling. However, in most industrial settings it would be much more helpful to have an understanding of the orientation state from a group of many fibers. Even though Jeffery's Equation was made for a single fiber, it can be solved many times for many different fibers and then an approximation of the second- and fourth-order orientation tensors can be made. In order to approximate these second- and fourth-order orientation tensors, the integral definitions of the orientation tensors from Equations (2.12) and (2.13) are replaced by summations:

$$A_{ij} \approx \frac{1}{N_f} \sum_{n=1}^{N_f} p_i^n p_j^n \tag{3.4}$$

for the second-order tensor and

$$A_{ijkl} \approx \frac{1}{N_f} \sum_{n=1}^{N_f} p_i^n p_j^n p_k^n p_l^n \tag{3.5}$$

for the fourth-order tensor. In these approximations, N_f is the total number of fibers for which the Jeffery simulation is performed and n denotes the n^{th} fiber. The procedure for solving Jeffery's Equation for many fibers is done by solving Jeffery's Equation, as

discussed in Section 3.4, and repeating it for many different fibers sampled from an initial isotropic orientation distribution function using the ARGA method (see e.g., [36]).

In order to solve Jeffery's Equation in MATLAB with `ode45`, the initial orientations of the fibers must be input into the function. In order to produce random initial orientations for the many different fibers, the Accept-Reject Generation Algorithm is used (see e.g., [36]). The ARGA algorithm will randomly sample discrete samples from any properly defined probability distribution function using a uniform random number generator. In this way a probability distribution that is defined in spherical coordinates may be objectively sampled from using another random number generator. For all cases in the following section, the initial orientation state was considered to be pure random.

Once Jeffery's Equation is solved for a particular streamline selected by the user for each of the many different fibers, the second- and fourth-order orientation tensors at each point along that streamline can be approximated with Equations (3.4) and (3.5). The change in a few of the components of the second- and fourth-order orientation tensors along streamline 0 can be seen, respectively, in FIG. 3.9 and FIG. 3.10. For the rest of this thesis, we choose to graph only a few of the components of A_{ij} and A_{ijkl} for simplicity and again, for the rest of this thesis, although the flow in the nozzle is defined for the x_1-x_2 plane, the orientation state is not constrained to the x_1-x_2 plane. We choose streamline 0 to produce these plots since there are dramatic changes in the fiber orientation due to the high shear and low flow rate along this streamline. It is important to observe that periodic motion can be seen occurring in FIG. 3.9 and FIG. 3.10 for both the

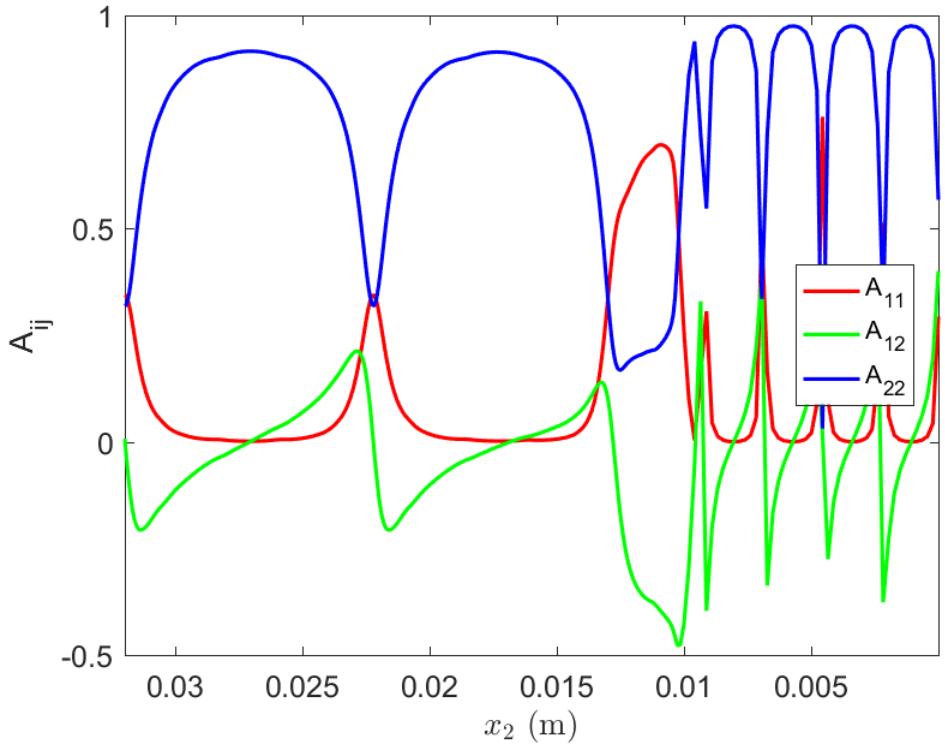

FIG. 3.9. Components of A_{ij} along streamline 0 – Jeffery's model, $N_f = 503$

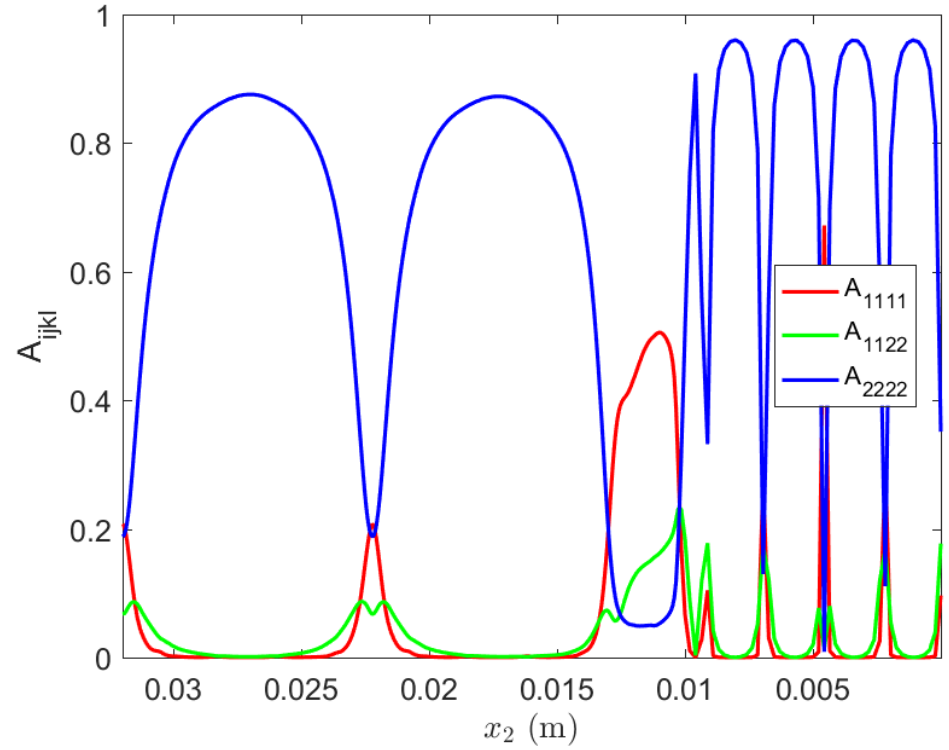

FIG. 3.10. Components of A_{ijkl} along streamline 0 – Jeffery's model, $N_f = 503$

second- and fourth-order orientation tensors over the same x_2-intervals as it did in FIG. 3.6.

In addition, by carefully observing the two initial humps in the A_{22} component in FIG. 3.9 and A_{2222} component in FIG. 3.10, one can notice that they are not perfectly smooth across their tops. This is an artifact of the approximations made in Equations (3.4) and (3.5). Equations (3.4) and (3.5) will approach the smooth value expected from the integral definitions as $N_f \to \infty$. This is impossible to program, but using a larger value for N_f in the orientation tensor approximations would lead to smoother results. We illustrate this by using a larger value of N_f to create FIG. 3.11 and FIG. 3.12. N_f is 503 for generating FIG. 3.9 and FIG. 3.10 and 1124 for generating FIG. 3.11 and FIG. 3.12. Other than the different values of N_f, FIG. 3.11 and FIG. 3.12 are made with the exact same MATLAB code as FIG. 3.9 and FIG. 3.10. The plots in FIG. 3.11 and FIG. 3.12 are, indeed, slightly smoother than the ones in FIG. 3.9 and FIG. 3.10, but not by much. Furthermore, generating FIG. 3.11 and FIG. 3.12 requires almost twice the amount of time as it does to generate FIG. 3.9 and FIG. 3.10 (about 215 seconds using a standard Intel i7-Generation 4 desktop as opposed to about 123 seconds).

In addition to streamline 0, it will also be of some value to look at a streamline closer to the center of the nozzle. Components of the second- and fourth-order orientation tensors along streamline 8 have also been graphed in FIG. 3.13 and FIG. 3.14, respectively. When considering streamline 8 in FIG. 3.13 and FIG. 3.14, we notice that periodic motion is, again, imperceptible, just as it was in FIG. 3.8 for a single fiber traversing streamline 8. Once again, this is due to the smaller shear rates closer to the center of the nozzle. Again the fibers align along the direction of the flow as observed by

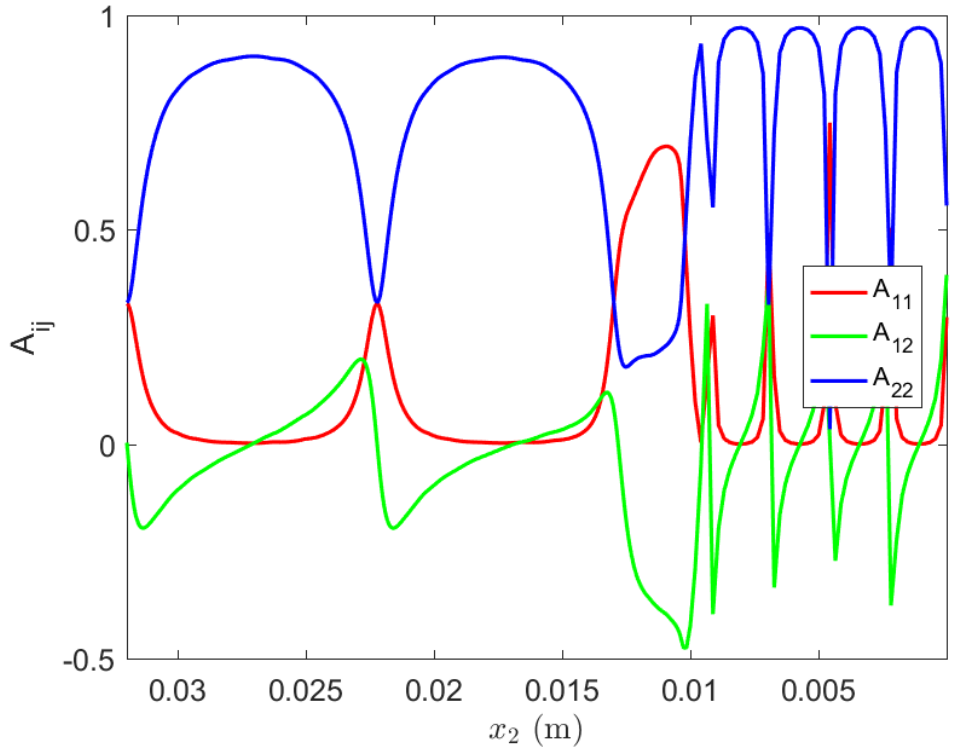

FIG. 3.11. Components of A_{ij} along streamline 0 – Jeffery's model, $N_f = 1{,}160$

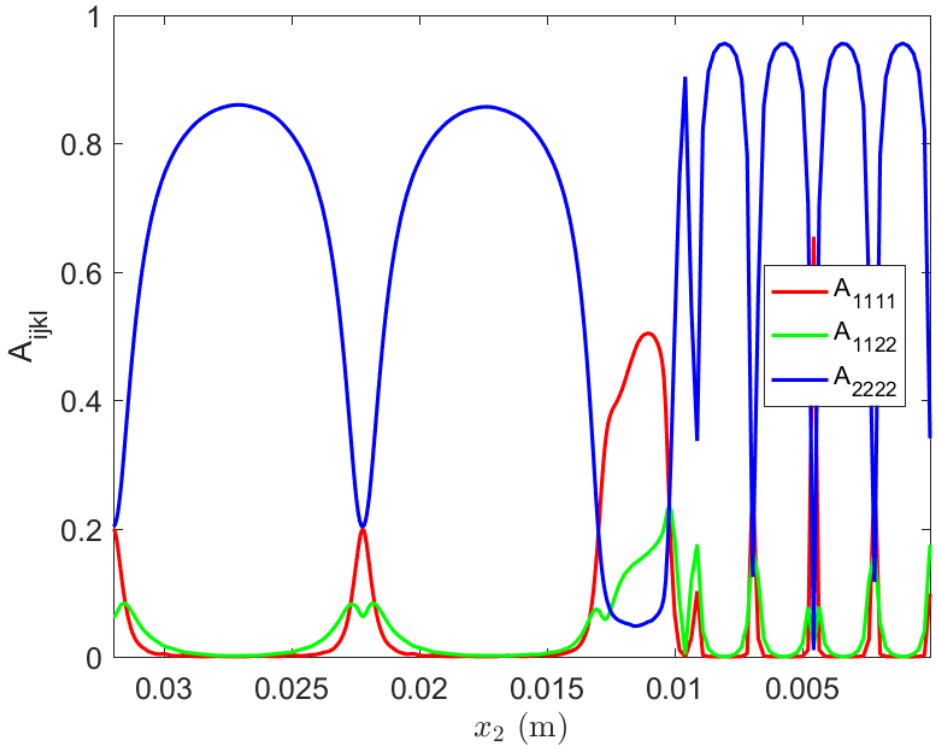

FIG. 3.12. Components of A_{ijkl} along streamline 0 – Jeffery's model, $N_f = 1{,}160$

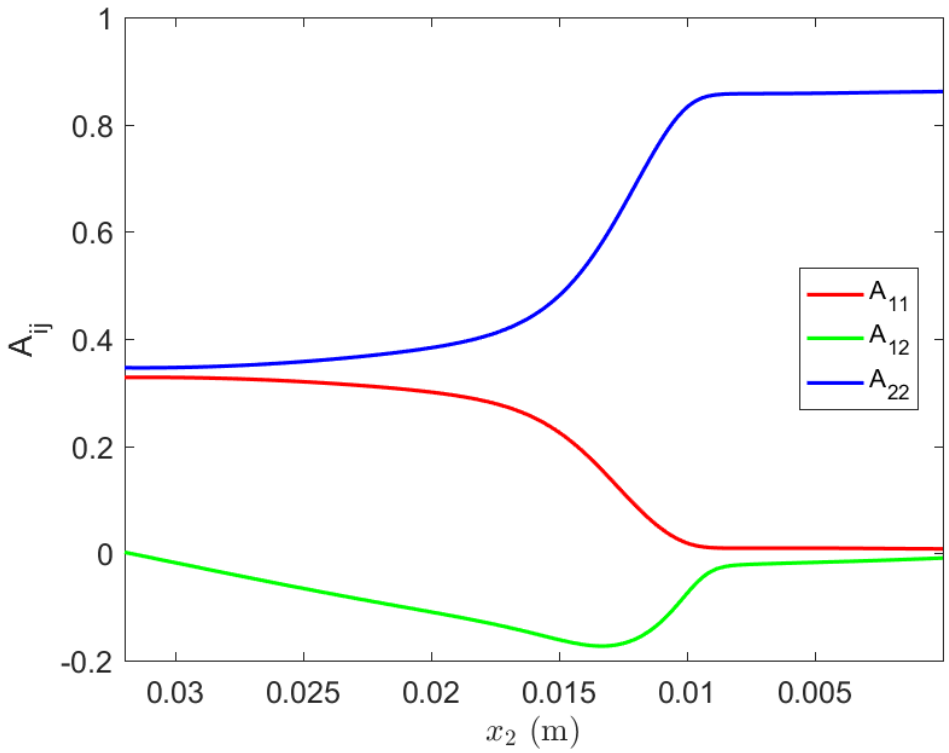

FIG. 3.13. Components of A_{ij} along streamline 8 – Jeffery's model, $N_f = 472$

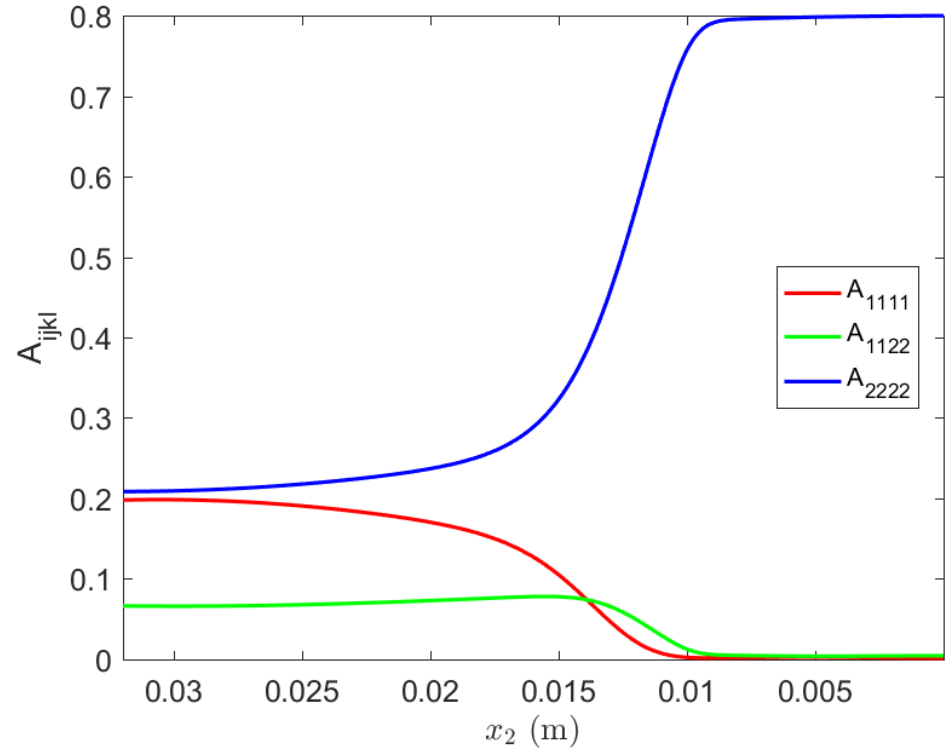

FIG. 3.14. Components of A_{ijkl} along streamline 8 – Jeffery's model, $N_f = 472$

A_{22} and A_{2222} both increasing, and the rate of alignment is greatest in the contraction region.

It is worth explaining why streamlines 0 and 8 were chosen for the graphs in this section of the thesis. For one, streamline 0 was chosen so that it could be clearly shown that periodic motion was occurring, as Jeffery's model predicts in a shearing flow. Secondly, streamline 8 was chosen since it was closer to the center of the nozzle and shows that not all of the streamlines predict severely oscillating changes in orientation since they are not all under the influence of high shear rates.

Another observation to make in FIG. 3.9, FIG. 3.11, and FIG. 3.13 is that the A_{ij} component that tends to be the largest is A_{22}. Even for streamline 0 where A_{22} periodically decreases, it is evident that A_{22} tends to stay near its maximum value longer than it does near its minimum. This means that Jeffery's model predicts that the fibers will tend to align towards the x_2-direction (the vertical direction) for the specific flow field defined in Section 3.2. In other words, the fiber orientation state will no longer be isotropic due to the preferential alignment nor will it be homogeneous spatially as the orientation state along the outer walls is drastically different than those near the center-line. This will have a significant impact upon the material properties as will be demonstrated in later sections.

3.6 Orientation Tensors – IRD and RSC Approaches

Two significant issues arise by using Jeffery's Equation for the solution of many fibers and then approximating the resulting orientation tensors afterwards: (1) the fiber interactions are not accounted for and, (2) the fiber orientation state never reaches a steady state – it just keeps exhibiting periodic motion forever. The latter of these two

issues is effectively a byproduct of the first as the lack of interactions will result in periodic motion, and with all fibers having the same aspect ratio their periods of motion will be identical. In this section, we will look at Folgar and Tucker's Isotropic Rotary Diffusion (IRD) model [29] and the Reduced Strain Closure (RSC) [1] model which both include fiber interaction terms and can therefore lead to steady state values for the orientation state. It turns out that the IRD and RSC models can be adapted to model both dilute (no fiber interactions) and concentrated (with fiber interactions) fiber suspensions, based on the values for their associated empirical parameters. Equations (2.23) and Equation (2.24) are the second-order orientation tensor evolution equations for the IRD and RSC models, respectively, both of which will be investigated throughout the remainder of this chapter.

3.6.1 Dilute Suspensions

When a model based on Jeffery's model does not account for fiber interactions, that model can, at most, only be valid for dilute suspensions where fiber interactions do not have any effect on the change in orientation state. In this section, we will examine how both the IRD model and the RSC model can be reduced down to Jeffery's model. In doing so, the IRD model and RSC model are still valid for dilute suspensions.

3.6.1.1 Comparison of IRD without Fiber Interactions and Discrete Jeffery Model Solutions. In order to model a dilute suspension using Folgar and Tucker's IRD model, we could simplify Equation (2.23) by simply canceling out the last term in the equation. Equivalently, we could choose $C_I = 0$. This yields,

$$\frac{DA_{ij}}{Dt} = -\frac{1}{2}\left(\Omega_{ik}A_{kj} - A_{ik}\Omega_{kj}\right) + \frac{1}{2}\lambda\left(\Gamma_{ik}A_{kj} + A_{ik}\Gamma_{kj} - 2\Gamma_{kl}A_{ijkl}\right) \qquad (3.6)$$

which is exactly the same as the integral form of Jeffery's Equation, Equation (2.2), except that it is in terms of the orientation tensors instead of p_i (see e.g., [36]). It is important to connect this idea back to Section 3.5, where it was discussed how the orientation tensors could be found using Jeffery's Equation. The approach of Section 3.5 first solved Jeffery's Equation for many fibers and then the orientation tensors were approximated using the approximations of the integral forms given in Equations (3.4) and (3.5). Now, Equation (3.6) gives one the opportunity to calculate the second-order orientation tensor *explicitly* with Jeffery's model and there is therefore no need to approximate it using an equation like Equation (3.4). Although this is true, there should be a warning here though. A_{ij} can be explicitly calculated with Equation (3.6), but we must recognize the crucial detail that the fourth-order orientation tensor A_{ijkl} appears in the expression for A_{ij} and thus must be approximated using a closure method. Thus, A_{ij} is calculated explicitly but is only as accurate as the approximation of A_{ijkl} allows it to be. For this thesis, the fourth-order orientation tensor is approximated using a form of the ORT closure of VerWeyst [74]. In addition, in spite of the fact that the orientation states are still *technically* being approximated, the form of Equation (3.6) allows us to define an initial orientation state for `ode45` that is truly, *perfectly* random. That is $A_{ij}^{initial} = \frac{1}{3}\delta_{ij}$ exactly and not just approximately as was the case when we were using Jeffery's model and a finite number of fibers.

We next move on to a comparison test to confirm that solutions from Equation (3.6) with the ORT approximation of the fourth-order orientation tensor A_{ijkl} yield the

same results as Jeffery's model. For the sake of comparing the solutions of the IRD model without fiber interactions with solutions of Jeffery's model from discrete individual fibers, it has been decided to compare the plots of the components of the orientation tensors along streamline 0 from FIG. 3.3. The solutions from solving Jeffery's equation for many discrete fibers has been shown in FIG. 3.9 and FIG. 3.10. For the IRD plots, the full IRD model, Equation (2.23), is written as a function file in MATLAB. In order to solve this function in MATLAB, `ode45` is used again with almost the same inputs as those used in Sections 3.4 and 3.5. These include the time span with 500 steps in time, a relative error tolerance of 10^{-8}, a $\lambda \approx 0.98$ (where $r_e = 10$), time data exported from COMSOL, and velocity gradient data exported from COMSOL. The only two inputs that differ from the inputs of Jeffery's function in MATLAB are the initial orientation state, which is defined as a 1x5 vector containing the independent components of the initial second-order orientation tensor A_{ij} as opposed to the initial orientation of a 3x1 unit vector **p** directed along a single fiber, and an interaction coefficient, C_I. Recall, the full IRD model of Equation (2.23) allows for fiber interactions through the interaction coefficient C_I, but in this present example we set $C_I = 0$ such that there are no fiber interactions.

In solving the IRD model with no fiber interaction in MATLAB, FIG. 3.15 and FIG. 3.16 are produced for streamline 0. It is important to note the similarity between FIG. 3.9 and FIG. 3.15 and also FIG. 3.10 and FIG. 3.16. FIG. 3.9 and FIG. 3.10 were produced by solving Jeffery's equation for a discrete sample of fibers beginning from the individual unit vector **p** and then approximating the solution of the orientation tensors. A difference can be seen in the two smooth humps occurring in the initial stages of the

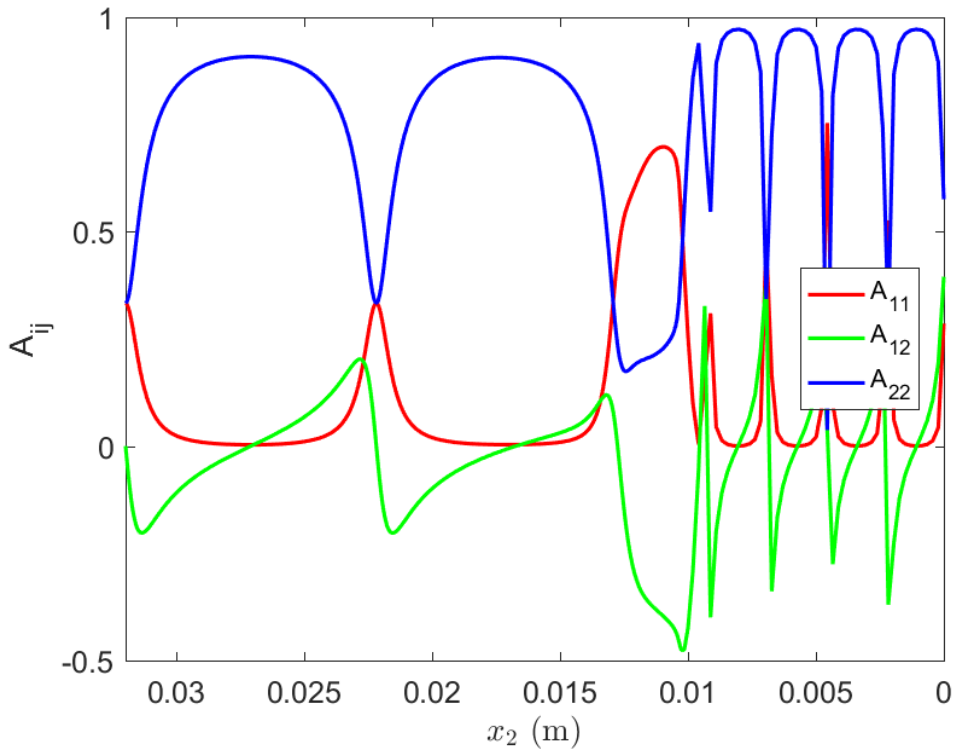

FIG. 3.15. Components of A_{ij} along streamline 0 – IRD model, no fiber interaction

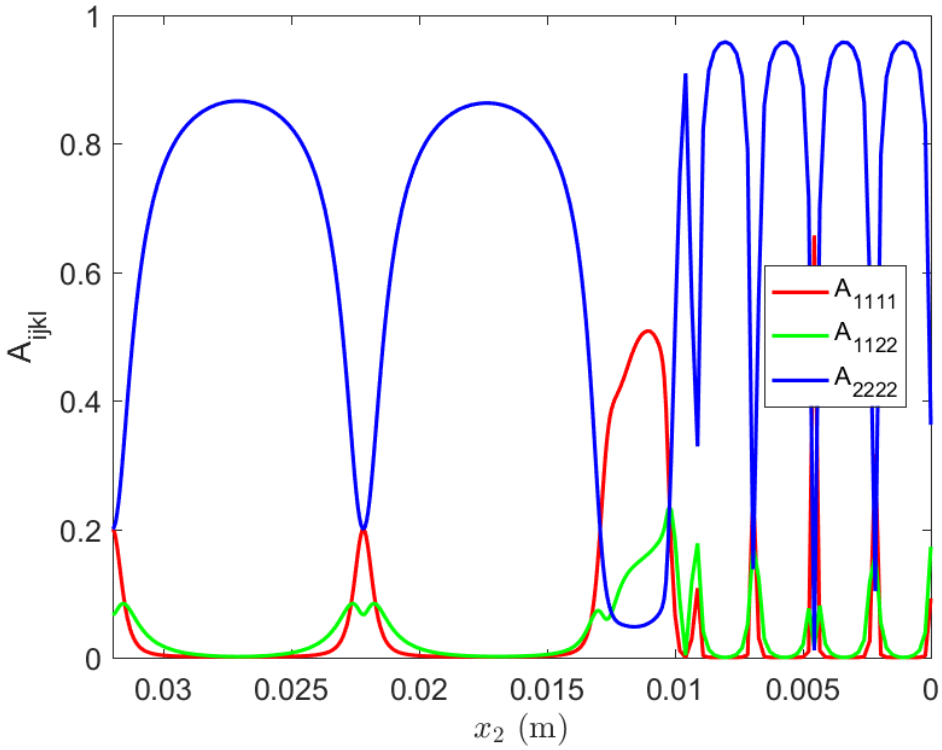

FIG. 3.16. Components of A_{ijkl} along streamline 0 – IRD model, no fiber interaction

nozzle for $0.03\ m > x_2 > 0.012\ m$ in A_{22} and A_{2222} in FIG. 3.15 and FIG. 3.16, respectively, which appear smoother than they do in FIG. 3.9 and FIG. 3.10. In addition, the code to run the IRD model is much more efficient than the code for running Jeffery's model. In the present implementation, the IRD code takes about 4 seconds to complete whereas Jeffery's model for 1100 discrete fibers takes about 3 minutes.

3.6.1.2 Comparison of RSC without Fiber Interactions and Discrete Jeffery Model Solutions. The RSC model can also be adapted to match Jeffery's model exactly. This model is programmed as a function in MATLAB identically to the way the IRD model in Section 3.6.1.1 was programmed, with the only difference being one extra input κ, which appears in Equation (2.24) in order to slow down the fiber alignment rate. When selecting $C_I = 0$ and $\kappa = 1$, the terms $-2\Gamma_{kl}(1-\kappa)\left(L_{ijkl} - M_{ijmn}A_{mnkl}\right)$ and $2\kappa C_I\dot{\gamma}\left(\delta_{ij} - 3A_{ij}\right)$ disappear from Equation (2.24) and one is again left with Jeffery's Equation, in terms of the orientation tensors [i.e. Equation (3.6)]. Thus, if we set $C_I = 0$ and $\kappa = 1$ and solve the RSC model with the exact same conditions as the IRD model in Section 3.6.1.1, we will yet again obtain a figure identical to FIG. 3.15 for the components of A_{ij} along streamline 0. The figure produced with the RSC model with $C_I = 0$ and $\kappa = 1$ is given in FIG. 3.17 to demonstrate that in the limit of no fiber interactions and the slowness parameter κ set to 1 yields identical solutions to those shown in FIG. 3.15 and extremely similar solutions to those shown in FIG. 3.9, the latter of which were produced from a finite number of fibers. The RSC code runs in a similar amount of time as does the IRD model and in the present instance took 4 seconds. A figure identical to FIG. 3.16 (and extremely similar to FIG. 3.10) could also be generated, but at this point we will maintain our focus on the results from the second-order orientation tensor as those results lend

themselves to a broader discussion of the alignment state. The use of the fourth-order orientation tensor will be discussed when the material stiffness and coefficient of thermal expansion tensors are reintroduced in Section 3.7.

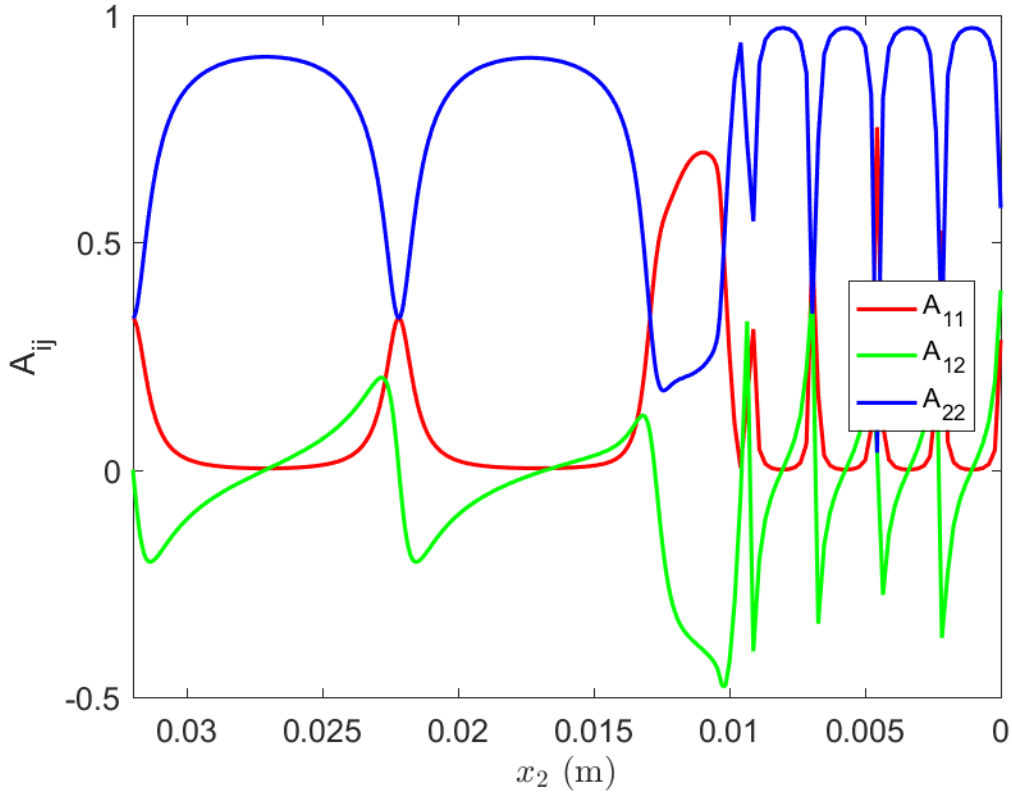

FIG. 3.17. Components of A_{ij} along streamline 0 – RSC model, no fiber interaction

3.6.2 Concentrated Suspensions

The fact that FIG. 3.15, FIG. 3.16, and FIG. 3.17 all match the previous plots made by the Jeffery model in FIG. 3.9 and FIG. 3.10 demonstrates the in-house programs written in MATLAB are being executed properly up to this point. These consistencies also help to demonstrate that the IRD and RSC models are extensions of the Jeffery model. In this section the IRD and RSC models will be utilized for concentrated suspensions to highlight the impact the internal fibers have on the macroscopic orientation state.

3.6.2.1. IRD with Fiber Interactions. To demonstrate the behavior of the IRD model with fiber interactions, we first illustrate the model with a value for the interaction coefficient of $C_I = 10^{-2}$ for streamlines 0 and 8 from FIG. 3.3. For the follow-on studies the results from several different values of C_I will be presented to demonstrate how the model changes as C_I increases. Other than the different values for C_I, the same MATLAB functions and conditions are used in this section as those used in Section 3.6.1 on dilute suspensions.

When $C_I = 10^{-2}$, the IRD model can be used to produce FIG. 3.18 using the in-house MATLAB program described earlier in Section 3.6.1.1. FIG. 3.18 shows components of A_{ij} along streamline 0. The initial orientation state used was completely random, i.e. $A_{ij} = \frac{1}{3}\delta_{ij}$. It is important to notice that with the addition of a fiber interaction term, the periodic motion observed by Jeffery's equation is now gone. It is also noticeable that the fibers are predicted to align mostly in the x_2-direction in the straight parts of the nozzle, but in the tapered, or "funneled," part of the nozzle the fibers tend to rapidly align more in the x_1-direction due to the highly elongational flow experienced within the contraction region of the nozzle. After the contraction region is completed, the fibers again align in the direction of the flow due to the high shear flow in the latter regions of the nozzle. Although and initial orientation state is specified to be completely random for producing FIG. 3.18, the IRD model will predict the fiber orientation state will reach the same steady state values no matter what the initial orientation is. Thus, as long as the nozzle geometry is long enough for the orientation state to reach steady state, the initial orientation state condition does not matter.

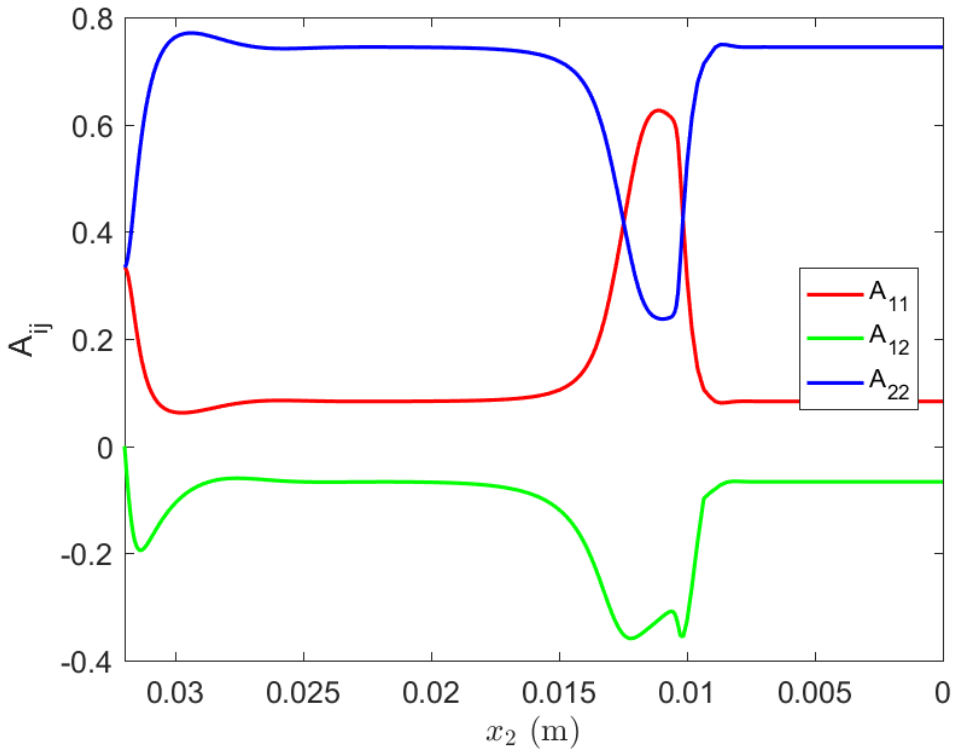

FIG. 3.18. Components of A_{ij} along streamline 0 – IRD model, $C_I = 0.01$

For streamline 8 the results for the second-order orientation tensor are provided in FIG. 3.19. Again, it can be noticed that there is no oscillating of the orientation state and that the highest component of A_{ij} is A_{22}, which means that the fibers are predicted to mostly align in the vertical direction close to the center of the nozzle. There is not a severe dip in A_{22} in the tapered part of the nozzle for streamline 8 like there is for streamline 0. A primary reason for this is that streamline 8 is near the center of the nozzle and the extension/compression effects on the velocity gradient near the centerline are very small. Another way to visualize this is to say that particles that initiate near the center-line in the x_2 direction exhibit very little motion in the x_1 direction.

We will now inspect what happens to the IRD model predictions as the fiber interactions are changed. For this study we let $C_I = 0, 10^{-4}, 10^{-3}$, and 10^{-2}. In addition,

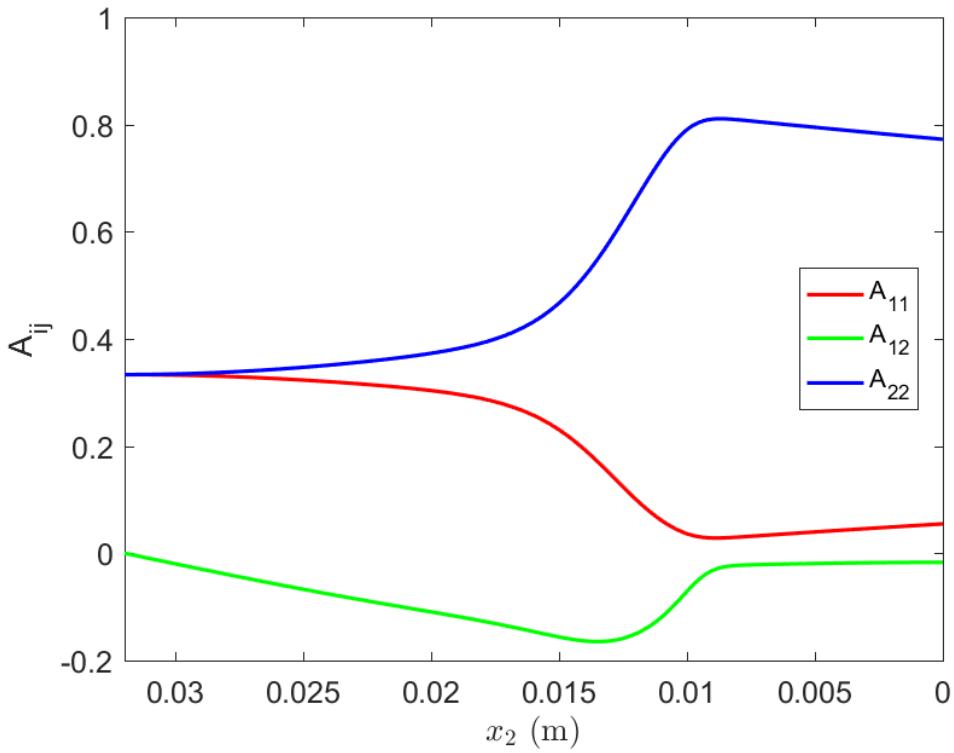

FIG. 3.19. Components of A_{ij} along streamline 8 – IRD model

for the sake of simplicity, we will only choose one component of A_{ij} to examine. Since we have seen that the direction of highest fiber alignment is the x_2-direction, we choose A_{22} to compare IRD models with different values of C_I. A plot of A_{22} with the different values of C_I can be seen in FIG. 3.20. The inputs and code used to generate FIG. 3.20 are identical to those used to generate the previous two figures, except for changes in some plotting commands and the addition of a `for` loop over the different interaction coefficients. It can be seen that increasing the value of C_I tends to dampen the periodic motion more and more. Thus a higher value of C_I allows the fiber orientation state to reach steady state more quickly. The increasing interaction coefficient also has the effect of reducing the overall alignment state, thus with increasing fiber interaction the overall alignment at steady state is lowered.

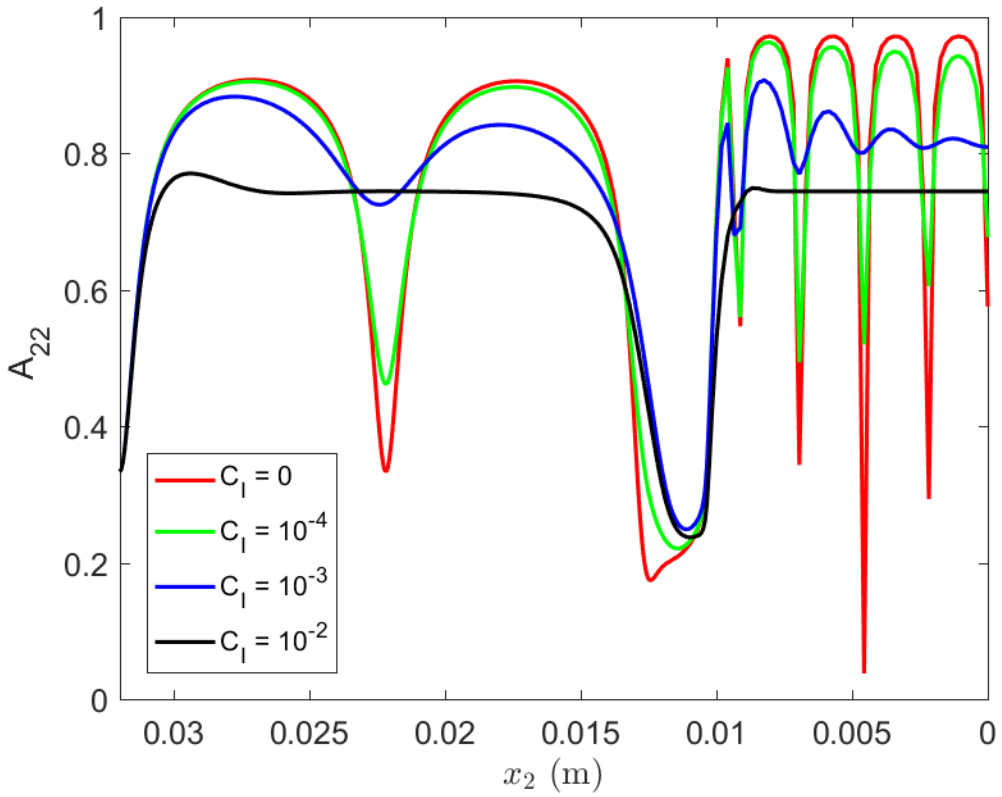

FIG. 3.20. A_{22} along streamline 0 – IRD model with varying C_I

3.6.2.2 RSC with Fiber Interactions. In this section, we illustrate the use of the RSC model over a range of typical values of C_I and κ. This first study is for $C_I = 10^{-2}$ and $\kappa = \frac{1}{30}$. After this, while holding C_I constant, different values of κ will be used to examine the change in the RSC model as κ decreases. The rest of the conditions to be input into the MATLAB functions are the same as those used in the previous section on the IRD model. Thus, the initial orientation state is, once again, completely random, i.e. $A_{ij} = \frac{1}{3}\delta_{ij}$.

When solving the RSC model [i.e. Equation (2.24)] with $C_I = 10^{-2}$ and $\kappa = \frac{1}{30}$ for streamline 0, FIG. 3.21 can be produced. This figure expresses the change in some of

the components of A_{ij} with respect to x_2-position in the 3D printer nozzle. Clearly, FIG. 3.21 is different from FIG. 3.18 for the IRD model with the same interaction coefficient C_I, because the RSC model includes the additional parameter κ that can drastically slow down the rate of alignment. In FIG. 3.18, the components of A_{ij} quickly change and seem to have already arrived at a steady state value before the flow even reaches the tapered part of the nozzle. In contrast, the components of A_{ij} appear to be nowhere near steady state values in the RSC results shown in FIG. 3.21 prior to $x_2 = 0.012$ m (where the tapered part of the nozzle begins). In fact, it appears that the RSC model predicts that the fiber orientation will never even reach steady state prior to the end of the nozzle. Because the fiber orientation state never reaches steady state for the nozzle used in this study, the RSC predictions of the final orientation state could be more sensitive to the initial orientation state than the IRD predictions. Again, the results presented below are for a completely random initial orientation state, $A_{ij} = \frac{1}{3}\delta_{ij}$.

A similar type of plot to FIG. 3.21 can also be made for the evolution of A_{ij} closer to the center of the nozzle, along streamline 8. This plot can be seen in FIG. 3.22. There is very little change in any of the components of A_{ij} along this streamline. It is worth noting that A_{22} is much lower for this streamline than it is for streamline 0. In fact, at the end of the nozzle, the orientation state remains near to the initial orientation state of perfectly random ($A_{11} = A_{22} = A_{33} = 1/3$) for streamline 8. Since the orientation state is different from streamline to streamline at the end of the nozzle according to the RSC model, we will find that when the RSC model is used, the material properties of the final 3D printed bead will also vary from streamline to streamline at the end of the nozzle. This will be discussed in Section 3.7.

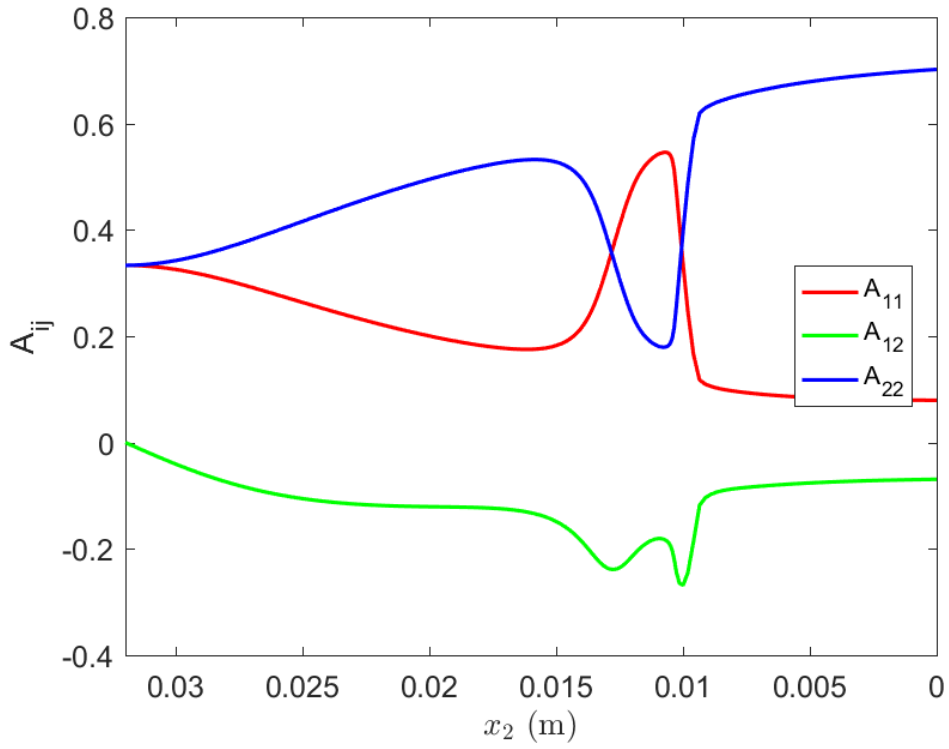

FIG. 3.21. Components of A_{ij} along streamline 0 – RSC model, $C_I = 0.01$, $\kappa = \frac{1}{30}$

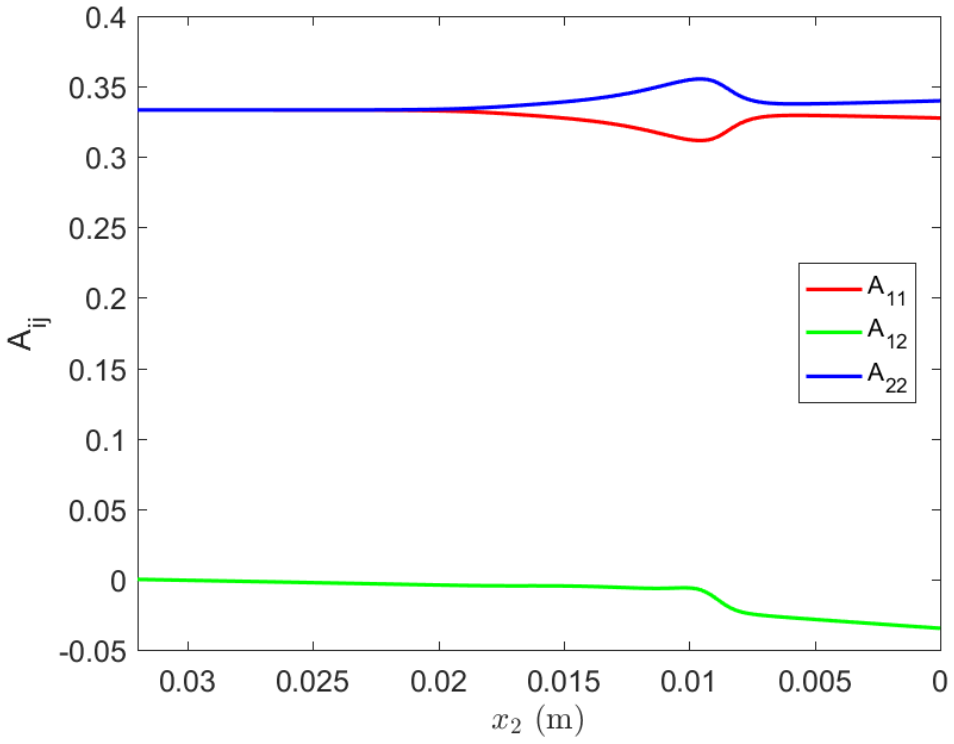

FIG. 3.22. Components of A_{ij} along streamline 8 – RSC model, $C_I = 0.01$, $\kappa = \frac{1}{30}$

This next study investigates the effects of varying the κ term. For this study we will let $C_I = 10^{-2}$ and $\kappa = 1, \frac{1}{10}$, and $\frac{1}{30}$. Again we will just look at the effects of κ on the RSC predictions of A_{22}. These can be seen in FIG. 3.23. From this plot, it can be seen that increasing κ tends to decrease the steepness of the slope of the curves, or in other words, decrease the rate at which the fibers reach their steady state. The red curve with no strain reduction (i.e. $\kappa = 1$) in FIG. 3.23 is exactly the same as the IRD curve for A_{22} in FIG. 3.18 since both have the same interaction coefficient and neither have strain reduction. Observe how the final orientation state at the exit of the nozzle ($x_2 = 0\ m$) varies as a function of the slowness parameter κ. For a long enough nozzle, the RSC model would predict a steady state value of the fiber orientation state.

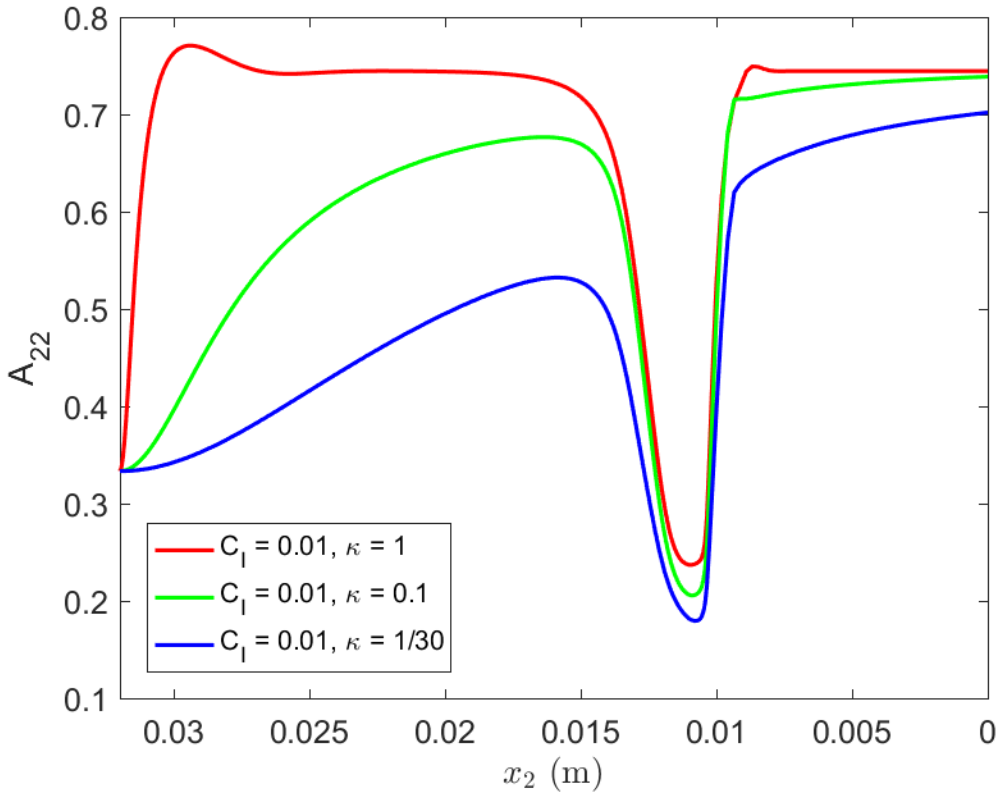

FIG. 3.23. A_{22} along streamline 0 – RSC model with $C_I = 0.01$ and varying κ

3.6.2.3 Fiber Interaction Model Conclusions. Both the IRD and RSC models have been illustrated. Both of these models incorporate fiber interaction and can predict steady state values for the fiber orientation. The RSC model was created to slow down the rate of fiber alignment which was too fast in models such as the IRD. In comparing plots generated with the IRD and RSC models, we have seen that the RSC does, indeed, do this. We have also seen that the IRD and RSC models are truly extensions of Jeffery's model and will give the same results as long as the correct values are chosen for the constant terms C_I and κ.

3.7 Stiffness and Coefficient of Thermal Expansion Tensors along a Streamline

In Section 3.7, the stiffness and CTE properties of a 3D printed, short-fiber composite bead will be examined. Since these properties depend on the fiber orientation state within the composite through Equations (2.45)-(2.52), these properties will change along the flow of the composite just as the orientation state also changes. This section has three main subsections. The first of these, 3.6.1, is concerned with calculating the stiffness and CTE tensor properties as they change along a single streamline. The next subsection, 3.6.2, is concerned with calculating the stiffness and CTE tensor properties at the exit of the 3D printer nozzle. In the third and final subsection we link MATLAB and COMSOL, defining the stiffness tensor properties for a part in COMSOL as those that were calculated at the nozzle exit in MATLAB for subsection 3.6.2. Thus the properties at the nozzle exit will be the properties across the whole, newly created part in COMSOL. Then a tensile test simulation is done on this part in COMSOL and the effective longitudinal Young's modulus is derived. In addition, the stiffness and CTE

tensor properties for another part in COMSOL are defined as those at the nozzle exit and a test for the effective longitudinal CTE is simulated.

3.7.1 Stiffness and CTE along a Single Streamline

In order to get the stiffness and CTE tensors along a single streamline, we use the results from the previous sections for Jeffery's model, the IRD model, and the RSC model for finding the orientation tensors along the streamline. Once the orientation state is identified, the stiffness and CTE tensors can be found along the streamline as well. In essence, this section will show that the material properties along a streamline depend on both the fiber orientation state and, consequently, on the model used to calculate the fiber orientation state.

3.7.1.1 Stiffness and CTE along a single streamline – Jeffery's model. In order to get the stiffness and CTE tensors along a single streamline, we will need to define the material properties of the fiber and polymer matrix, calculate the orientation tensors, calculate the transversely isotropic stiffness tensor using a valid micromechanics model, and finally calculate the orientation averaged stiffness and CTE tensors.

One of the first pieces of information that will be needed in MATLAB is the material properties of the ABS matrix and carbon fiber. The following properties were used for this thesis:

1. Young's modulus of ABS $= 2.25\ GPa$ (this is the average of the lower and upper bounds given by [75])
2. CTE of ABS $= 90 \times 10^{-6}\ (mm/mm)/^{o}C$ (this is the average of the lower and upper bounds given by [76])

3. Poisson's ratio of ABS $= 0.35$ (given by [77])
4. Young's modulus of carbon fiber $= 230\ GPa$ (given by [72])
5. CTE of carbon fiber $= -2.6 \times 10^{-6}\ (mm/mm)/^{o}C$ (given by [72])
6. Poisson's ratio of carbon fiber $= 0.2$ (given by [72])

Two more material characteristics are also needed: the equivalent ellipsoidal aspect ratio, which is chosen to be 10, and the fiber volume fraction. The fiber volume fraction can be calculated since the particular choice of carbon fiber filled ABS used in the experimental phase of this study, which was manufactured by PolyOne, is 13% carbon fiber by weight according to its technical data sheet [78]. In order to convert the weight fraction w_f to a volume fraction v_f, the densities of carbon fiber and ABS are needed. The density of carbon ρ_f is 1.75-1.95 g/cm^3 according to [79] and the density of ABS ρ_m is 1.03-1.07 g/cm^3 according to [80]. After choosing values for the carbon fiber density and ABS density within these ranges, the fiber volume fraction can be calculated using the following formula (see e.g., [81])

$$v_f = \frac{w_f}{w_f + (1 - w_f)\frac{\rho_f}{\rho_m}} \tag{3.7}$$

The minimum value of v_f, given the ranges for ρ_f and ρ_m, is 0.0732 and the maximum value is 0.0837. Averaging these values we get a fiber volume fraction of 0.0784 and will use this value for the remainder of this thesis.

The transversely isotropic stiffness tensor needs to be found using an appropriate micromechanics model, as discussed in the literature review, and in this thesis the Tandon-Weng micromechanics model [63] is used. It is programed as a function M-file and accepts inputs of the fiber and matrix elastic moduli, the fiber and matrix Poisson's

ratios, the fiber volume fraction, and the fiber aspect ratio. From these inputs, the function evaluates the Tandon-Weng micromechanics model and returns the transversely isotropic, fourth-order stiffness tensor in contracted notation. Once this transversely isotropic stiffness tensor is found, it can be input along with the orientation tensors along the streamline and the number of moments in time for which these orientation tensors have been calculated, into another MATLAB function. This function contains Equations (2.45) and (2.46) and can calculate the fourth-order, orientation averaged, stiffness tensor C_{ijkl} along the streamline for any spatial location for which the orientation tensors are known. Once the fourth-order, orientation averaged, stiffness tensor is found along the streamline, it, along with the second-order orientation tensor along the streamline and several other material properties, can be input into a MATLAB function which solves Equations (2.46)-(2.52) for the second-order, orientation averaged, coefficient of thermal expansion tensor α_{ij}.

Select components of the fourth-order stiffness tensor and second-order coefficient of thermal expansion tensor along streamline 0 are plotted in FIG. 3.24 and FIG. 3.25 as functions of x_2. These results from the Jeffery model are obtained using the program written for the IRD model with the ORT closure for $C_I = 0$ as discussed in Section 3.6. It is readily seen that the components of the stiffness tensor in FIG. 3.24 follow the trends of the components of the fourth-order orientation tensor as shown in FIG. 3.10, FIG. 3.12, and FIG. 3.16. This is evidence of the fact that the stiffness is directly related to the fiber orientation state and that higher fiber alignment in a certain direction corresponds to higher stiffness in that direction. This explains why the longitudinal stiffness C_{2222} is generally much higher than the transverse stiffness C_{1111},

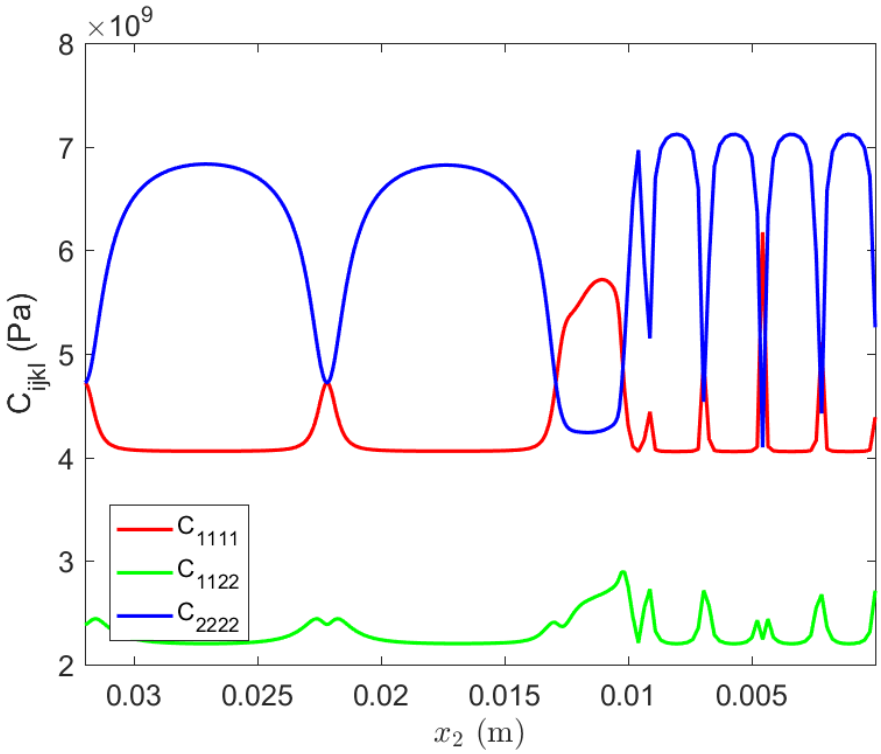

FIG. 3.24. Components of C_{ijkl} along streamline 0 – Jeffery model

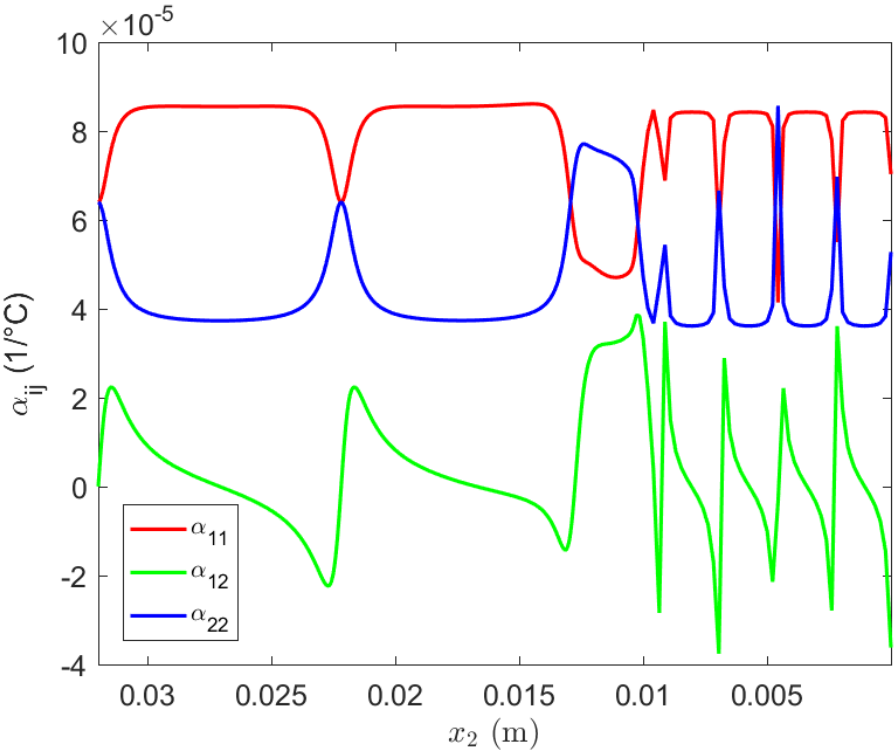

FIG. 3.25. Components of α_{ij} along streamline 0 – Jeffery model

because the fiber alignment in the longitudinal direction is generally much higher than the transverse fiber alignment.

In FIG. 3.25 the plots of the transverse and longitudinal components of the CTE tensor appear similar in shape, respectively, to the plots of the transverse and longitudinal components of the fourth-order orientation tensor reflected over the horizontal axis. This is likely a result of the CTE of the carbon fibers being less than the CTE of the ABS matrix which serves to counteract the thermal expansion of the ABS, especially in the direction the fibers are most highly aligned.

3.7.1.2 Stiffness and CTE along a single streamline – IRD model. The exact same procedure and material properties used in section 3.7.1.1 can also be used with the IRD model, with a nonzero fiber interaction coefficient, to obtain the fourth-order stiffness and second-order thermal expansion tensors. This is done in this section with $C_{\mathrm{I}} = 0.001$, and 0.01. A comparison of the effects of these different interaction coefficients on components of C_{ijkl} and α_{ij} along streamline 0 are shown in FIG. 3.26 and FIG. 3.27, respectively. In these figures, the effect of increasing the fiber interaction term can clearly be seen to increase dampening on the periodic oscillations, allowing the values to reach steady state, or "flat line." The steady state value of the longitudinal stiffness can also be seen to be decreasing as the interaction coefficient increases. In FIG. 3.24, the longitudinal stiffness was often near 7 GPa, whereas in FIG. 3.26, the steady state value for the IRD model with $C_I = 0.01$ is closer to 6 GPa – approximately a full GPa in difference. The CTE results in FIG. 3.27 show that the increasing interaction coefficient increases the longitudinal CTE steady state values, though there does not appear to be as dramatic a difference in steady state values as there was for the longitudinal stiffness. For

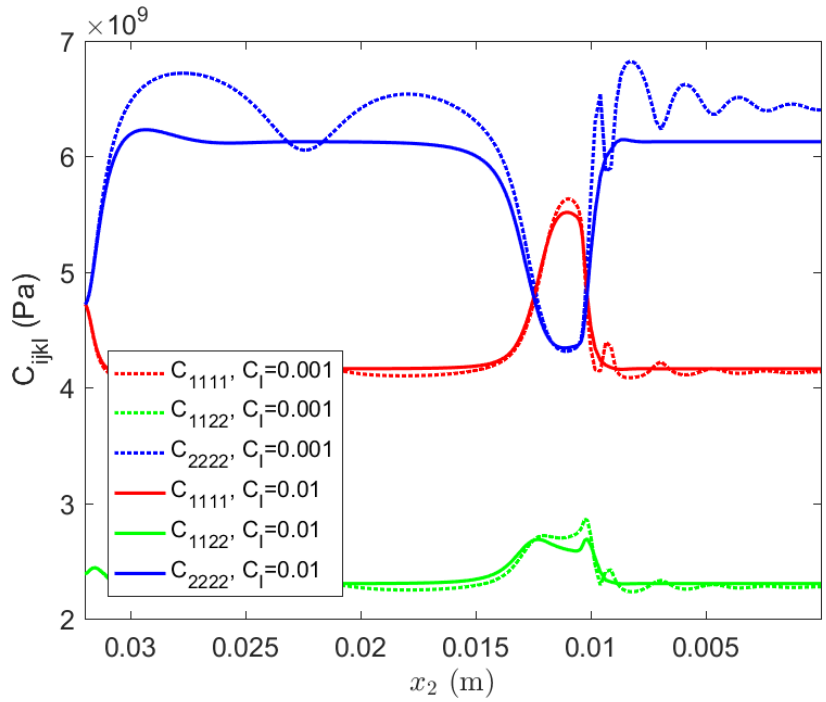

FIG. 3.26. Components of C_{ijkl} along streamline 0 – IRD model, $C_I = 0.001$ (dotted) and $C_I = 0.01$ (solid)

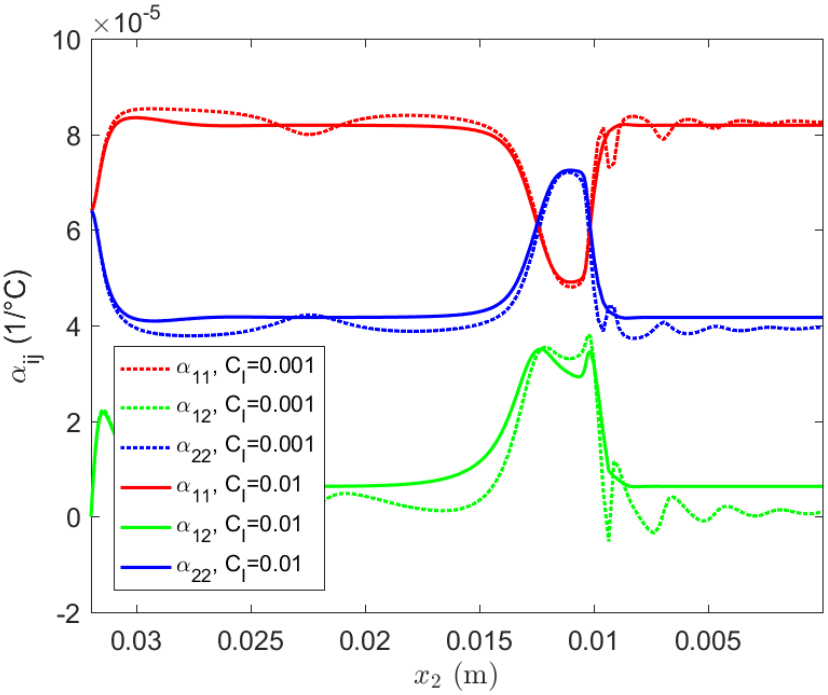

FIG. 3.27. Components of α_{ij} along streamline 0 – IRD model, $C_I = 0.001$ (dotted) and $C_I = 0.01$ (solid)

both the stiffness and CTE tensors, the transverse components are not as affected by changing C_I as the longitudinal components are.

3.7.1.3 Stiffness and CTE along a single streamline – RSC model. Once again, the same procedure and material properties used in the last two sections can be used again except with the RSC model, as opposed to the IRD model. Here we will let $C_\mathrm{I} = 0.01$ and $\kappa = \frac{1}{5}$ and $\frac{1}{30}$ when plotting the stiffness and CTE components so that the effects of different κ values can be observed. Decreasing the value of κ can be seen to reduce the rate at which the stiffness and CTE approach their steady state values. Again, the longitudinal component of the stiffness tensor can be seen following a similar trend as the corresponding longitudinal component of the orientation tensor as depicted in FIG. 3.23.

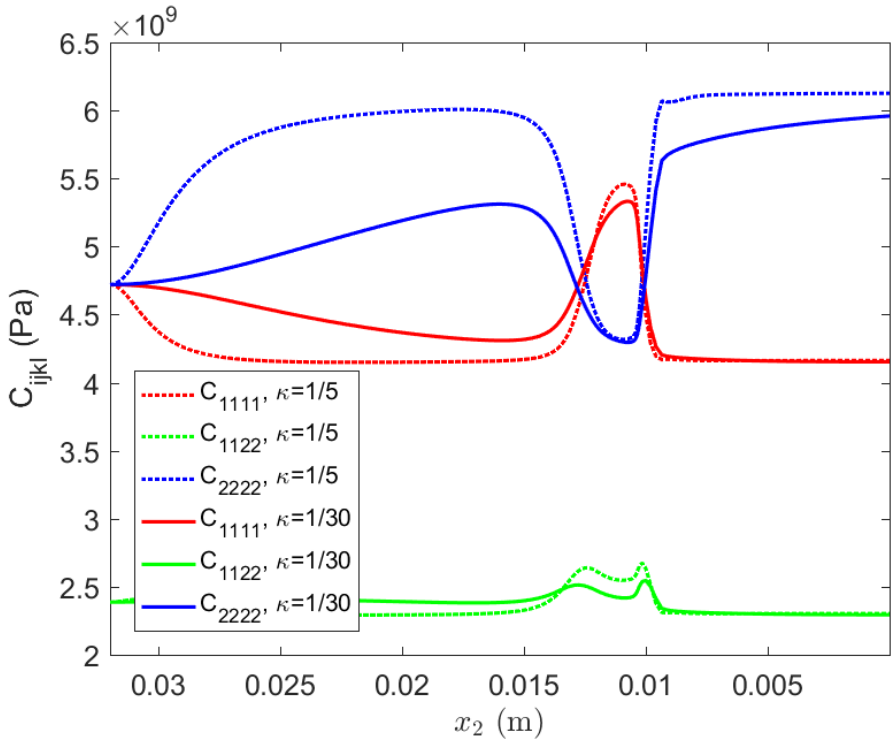

FIG. 3.28. Components of C_{ijkl} along streamline 0 – RSC model, $C_I = 0.01$ and $\kappa = \frac{1}{5}$ (dotted) and $\kappa = \frac{1}{30}$ (solid)

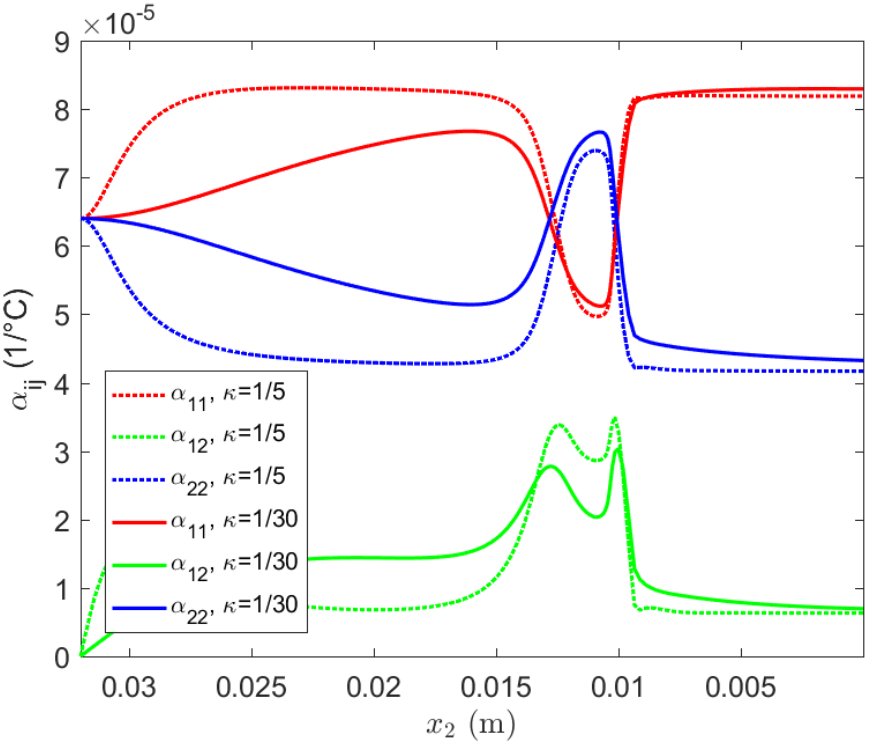

FIG. 3.29. Components of α_{ij} along streamline 0 – RSC model, $C_I = 0.01$, $\kappa = \frac{1}{5}$ (dotted) and $\kappa = \frac{1}{30}$ (solid)

There is a large difference in the transverse and longitudinal stiffness values as κ is decreased, especially in the initial straight portion of the nozzle leading down to the tapered part of the nozzle around $x_2 = 0.012\ m$. This can also be said of the transverse and longitudinal CTE values, which appear similar in shape to the corresponding stiffness values reflected over the horizontal axis. At the nozzle exit, however, the disparities between the final values of the stiffness components are not as great as they were for the IRD model and it appears likely that they would decrease even more were the nozzle to be lengthier since the RSC model with $\kappa = \frac{1}{30}$ does not reach steady state for the nozzle geometry defined in this study. The same goes for the CTE tensor components, although these appear close to steady state values by the end of the nozzle.

3.7.2 Stiffness and CTE at the Nozzle Exit

In order to calculate the stiffness and CTE tensors horizontally across the nozzle exit, we first solve for the stiffness and CTE tensors along *each* streamline and collect the values at the end of each streamline. These collected values at the end of each streamline would correspond to the stiffness and CTE tensors of the deposited extrudate if the die swell were neglected (see e.g., [23] for methods to address the die swell issue). Again, this is done with Jeffery's model, the IRD model, and the RSC model. In the previous sections of this thesis, the velocities and velocity gradients were calculated along 20 streamlines. However, 20 points across the nozzle exit did not produce smooth plots, thus in the following three subsections, the velocities and velocity gradients are calculated in COMSOL along 70 streamlines and exported to MATLAB for calculating the fiber orientation state and, subsequently, the stiffness and CTE tensors. The nozzle geometry was not changed and neither were the initial conditions, boundary conditions, or the finite element mesh.

3.7.2.1 Stiffness and CTE at the nozzle exit – Jeffery's model. When solving Jeffery's model for all 70 streamlines, we compute the solution using the IRD model with the ORT closure and with no fiber interactions accounted for (i.e., $C_I = 0$). The orientation state at the end of the flow along each streamline, corresponding to the nozzle exit, is then used to compute the stiffness and coefficient of thermal expansion tensors using the previously discussed micromechanics methods. Select components of the stiffness and the CTE tensors are plotted at the nozzle exit in FIG. 3.30 and FIG. 3.31 as a function of x_1.

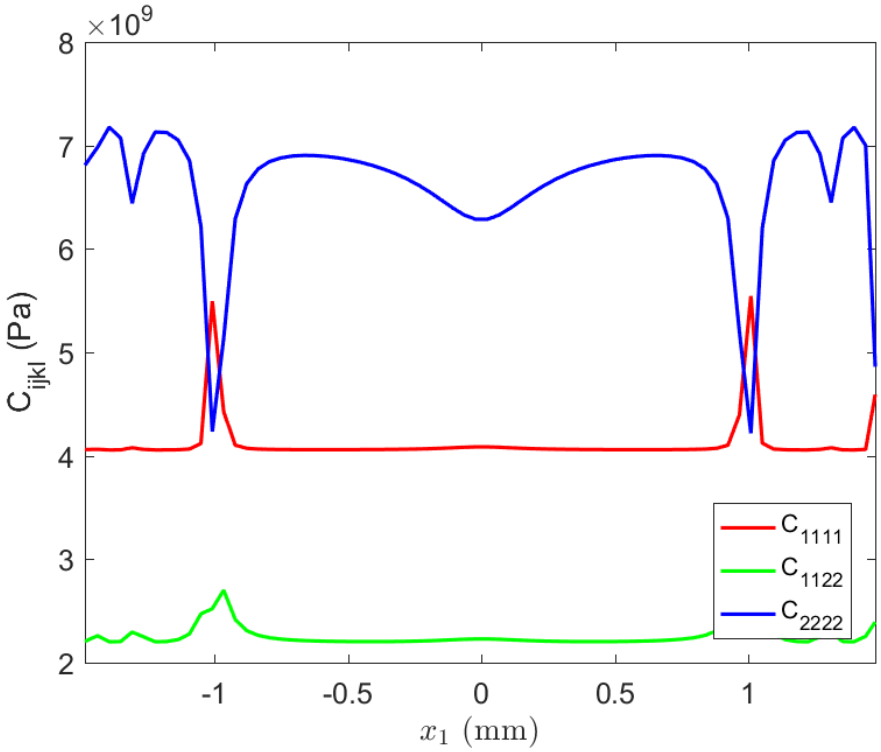

FIG. 3.30. Components of C_{ijkl} at the nozzle exit – Jeffery's model

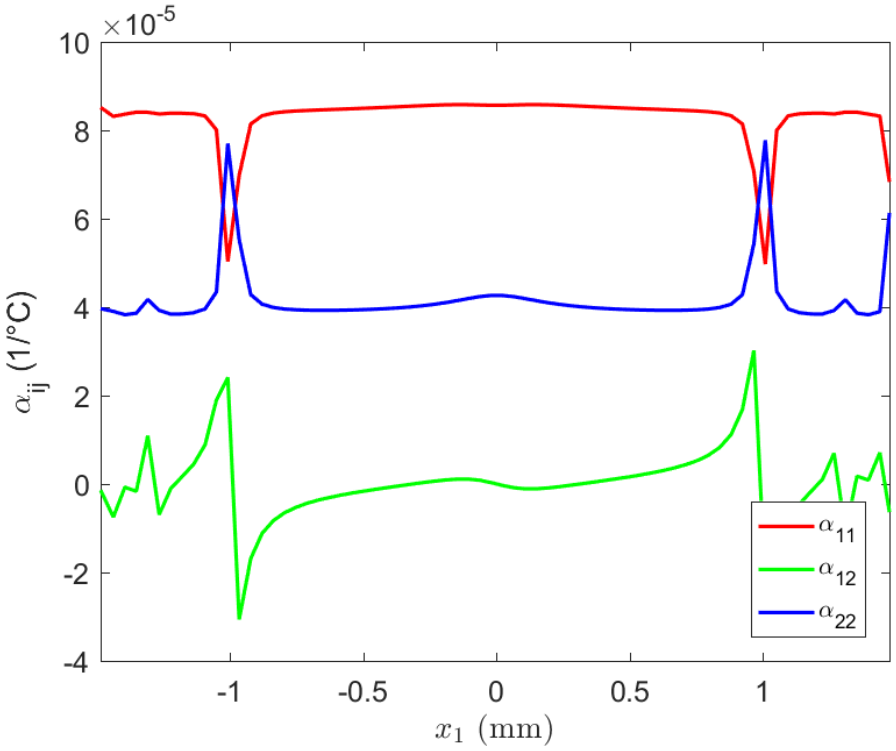

FIG. 3.31. Components of α_{ij} at the nozzle exit – Jeffery's model

The plots in FIG. 3.30 and FIG. 3.31 contain sharp discontinuities and these can be explained by the periodic motion predicted by Jeffery's model. For most of the length of each streamline, the fiber orientation state is biased in the x_2-direction. However, since Jeffery's model predicts that an orientation state along a streamline will change periodically, there is a chance that at the moment in time that the polymer flow reaches the nozzle exit, the fiber orientation state along individual streamlines will not be in the flow direction. There is a much greater possibility of seemingly chaotic behavior along the streamlines that are near the wall of the nozzle since there is more shearing force near the wall and the frequency of tumbling out of alignment as a function of vertical position increases with increasing shear. Near the center of the nozzle, the shear rate is quite small relative to the nozzle length and thus the fibers do not tumble out of alignment (recall FIG. 3.13 and FIG. 3.14). This is why the center of the plots in FIG. 3.30 and FIG. 3.31 are smooth and the sharp discontinuities only appear closer to the nozzle walls.

The origin of this seemingly unusual behavior is emphasized in FIG. 3.32 which contains a plot of select fourth-order orientation tensor components. It can be seen that the stiffness tensor tends to follow the same trend as the orientation tensor. That is, the direction of highest fiber alignment tends to have the highest stiffness and the direction of least fiber alignment tends to have the lowest value for stiffness, as should be expected after seeing the results in Section 3.7.1. Again, as was seen in Section 3.7.1, the transverse and longitudinal CTE tensor components also appear to follow the trends in the corresponding components of the fourth-order orientation tensor, reflected over the horizontal axis. That is, the direction of highest fiber alignment seems to be the direction in which the CTE tends to be the smallest and the direction of least fiber alignment seems

to be the direction where the CTE tends to be the largest, due to the CTE value of carbon fiber being less than the CTE of the ABS matrix.

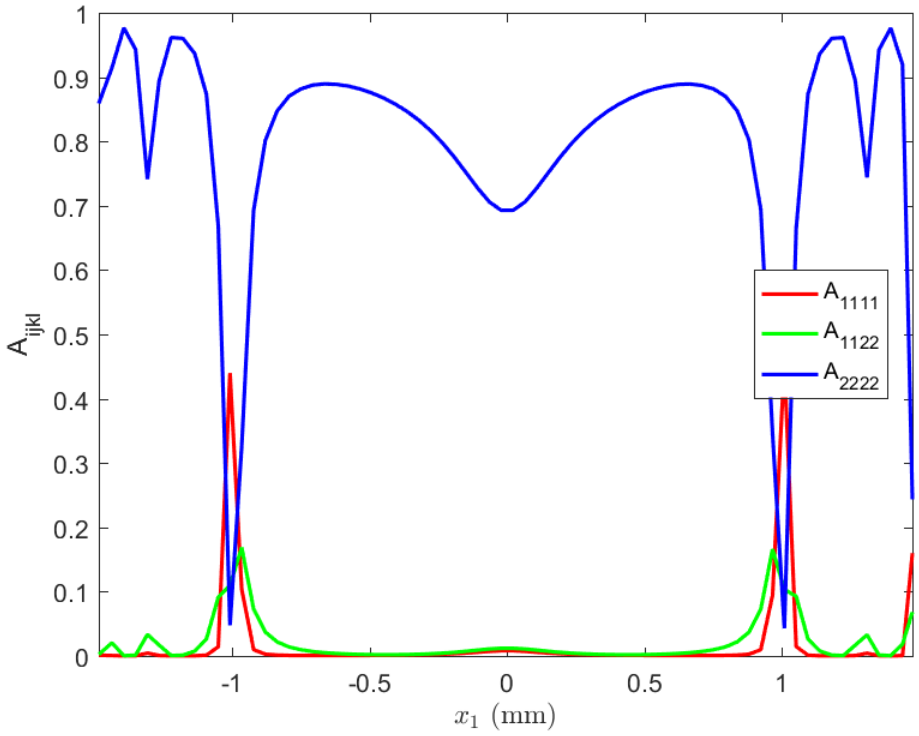

FIG. 3.32. Components of A_{ijkl} at the nozzle exit – Jeffery's model

3.7.2.2 Stiffness and CTE at the nozzle exit – IRD model. The sharp discontinuities in FIG. 3.30 – FIG. 3.32 are non-physical for semi-dilute and concentrated suspensions. The following study of the stiffness and CTE tensors is of the IRD model as a function of increasing fiber interaction, with $C_I = 0.001$ and $C_I = 0.01$. The results of the orientation state at the nozzle exit from Section 3.7.2.2 serve as inputs for the micromechanical modeling, and the results for select components of the stiffness tensor and CTE tensor are provided, respectively, in FIG. 3.33 and FIG. 3.34. Observe in FIG. 3.33 and FIG. 3.34 that as the interaction coefficient increases the oscillations in the properties diminish. In addition, upon visual inspection, it appears an increasing

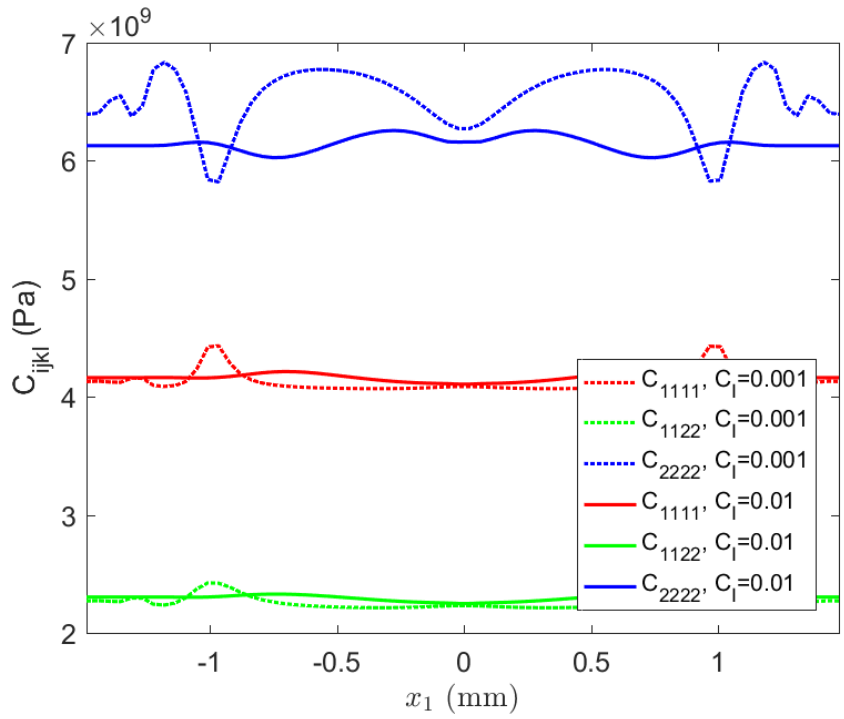

FIG. 3.33. Components of C_{ijkl} at the nozzle exit – IRD model, $C_I = 0.001$ (dotted) and $C_I = 0.01$ (solid)

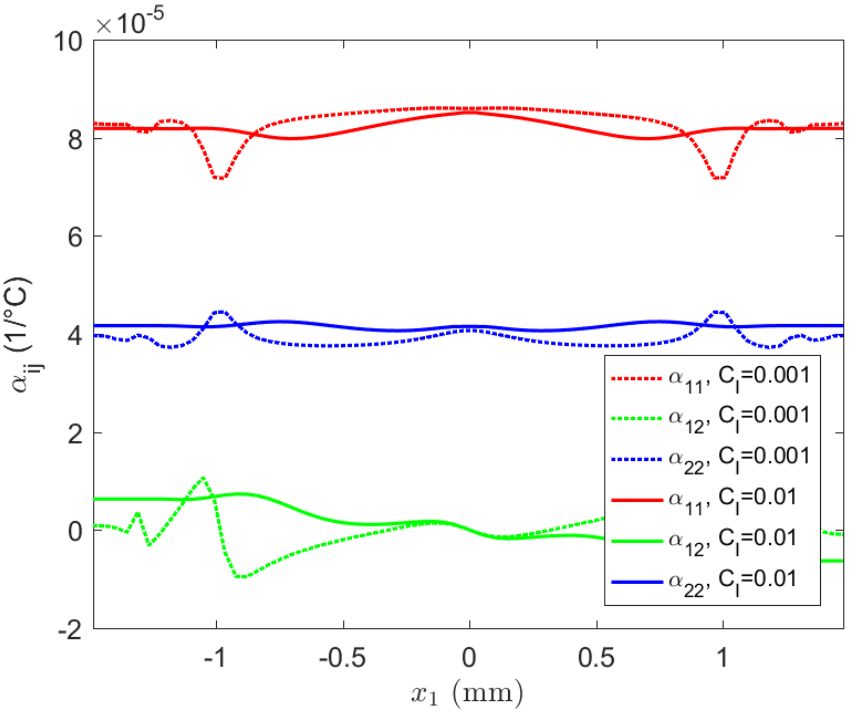

FIG. 3.34. Components of α_{ij} at the nozzle exit – IRD model, IRD model, $C_I = 0.001$ (dotted) and $C_I = 0.01$ (solid)

interaction coefficient decreases the overall mean value for the longitudinal stiffness in the x_2 direction. It is interesting to note the degree of anisotropy predicted in the final processed bead. The stiffness properties in the print direction are predicted to be significantly higher than that of the transverse direction, with the opposite being true for the thermal expansion behavior.

3.7.2.3 Stiffness and CTE at the nozzle exit – RSC model. We next turn to the RSC model which will have the effect of slowing down the orientation kinetics and for the present study we set $C_I = 0.01$ and vary the slowness parameter from $\kappa = \frac{1}{5}$ to $\kappa = \frac{1}{30}$. The resulting stiffness and coefficient of thermal expansion tensors at the nozzle exit are provided in FIG. 3.35 and FIG. 3.36, respectively.

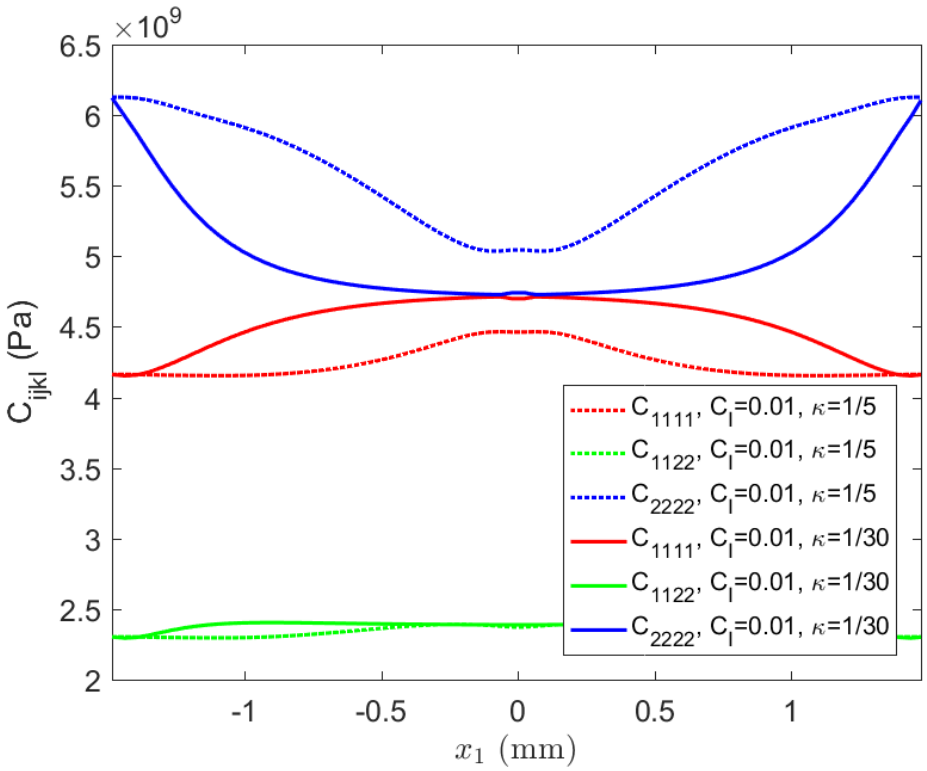

FIG. 3.35. Components of C_{ijkl} at the nozzle exit – RSC model, $C_I = 0.01$, $\kappa = \frac{1}{5}$ and $\kappa = \frac{1}{30}$

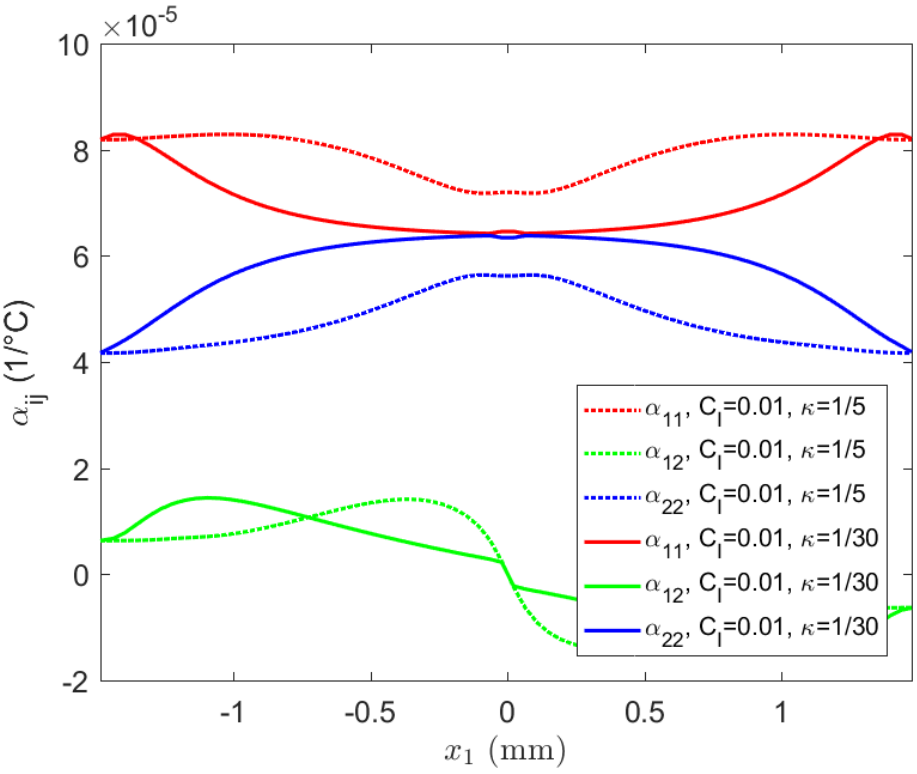

FIG. 3.36. Components of α_{ij} at the nozzle exit – RSC model, $C_I = 0.01$, $\kappa = \frac{1}{5}$ and $\kappa = \frac{1}{30}$

Notice the significant variation of the various stiffness and CTE tensor components as a function of x_1 as compared to that of the IRD results in FIG. 3.33 and FIG. 3.34. The RSC model predicts a significant change in the stiffness and CTE when the strain reduction factor is reduced. In addition, the RSC model predicts more of a *U*-shaped longitudinal stiffness and transverse CTE than the IRD model does, with greater values near the nozzle walls, and more of an inverted *U*-shape for the transverse stiffness and longitudinal CTE than the IRD model.

Since, intuitively, the stiffness should be greatest in the direction of highest fiber alignment, this is in agreement with FIG. 3.21 and FIG. 3.22 which show that the fibers

exhibit more vertical alignment at the nozzle exit closer to the edge of the bead, like along streamline 0, than they do closer to the center of the bead, like along streamline 8. As has been the case, the CTE exhibits almost the opposite behavior as the stiffness in that the longitudinal CTE is *lowest* near the edges of the bead and highest near the center. Observe that as $\kappa \to 0$ the alignment rate is so small that at the center of the channel there is essentially no change in orientation. In the present study the initial alignment was set to uniformly random, and this is essentially unchanged in the center of the channel for $\kappa = \frac{1}{30}$ and thus the stiffness and CTE tensors remain isotropic in the center of the flow channel.

3.7.3 Effective Bulk Longitudinal Stiffness and Coefficient of Thermal Expansion

The final contribution of the modeling effort is to form the connection between the spatially varying stiffness and CTE tensors to that of the bulk response. The purpose being to relate the model predictions that provide a spatial response to that of a fabricated test specimen subjected to a macroscopic tensile or CTE test. A key part of this last task involves linking MATLAB and COMSOL so that the stiffness and CTE tensor components can be uploaded into COMSOL for defining the material properties of a part.

3.7.3.1 Effective longitudinal stiffness. First, in order to find the effective longitudinal stiffness E_{22} of the extrudate itself, a simple tensile bar is made in COMSOL with the same cross sectional dimensions to that of the nozzle exit from the flow modeling. This assumption that the width of the sample is the same as that of the nozzle diameter is not quite true due to the extrudate swell discussed in section 2.1.6 (see e.g., [23,24]) but the die-swell is left to the related study done by [24]. Thus, a simple 2-

dimensional rectangle with width 3 mm and height 30 mm is defined in COMSOL for the tensile sample as shown in FIG. 3.37. In order to simulate a tensile test on this specimen, a boundary condition analogous to that of a tensile test stage must be defined for the FEA computations. These include prescribed displacements and a prescribed load. The entire bottom of the tensile bar is given a prescribed displacement of 0 in the x_2-direction ($u_2 = 0$). In addition, the center point of the bottom of the bar has a prescribed displacement of 0 in the x_1-direction ($u_1 = 0$), which prevents translational movement. The load applied to the bar is 6 MPa across the whole top side of the bar in the positive x_2-direction.

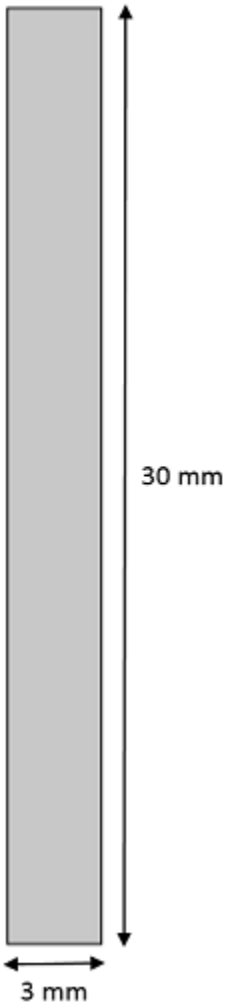

FIG. 3.37. Tensile bar geometry in COMSOL

The finite element analysis within COMSOL is constructed to accept as an input the spatially varying stiffness as defined in a MATLAB M-File with the material properties for the fiber and the matrix defined in Section 3.7.1.1. The tensile sample is modeled as a linearly elastic material with a fourth order anisotropic stiffness tensor. The created M-File accepts as inputs the transverse spatial location corresponding to the transverse position from the nozzle exit. The file then searches for the corresponding second-order orientation tensor at the COMSOL requested spatial position using an interpolating spline to allow for stiffness to be a smooth and continuous function even though there are a finite number of streamlines passing through discrete points. Since there are 70 streamlines for this flow, A_{ij} is found at 70 points in the flow at the nozzle exit, and in this section results from both the IRD and RSC are used. Once the second-order orientation tensors along the nozzle exit have been found, they are stored along with their x-coordinates in a `.mat` file. When the contracted, fourth-order, anisotropic stiffness tensor is defined in COMSOL for the tensile bar, it is defined in terms of an in-house MATLAB function that uses this A_{ij} data stored in the `.mat` file. This MATLAB function takes as inputs an x_1-coordinate and the indices for a particular component of the stiffness tensor. Whenever COMSOL needs the stiffness at a particular coordinate location within the bar it will call this MATLAB function and give it an x_1-coordinate and the indices (i, j, k, l) for the particular component of the stiffness tensor that it needs. The MATLAB function loads the A_{ij} data stored in the `.mat` file and linearly interpolates between the data. This enables COMSOL to obtain any component of the stiffness tensor at any point within the tensile bar as needed, which means that COMSOL essentially has the full anisotropic stiffness tensor at any point within the part.

After the anisotropic stiffness tensor has been defined as a property of the tensile bar in COMSOL, COMSOL can be used to run a Finite Element Analysis of the tensile test simulation. After the Finite Element Analysis has been done, the effective longitudinal modulus is derived using the following equation

$$E_{22} = \frac{\sigma_{22}}{\varepsilon_{22}} \tag{3.8}$$

where σ_{22} is the stress in the x_2-direction (6 MPa), and ε_{22} is the strain in the x_2-direction, where $\varepsilon_{22} = (x_2\ displacement)/(original\ height)$. The effective longitudinal modulus of the entire extrudate is dependent on the spatially varying stiffness tensor, which is itself dependent on the fiber orientation state.

Multiple effective moduli for the entire part have been calculated for both the IRD and RSC models with varying fiber interaction levels and slowness parameters which are labeled in Table 3.1.

Table 3.1. Effective longitudinal Youngs modulus, E_{22}

Model Used	E_{22} (GPa)
IRD – $C_I = 0.001$	4.84
IRD – $C_I = 0.01$	4.43
RSC – $C_I = 0.01$, $\kappa = 1/5$	3.90
RSC – $C_I = 0.01$, $\kappa = 1/10$	3.68
RSC - $C_I = 0.01$, $\kappa = 1/30$	3.37

Prior to simulating the COMSOL tensile tests, the IRD and RSC models were calculated for 500 time steps, relative error tolerances of 10^{-8}, initial orientation states of $A_{ij} = \frac{1}{3}\delta_{ij}$, $\lambda \approx 0.98$ (with $r_e = 10$), and for the same nozzle geometry, initial conditions, and boundary conditions that were articulated in Section 3.2. As before the IRD and RSC models also took inputs of the time and velocity gradient data exported from the

COMSOL polymer melt flow simulation. The results for E_{22} from the tensile test simulations were generated from a finite element mesh of 10 elements along the height of the tensile bar and 70 elements along the width of the tensile bar. Rectangular elements were chosen since the shape of the sample is rectangular.

Since we are now able to calculate the effective longitudinal Young's Modulus for a sample of a 3D printed bead, we can also look at how certain parameters may affect the modulus. After all, the point of this research is to be able to understand the effects of processing on the material properties well enough to determine how the part may be optimized for its intended application. One parameter that effects the modulus is the equivalent ellipsoidal aspect ratio r_e of the fibers. This parameter was chosen partly because the aspect ratio of the fibers was not provided by PolyOne and thus was not known precisely for this study. FIG. 3.38 shows the elastic modulus as a function of equivalent ellipsoidal aspect ratio for a range typical of short fibers. The modulus was calculated with results from the RSC model with $C_I = 0.01$ and $\kappa = \frac{1}{30}$. It can be seen that the modulus tends to increase with increasing r_e, but not by much. Over the range of short-fiber lengths shown, the maximum percent difference, given in Equation (3.9), is very low:

$$\begin{aligned} \%\, difference &= \left|\frac{(first\ E_{22}) - (last\ E_{22})}{[(first\ E_{22}) + (last\ E_{22})]/2}\right| \cdot 100\% \\ &= \left|\frac{(3.3687 \times 10^9\ GPa) - (3.3741 \times 10^9\ GPa)}{[(3.3687 \times 10^9\ GPa) + (3.3741 \times 10^9\ GPa)]/2}\right| \cdot 100\% \\ &\approx 0.1602\ \% \end{aligned} \tag{3.9}$$

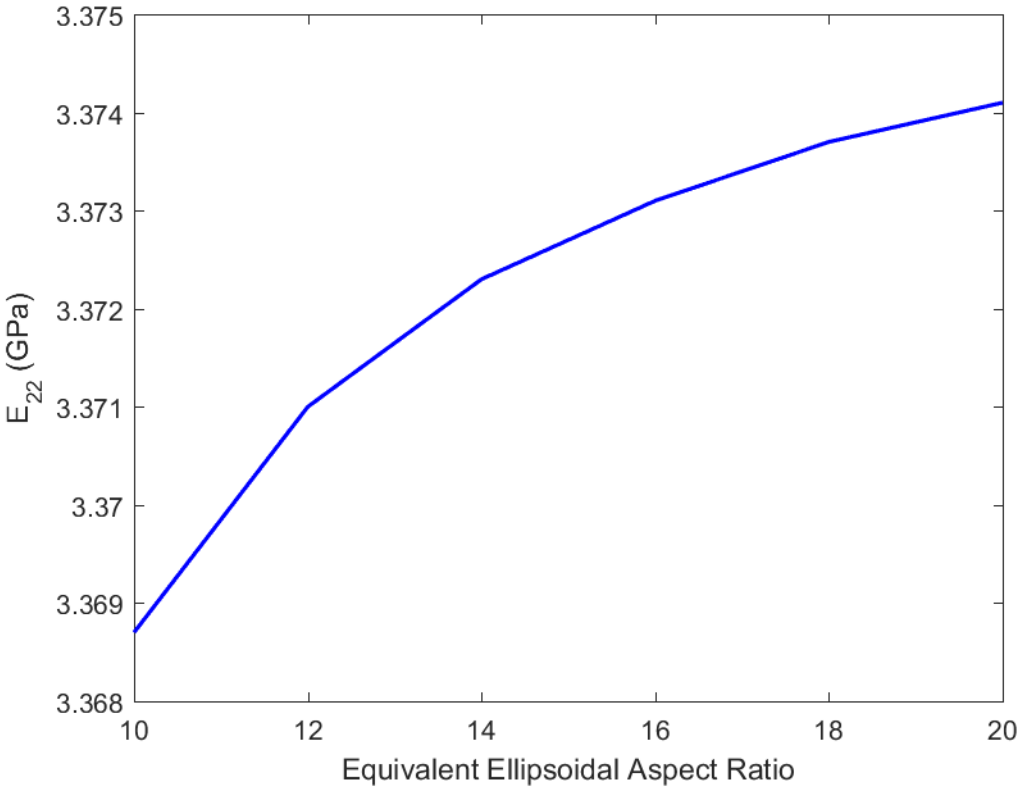

FIG. 3.38. Young's Modulus as a function of Equivalent Ellipsoidal Aspect Ratio

3.7.3.2 Effective longitudinal CTE. A test for the effective longitudinal coefficient of thermal expansion can also be simulated in COMSOL. For this test, the sample geometry is as shown in FIG. 3.39. The prescribed displacements are the same for this section as they were in Section 3.7.3.1 with the entire bottom of the sample being prescribed as zero displacement in the x_2-direction ($u_2 = 0$) and the point on the bottom center of the sample being prescribed to a zero displacement in the x_1-direction ($u_1 = 0$). However, this time there is no applied load. Instead, there is an applied temperature increase of 1^{o}C to the top of the sample, which is initially set to 0^{o}C throughout its entirety, and the other three sides are insulated. When defining the material properties, the anisotropic stiffness tensor is defined exactly as it was in Section 3.7.3.1. In addition to this, an anisotropic second-order coefficient of thermal expansion tensor is also

defined. This is defined by using a similar method that was used for the stiffness tensor: an in-house MATLAB function loads A_{ij} data at the nozzle exit and, by the help of linear interpolation, can calculate the CTE tensor at any point within the sample.

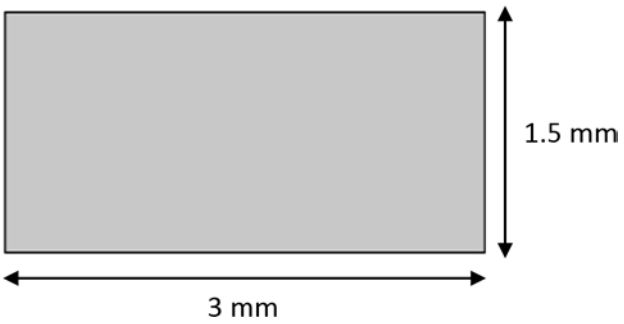

FIG. 3.39. CTE test sample in COMSOL

After the Finite Element Analysis is done on the sample, which expands due to the increase in heat, the effective longitudinal CTE can be derived using the following formula

$$\alpha_{22} = \frac{1}{h}\frac{dh}{dT} \tag{3.10}$$

where h is the original height, dh is the change in height, and dT is the change in temperature. Since we know that the change in temperature is just 1^{o}C, we can simplify Equation (3.10) to

$$\alpha_{22} = dh/h \ (1/^{o}\text{C}) \tag{3.11}$$

For both the IRD and the RSC, the same sets of fiber interaction and slowness parameters were investigated for the effective longitudinal CTE and the results for α_{22} are presented in Table 3.2. The FEA solution was found using a rectangular element mesh with 70 elements in the x_1-direction and 10 elements in the x_2-direction.

Table 3.2. Effective longitudinal CTE, α_{22}

Model Used	α_{22} (1/°C)
IRD - $C_I = 0.001$	9.61 x 10^{-6}
IRD - $C_I = 0.01$	2.00 x 10^{-5}
RSC - $C_I = 0.01$, $\kappa = 1/5$	3.79 x 10^{-5}
RSC – $C_I = 0.01$, $\kappa = 1/10$	4.69 x 10^{-5}
RSC - $C_I = 0.01$, $\kappa = 1/30$	5.93 x 10^{-5}

CHAPTER FOUR

Experimental Methods

The experimental phase of this study involved completing an in-house large scale bead deposition system. This was done by designing and fabricating a new translational platform for fabricating beads of carbon fiber filled ABS from which test samples were cut for tensile testing and for testing in a thermomechanical analyzer (TMA) machine. After the large scale bead deposition system had been completed, a comprehensive parameter study was performed to identify appropriate ranges of manufacturing conditions prior to fabricating the samples used within this chapter. From the final fabricated samples, structural testing was performed to obtain the effective bulk longitudinal modulus and thermomechanical testing was performed to obtain the effective bulk longitudinal coefficient of thermal expansion. Both sets of results are compared to those from the modeling efforts from the previous chapter, and closest resemble those of the RSC model with an interaction coefficient of $C_I = 0.01$ and slowness parameter of $\kappa = 1/30$.

4.1 Building the 3D Printer Bed

The construction of the large scale bead deposition system at Baylor University was begun by Nathan Spinnie during his master's studies [22]. Spinnie used an Exon8 Single Screw Extruder from HapCO Inc. and constructed the supporting frame, onto which this extruder was mounted. He then built a small 18 in. x 18 in. translation platform that could move in both the x_1 and x_2 directions [22]. At the beginning of the

present thesis efforts, a Strangpresse Extruder Model 19 was obtained and mounted onto the support structure replacing the Exon8 originally used by Spinnie. As part of the current research efforts, the author worked with Daniel Pulipati, a Baylor doctoral candidate, and Dr. Douglas Smith to setup the extruder, shown in FIG. 4.1, and make it operational.

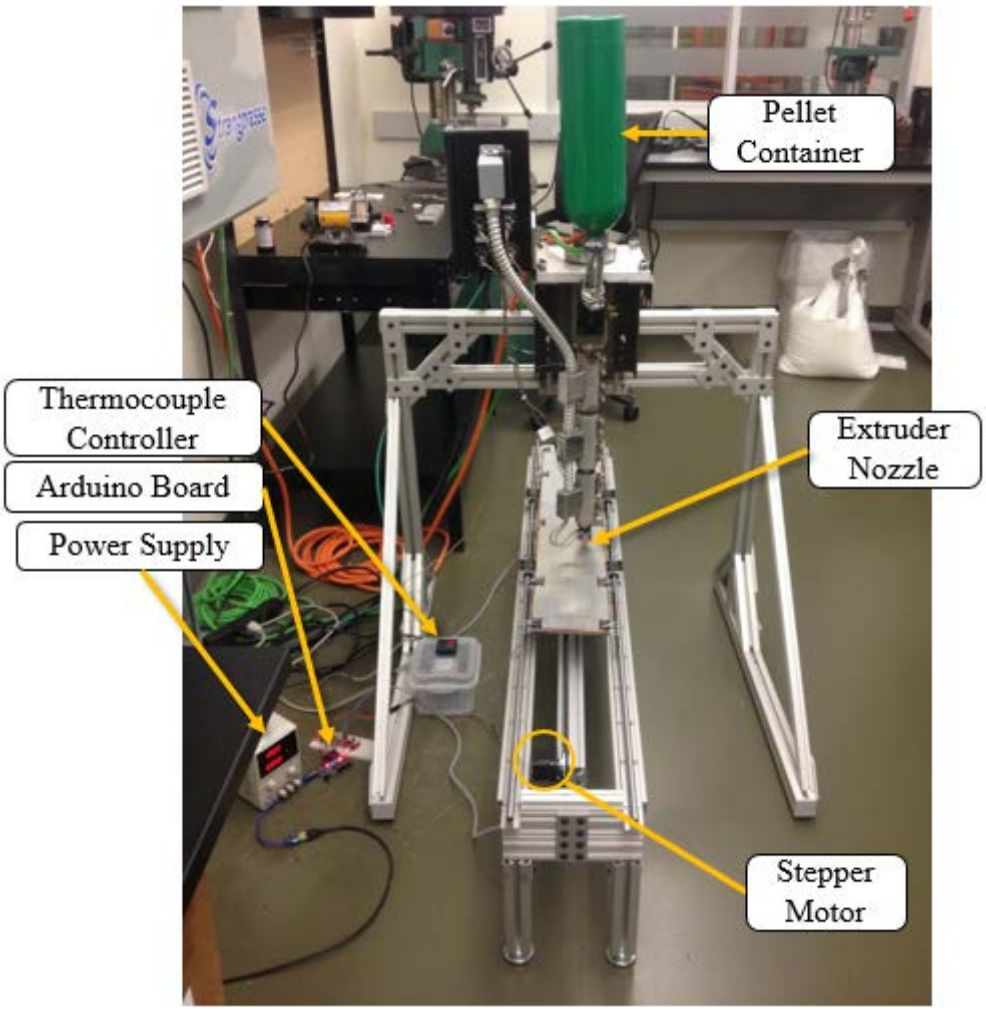

FIG. 4.1. Large scale bead deposition system at Baylor University

Another update to the large scale bead deposition system as part of this research effort was the design, construction, and implementation of a new high-speed print bed system. The fabricated print bed can only move in the x_1 direction, but is much longer

than Spinnie's (36 in. as opposed to 18 in.). This enabled longer beads for tensile test samples and also decreased any spatial inhomogeneity inherent to the start-up and termination regions of a print path. The addition of a second and potentially a third axis is left for a future study, and the focus of the present scope of work was on the tensile and thermal properties of an individual print path. The entire Baylor University large scale bead deposition system that was used for this study is shown in FIG. 4.1.

In order to build the translating print bed system, there were several items that needed to be addressed. The system needed a print bed, a large and flat heater to heat the print bed, a supporting structure for the print bed, and a method of controlling the movement of the print bed. The print bed itself is 6 in. wide and 36 in. long, and is composed of several layers. The print bed base layer is a piece of carbon fiber composite that is 21 ½ in. long to provide rigidity as well as insulation. The laminated plate was screwed to linear bearings that slide back and forth on the polished steel, linear rails of the translation system, allowing the print bed to slide back and forth securely on the rails. The rough dimensions of the print bed base layer are shown in FIG. 4.2.

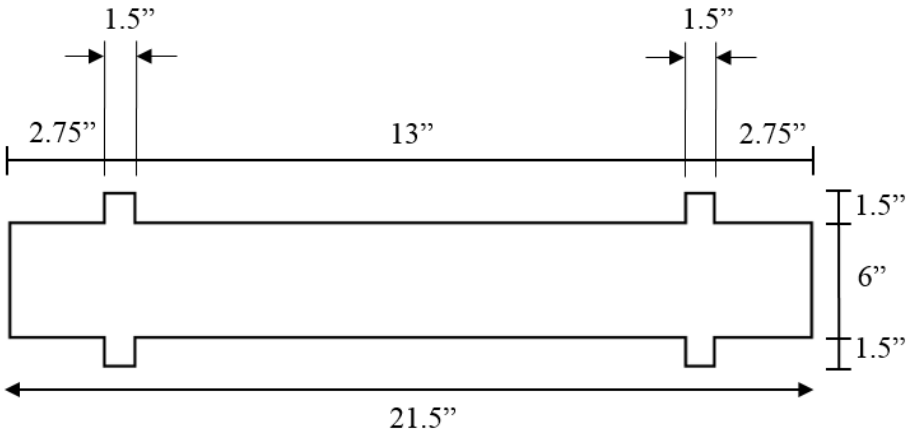

FIG. 4.2. Dimensions of the print bed base layer (not to scale)

The small peninsular areas of the carbon fiber sheet indicate the mounts where the carbon fiber sheet was screwed to the linear bearings.

A rubber timing belt was attached to the underside of this composite piece with 3D printed, plastic clips that were screwed to the composite (see FIG. 4.3). On either end of the supporting structure are a set of matched stepper motors that rotate the timing belt in tandem. These matched motors provide twice the torque of a single motor, and allow the print bed to translate back and forth along the linear rails during processing.

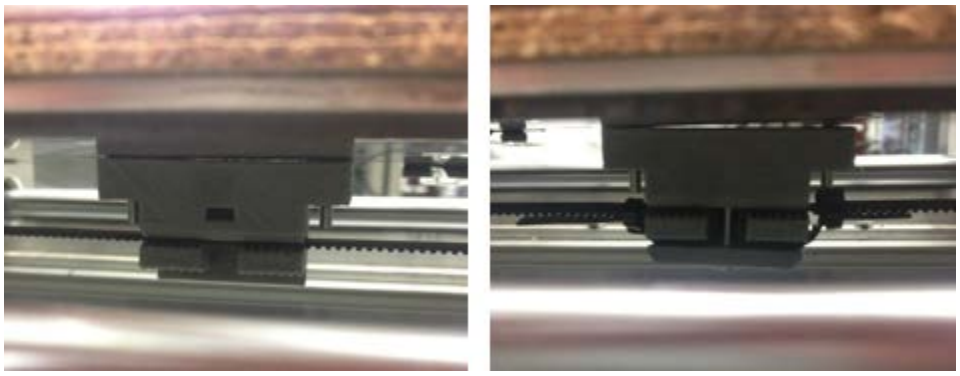

FIG. 4.3. 3D printed timing belt clips

The second layer of the print bed from the bottom is a piece of 6061 aluminum 6 in. wide and 36 in. long ordered from mcmaster.com. This piece is identical to that of the top layer of the print bed which serves as the printing surface. This aluminum piece on the underside, which added weight to the print bed, was used to increase the bending stiffness and aid in mitigating leveling issues with the print bed.

On top of the lower aluminum plate was placed two layers of 1/16 in. thick cork board, followed by a thermal heating blanket, and finally the top aluminum plate. The cork board was cut to 6 in. x 36 in. and insulated the heat bed from the underside, forcing the heat from the thermal blanket to dissipate through the upper aluminum plate. The

electrically resistive thermal blanket is a flexible silicone-rubber heat sheet from mcmaster.com that was 6 in. x 36 in. The temperature of this heat bed was controlled by a Versatile Control & Technologies JLD612 temperature controller coupled with in-house welded thermocouples. This controller allowed one to set the temperature of the heat bed and displayed this temperature along with the actual temperature of the heat bed, determined by a thermocouple that was placed between the heat bed and the top aluminum plate. The top aluminum plate had the same specifications as the one near the bottom. To keep all of the layers of the print bed sandwiched together, metal clips were used. An image of the complete stack of the print bed can be seen in FIG. 4.4.

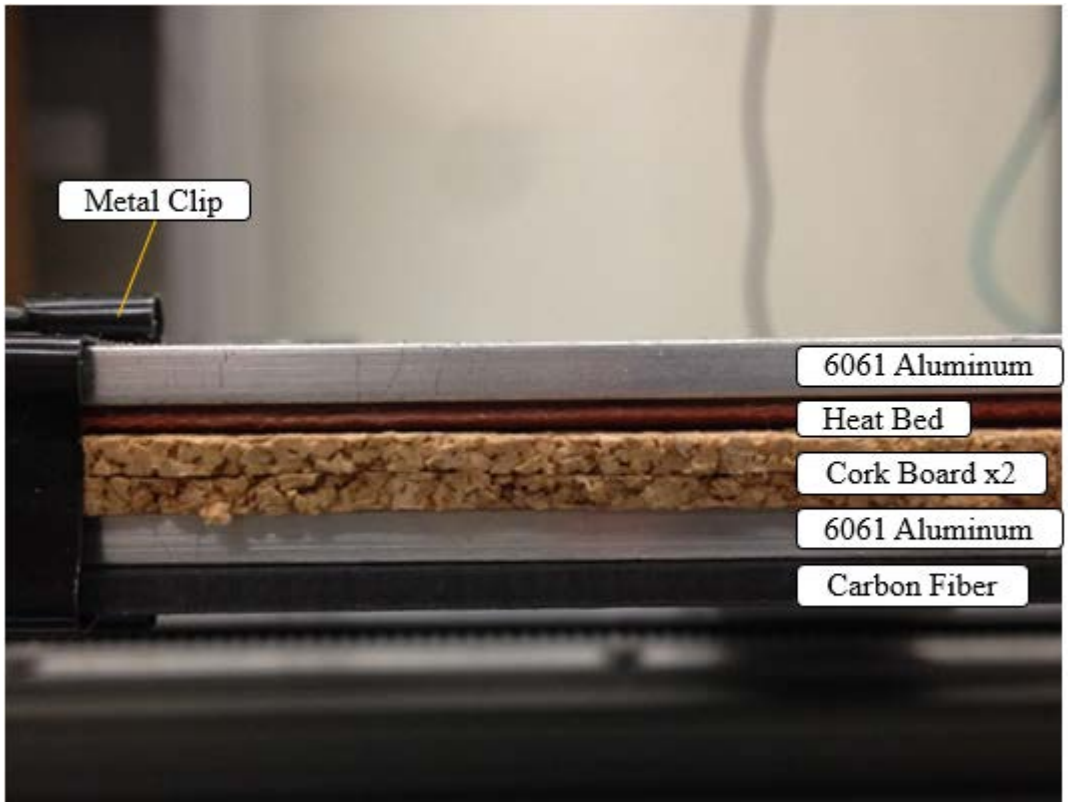

FIG. 4.4. Print bed layers

One of the problems encountered when building the translation system was that the linear rails, on which the print bed traveled, were slightly bowed upon delivery. In order to combat this issue, the rails were tightly fastened to straight pieces of 80/20 aluminum and the bowing was somewhat mitigated.

The supporting structure for the print bed was also made of 80/20 aluminum. It has four supporting legs, is a total of 60 in. in length, just under 10 in. wide, and nearly 15 in. tall, to the top of the rails on which the bed travels (including the extra height added by the feet). The height of the whole translation system, from the floor to the top of the print bed is just over 15 in. tall. The feet of the translation system are vibration-damping leveling mounts from mcmaster.com. These mounts provided fine controls to level the bed relative to the extruder. The addition of the vibration-damping mounts also conveniently softened internal vibrations from translation stage and the stepper motors. A closer view of the print bed support structure is shown in FIG. 4.5.

The motion of the print bed was controlled by two Nema 17 Bipolar stepper motors fastened on either end of the support structure, underneath the print bed, on a piece of 80/20 aluminum that spanned the length of the structure. These stepper motors were controlled by an Arduino UNO R3 board through a custom in-house program written in C on a PC. A variable voltage power supply capable of providing 60 Watts is used to power the stepper motors, and a second power supply capable of providing over 90 Watts of power was needed for the thermal blanket. The temperature control and the stepper motor control were two separate systems, with the Arduino controlling the positioning of the table and the Versatile Control & Technologies temperature controller managing the temperature of the printing bed. The Arduino program enabled the stepper

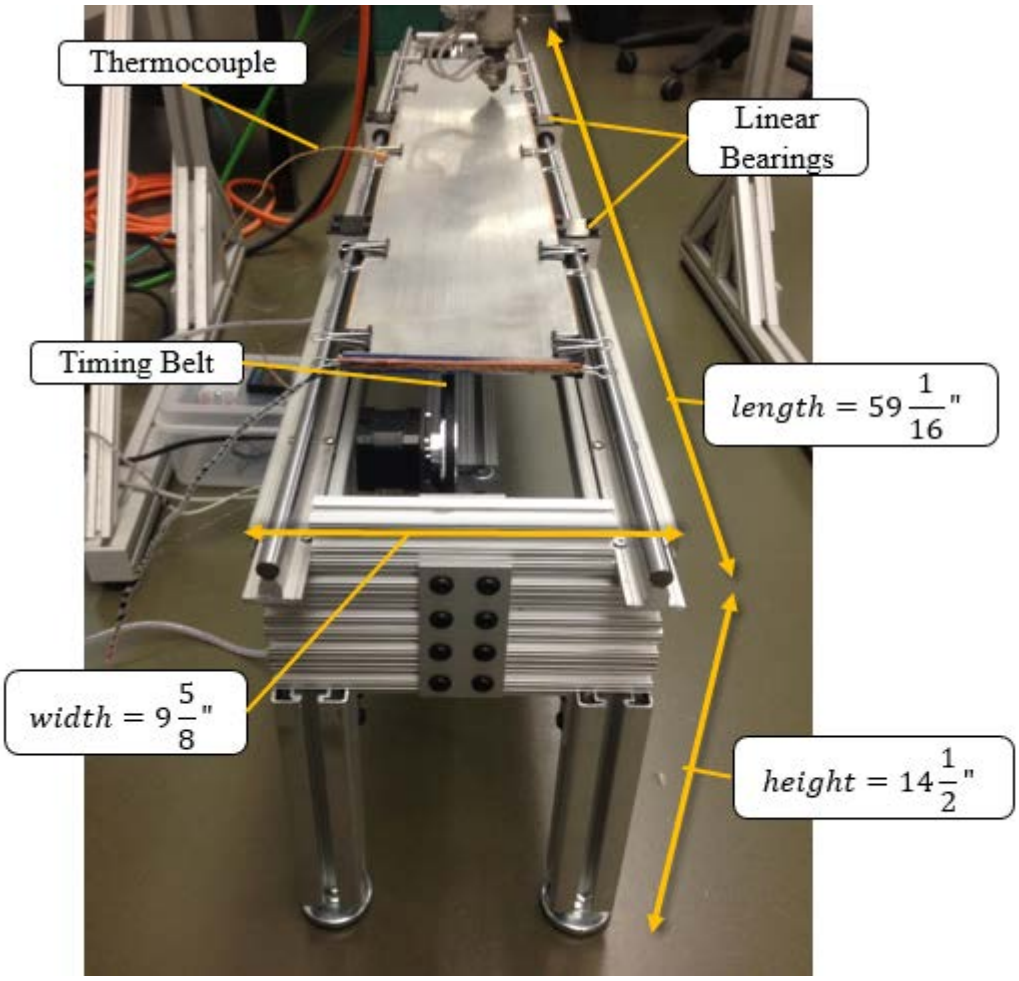

FIG. 4.5. Print bed and print bed supporting structure

motors to run up to 70 mm/s although, for the presented results all samples were fabricated at just 50 mm/s (≈ 2 in/s) so as not to exceed the extruder's capacity to extrude the carbon fiber reinforced ABS polymer.

4.2 Flatness of the Table

The height difference across the top of the print bed was measured using a dial gauge by magnetically attaching the dial gauge to the extruder assembly with the point on the top of the print bed at one end. Then the print bed was translated and a video recording made of the dial gauge as it read the change in height of the moving print bed

from end to end. After many adjustments had been made to the bed, mounting frame, and clamping system, a maximum height difference of 0.33 mm across the middle 16 in. of the bed was found. The extra 10 in. on both ends of the bed added even more to the height discrepancy, so when collecting samples, the ends of the beads were trimmed away and only 16 in. of each bead, from the middle 16 in. of the print bed, were used when collecting samples. This ensured that the test samples were collected from the most uniform and pristine section of the beads. It should also be noted that the minimum and maximum bead thickness measurements were 2.16 mm and 2.40 mm, respectively, which gives a difference of only 0.24 mm (as opposed to 0.33 mm). In addition, the maximum thickness difference for any one bead in particular was only 0.1 mm.

4.3 Material and Parameters

The material that was used was in this study is a composite of acrylonitrile butadiene styrene (ABS) and carbon fiber compounded by PolyOne. The carbon fiber weight percentage provided in the specification sheet is 13%. According to the technical data sheet for this material, the tensile modulus and strength are 7720 MPa and 78.6 MPa, respectively. The material was received in pellet form and dried at 60^{o}C for 11 hours in a Blue M Laboratory Oven, Model LO-225-P.

Beads of the material were printed using the in-house Strangpresse Extruder Model 19 in conjunction with the custom translating print bed. The pellets were fed into the container at the top of the extruder assembly (see FIG. 4.1) and the extruder was run at the full 2250 revolutions per minute (RPM). The parameters used for the extruder included temperatures of 198°C, 204°C, and 210°C along the three sections of the extruder (which were not seen to vary by more than a few degrees). The screen where the

settings for the extruder could be set is shown in FIG. 4.6. The software used by the extruder is Allen Bradley FactoryTalk [82].

FIG. 4.6. Strangpresse Extruder Model 19 settings

The heated print bed was set to 65°C and was not observed to deviate by more than 2-3°C during the course of making the samples used for the analysis presented in this thesis. Since the thermocouple controller was next to the translation system, it was easy to watch any changes in temperature as the print bed moved and the extruder printed a bead. As for the nozzle height (the distance of the gap between the tip of the nozzle and the print bed), this was measured using a feeler gauge to be roughly 1.5 mm. All beads were fabricated at the same nozzle height after the frame was set in place. The nozzle height of 1.5 mm was chosen based on the results from a preliminary study. In that study it was observed that the beads fabricated with a nozzle height of 1.5 mm at 2250 RPM produced a relatively smooth bead with a relatively constant cross-sectional area. The table speed was set to 50 mm/s (≈1.97 in/s). Once the extruder was turned on, the

Arduino controller to move the translation bed was run. Pictures of the fabrication process partway through a printing can be seen in FIG. 4.7(a) and FIG. 4.7(b). The blue painter's tape is placed on top of the print bed to allow the polymer melt to better adhere to the surface.

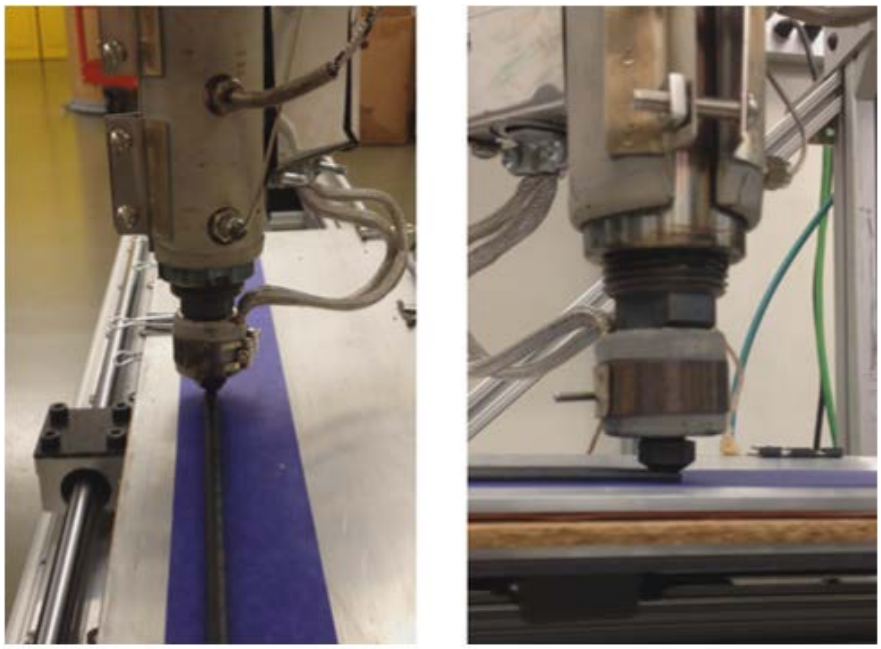

(a) (b)

FIG. 4.7. Fabrication process; (a) back view and (b) side view

4.4 Sample Preparation

The next step in the experimentation process was to cut smaller samples out of the acceptable 16 in. region of the printed beads for tensile and CTE testing. After printing, the beads look like those shown in FIG. 4.8. Since the print bed was 36 in. long, most of the beads were near 36 in. long as well, although oftentimes a bead would not adhere to the bed at the start of a print job and result in a bead shorter than 36 in.

The top of the beads oftentimes had small ripples caused by the extruder dragging through the deposited material. This can be seen in the bead on the left in FIG. 4.8(a). If

the extruder had been extruding at a slower rate or if the print bed had been moving faster, the ripples would be less prominent. The drawback of the slower rate is the risk of insufficient material to deposit on the print bed and the polymer being pulled along the table by the extruder, causing the cross sectional width to vary as a function of position. The bottom of the beads were smooth since they were laid on the smooth print bed as can be seen in the bead on the right in FIG. 4.8(a).

FIG. 4.8. Sample preparation; (a) fabricated beads, (b) tensile samples, and (c) TMA samples

After the beads were fabricated, they were cut into test samples according to the layout in FIG. 4.9. Typical tensile samples are shown in FIG. 4.8(b) cut to a length of approximately 5 in., and the smaller TMA samples cut approximately 3 mm in length are shown in FIG. 4.8(c). It was important to cut the TMA samples with very clean, parallel

cuts so as not to distort the testing results for the effective longitudinal CTE α_{22}. The low speed saw for the sectioning of the CTE samples is a Buehler IsoMet^{TM} Low Speed saw as pictured in FIG. 4.10. A speed setting of 7- 8 on the saw's dial gage was used to cut all of the samples. Wire cutters were used to cut the ends of the 16 in. bead section since extreme precision and clean cuts are not required for the tensile test specimens as the ends of the sample are placed within the grips of the tensile stage during testing.

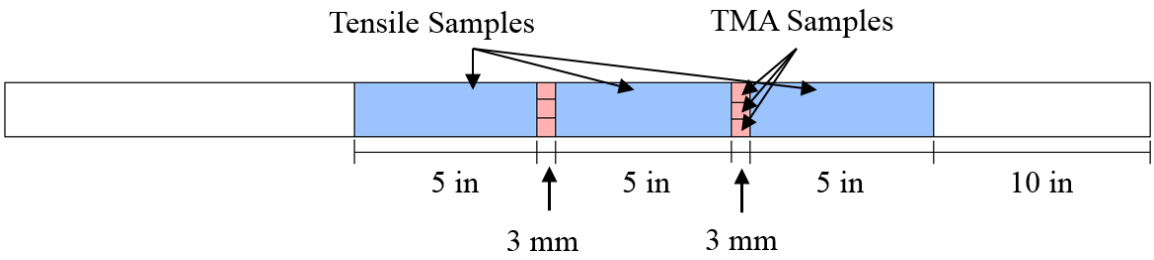

FIG. 4.9. Layout of how samples were cut from a bead (not to scale)

FIG. 4.10. Low speed saw used to cut samples

A typical bead, and therefore a typical tensile sample too, was 10-11 mm wide and 2.2-2.4 mm thick. The tensile samples were cut to 5 inches. A typical TMA sample was 2-3 mm long in the longitudinal direction (i.e., the direction the bead was printed). For keeping track of the tensile samples, a silver Sharpie was used to label the beads and tensile samples (this can be seen in FIG. 4.8). The TMA samples were too small to label with a marker, but were placed within a labeled bag.

4.5 Tensile Testing

After preparing the samples, 33 tensile test were done using a Test Resources 100 Series Electromechanical Universal Test Machine with a 1 kip (1000 lbf) load frame as shown in FIG. 4.11. Notice a tensile sample is currently mounted between the grips and the extensometer is mounted in the region between the grips.

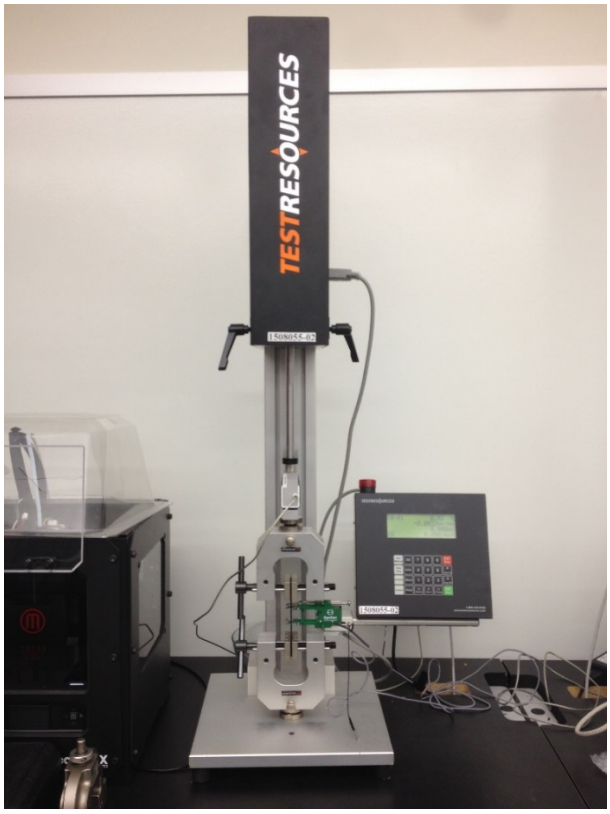

FIG. 4.11. Test resources tensile tester

To test a sample, the following general procedure is followed. The geometry of the sample is measured carefully using micrometers and the dimensions are entered into the control software. Two measurements of the width are taken on either end of a sample as shown in FIG. 4.12 and the average entered into the computer. Although the width measurement on one end of a sample was never actually the same as the width measurement on the other end of the sample, the largest discrepancy in width measurements for a single sample was only 0.58 mm, the smallest discrepancy was only 0.02 mm, and the mean discrepancy was 0.21 mm.

FIG. 4.12. Typical width measurement of tensile sample

In a similar way, the thickness of each tensile sample was measured on either end as shown in FIG. 4.13 and the average taken. The maximum discrepancy in thickness measurements on either end of a sample was only 0.10 mm, the minimum discrepancy was 0 mm, and the average discrepancy was 0.04 mm.

FIG. 4.13. Typical thickness measurement of tensile sample

After the geometrical measurements are entered into the software, the tensile sample is inserted vertically within the grips and the grips are tightened. Then an Epsilon Axial Extensometer, Model 3542-025M-025-ST is mounted to the tensile sample and the pin ensuring a zero strain is removed from it. At this point the strain and the load are zeroed out. The complete setup with the sample, grips, and extensometer is shown in FIG. 4.14.

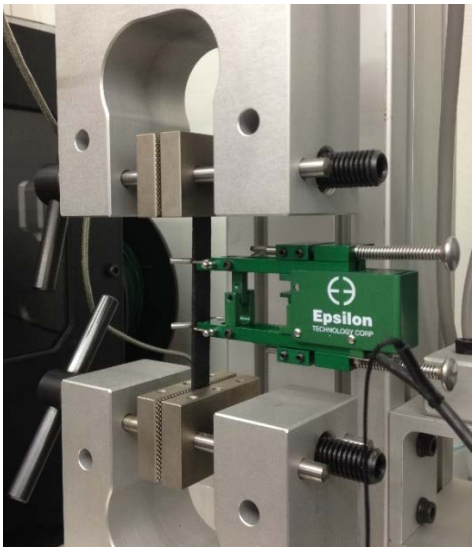

FIG. 4.14. Epsilon extensometer attached to tensile sample

After the strain gauge is attached to the sample, the user enters “Start” on the Test Resources machine to initiate the test. Each test was run with a control rate of 5 mm/min. The first tensile sample broke during the test under a maximum load of 767.3 N. Thus, the remaining tests were manually stopped when the load reached around 600-625 N so that the samples would not break and would be available for further testing. After the test was stopped, the extensometer was detached, the Test Resources machine was manually jogged to unload the force on the sample, and the sample was removed. In all, 33 tensile samples were tested. The data from each test included many data points for the value of the longitudinal load (N) and the corresponding longitudinal strain (mm/mm) at those loads, where the term “longitudinal” refers to the x_2, or “vertical,” direction. A typical response curve of the force as a function of the strain is provided in FIG. 4.15 for sample 33.

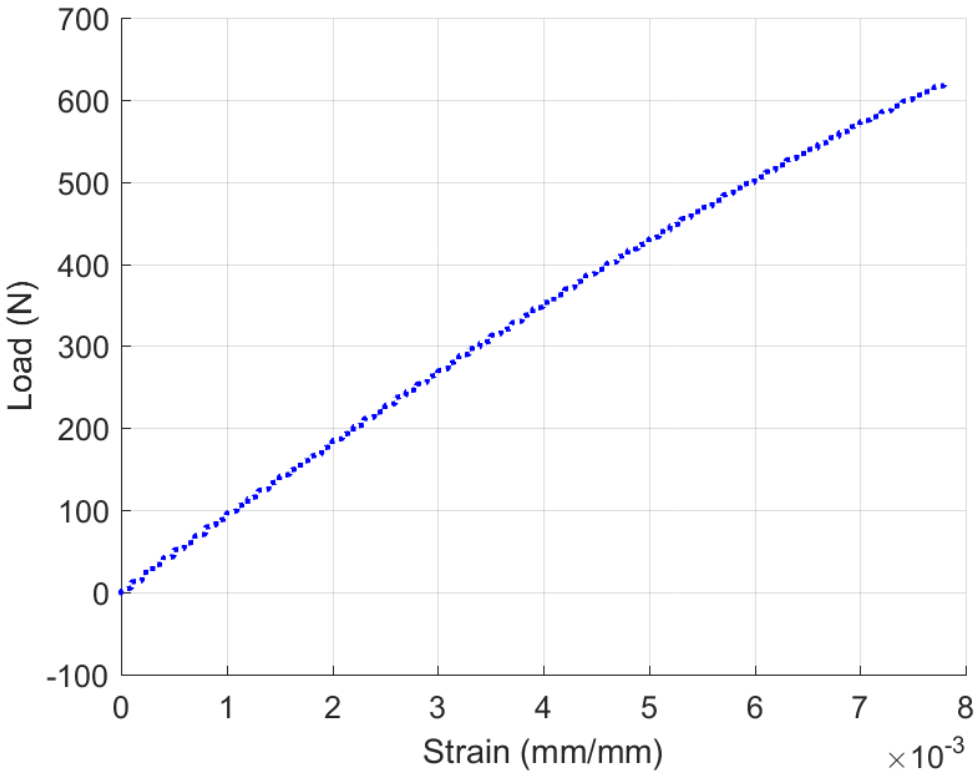

FIG. 4.15. Typical response curve of load as function of strain (sample 33)

From load data for the above representative tensile test, the longitudinal stress is calculated at the same data points with the equation

$$\sigma_{22} = \frac{F_2}{A} \tag{4.1}$$

where σ_{22} and F_2 are the stress and load (or "force") in the longitudinal direction, respectively, and A is the initial cross-sectional area of the tensile sample calculated using the average width and thickness measurements of the sample. Once the stress is obtained from the force, stress-strain graphs of the data can be made. The stress-strain data is shown in FIG. 4.16, which was produced by an in-house MATLAB code that reads in the data produced by the Test Resources software. Since it appears that the linear elastic region of this curve ends around 10 to 15 MPa, an in-house MATLAB code is used to cut out the data points above 10 MPa and fit a line to the remaining data points using linear regression. In this way, the slope of this line, which is graphed in FIG. 4.16 can be found and it gives the effective longitudinal Young's Modulus E_{22} of the tensile sample according to Equation (3.8). E_{22} for this particular sample was found to be 3.80 GPa and the coefficient of determination for the linear fit was $r^2 = 0.9991$. Since a linear fit is more accurate as r^2 gets closer to 1, this shows that the line fits and represents the actual data extremely well.

The stress-strain data from all 33 tensile tests, collected from 11 beads, are graphed in FIG. 4.17. The elastic regions for most of the stress-strain curves in FIG. 4.17 appear to end when the stress is around 10 to 15 MPa. Thus, the in-house MATLAB code is used to cut out the data points above 10 MPa and to fit lines through the remaining data points using linear regression for each curve. The lines fit to the *elastic* regions of each stress-strain curve are shown in FIG. 4.17 overlaying the original stress-strain data. When

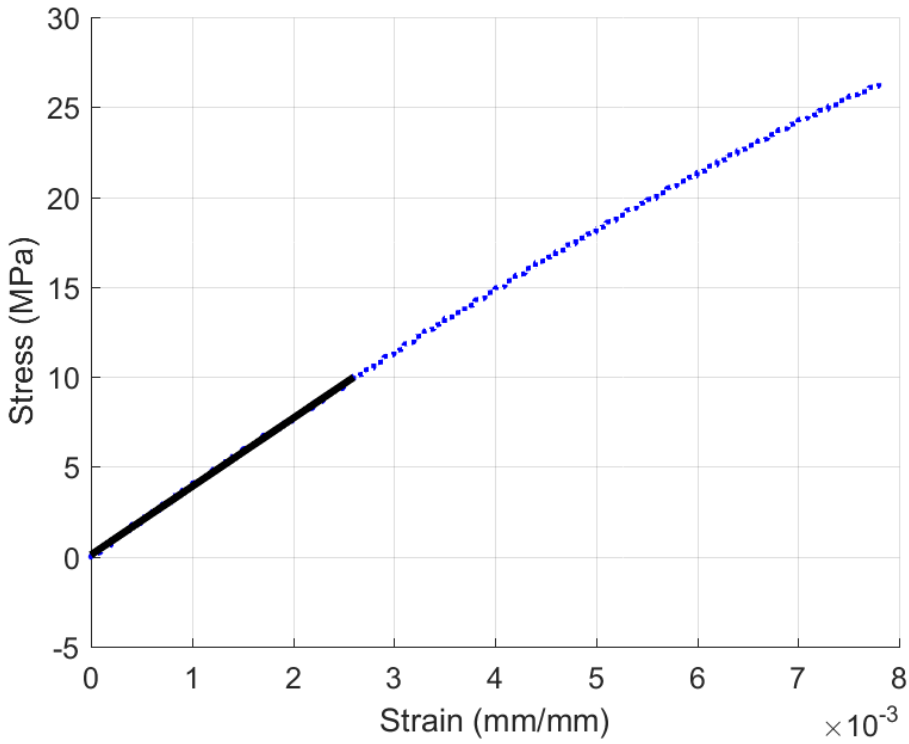

FIG. 4.16. Stress-strain curve from a typical tensile test (sample 33): original data (blue dots) and linear fit (black line)

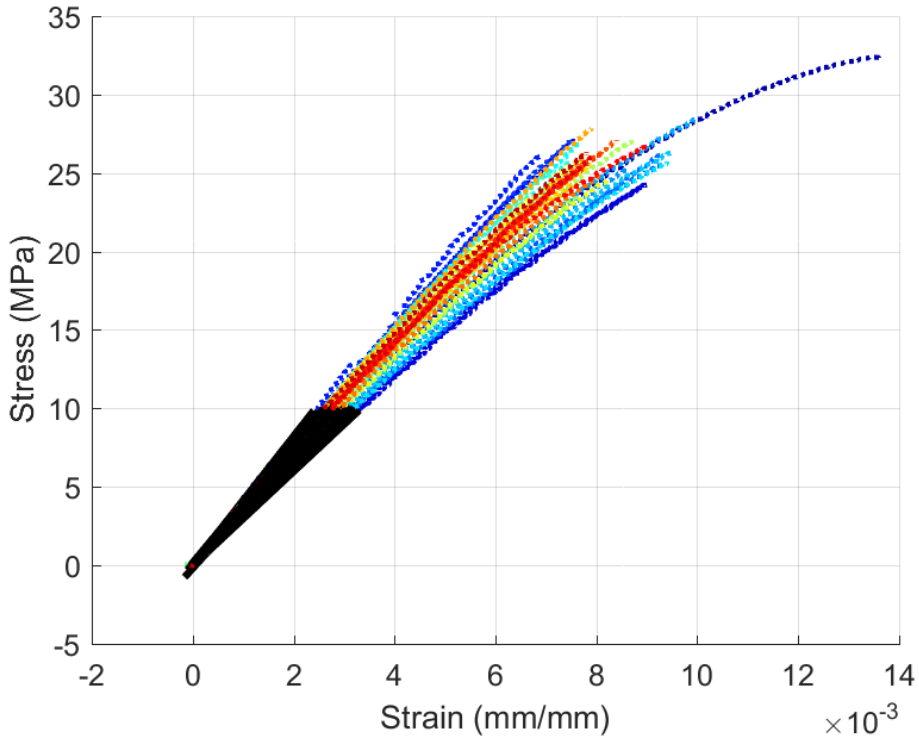

FIG. 4.17. Stress-strain data (colored dots) and linear fits (black lines) for 33 tensile tests

rounded to 4 decimal places, the coefficient of determination (r^2) is at least 0.9990 for *each* of these linearly fit lines.

To reiterate, the slope from each of the line segments in FIG. 4.17 gives the effective longitudinal Young's Modulus for each tensile sample according to Equation (3.8). After calculating the slope of each of these lines using the in-house MATLAB code, the values were averaged to give a mean effective longitudinal Young's Modulus $\overline{E_{22}}$ of a 3D printed, 13% carbon fiber filled ABS composite bead, fabricated by FFF, of 3.55 GPa. Other statistics for these tests include the maximum and minimum values of the effective longitudinal Young's modulus E_{22} which were 4.09 GPa and 3.01 GPa, respectively, and the standard deviation σ which was 0.27 GPa. The coefficient of variation of E_{22}, was found to be

$$CV = \frac{\sigma}{\overline{E_{22}}} \cdot 100\% \approx \frac{0.27\ GPa}{3.55\ GPa} \cdot 100\% \approx 7.47\% \tag{4.2}$$

These results compare well with the values given in Table 3.1 from the modeling aspect of this thesis, but a discussion of the comparison between the experimental characterization and the model predictions will be deferred to Section 4.7. It is also worth noting that the theoretical maximum value of E_{22}, which will occur for perfect fiber alignment in the x_2 direction, is 5.69 GPa.

4.6 TMA Testing

In order to measure the longitudinal, linear CTE α_{22} of a 13% carbon fiber filled, 3D printed, bead made by FFF, thermomechanical analyzer (TMA) tests were also done. These tests were done with a TA Instruments TMA Q400, pictured in FIG. 4.18 on samples prepared following the procedure discussed in Section 4.4.

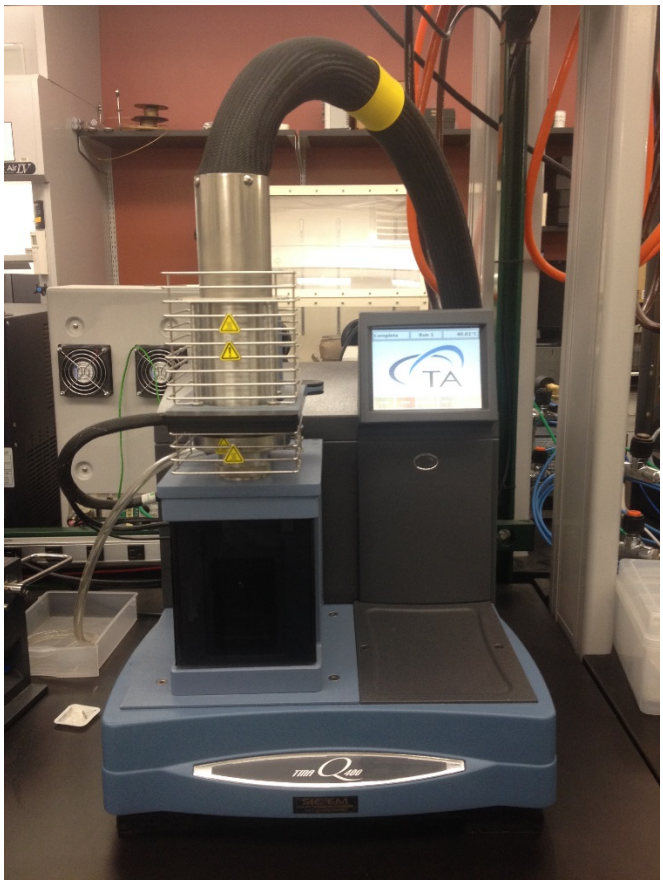

FIG. 4.18. TA Instruments TMA Q400

In order to perform the test for the CTE, a TMA sample would be carefully inserted into the TMA with tweezers between a quartz probe and a quartz plate. The sample set up is depicted in FIG. 4.19.

The sample would be placed so that the longitudinal dimension of the bead was upright. After this the length of the longitudinal dimension of the sample would be measured by the quartz probe through a linear encoder within the TMA and recorded in the computer linked to the TMA *prior* to the experiment. With the known length and the fact that the CTE of quartz is known, the TMA is able to measure the change in length in the longitudinal direction of the TMA sample *during* the course of the experiment while

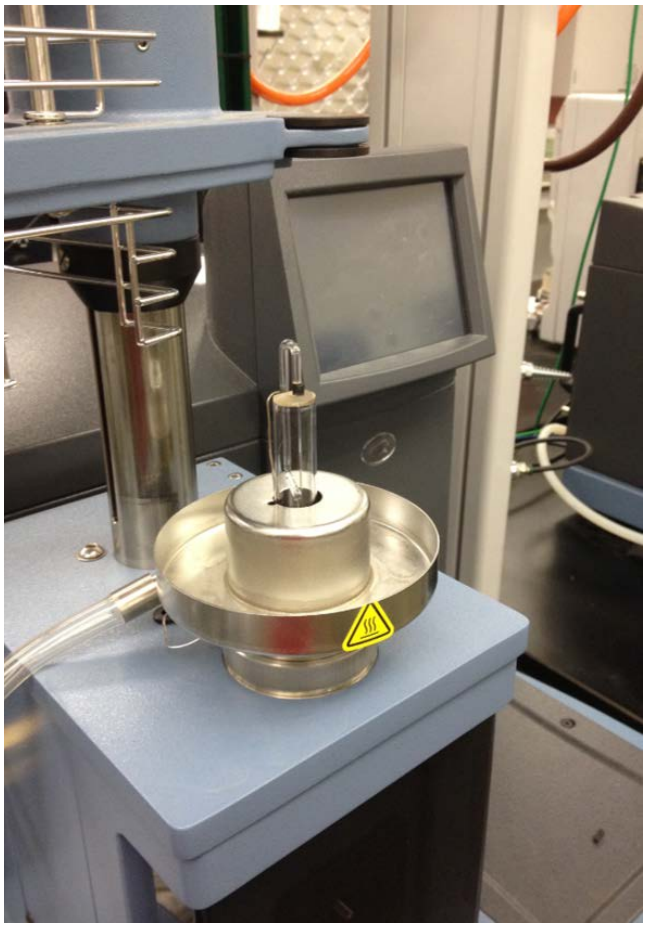

FIG. 4.19. TMA sample setup

the temperature inside the TMA changed. The displacement resolution for the TA Instruments Q400 TMA is under 0.5 nm. Following the recommendations from TA Instruments, a force of 0.20 N is placed on the sample by the quartz probe throughout testing. The sample is cooled to -40 ^{o}C and held for 2 minutes, at which point the length of the sample is measured and then the temperature is slowly ramped at a rate of 3^{o}C/min up to 110^{o}C. Each temperature ramp test required about an hour and although there was more variability in the results compared to the Young's modulus results given in the section 4.5, an example is provided in FIG. 4.21 for sample 2. The curve initially has a roughly linear-like profile, but drifts negative shortly afterward. It would be tempting to

think that the CTE above 50°C was negative, but this is due to the softening of the polymer at the higher temperatures. For calculating α_{22}, all data above 25 °C is neglected in the present study so that we are only dealing with the linearly elastic region.

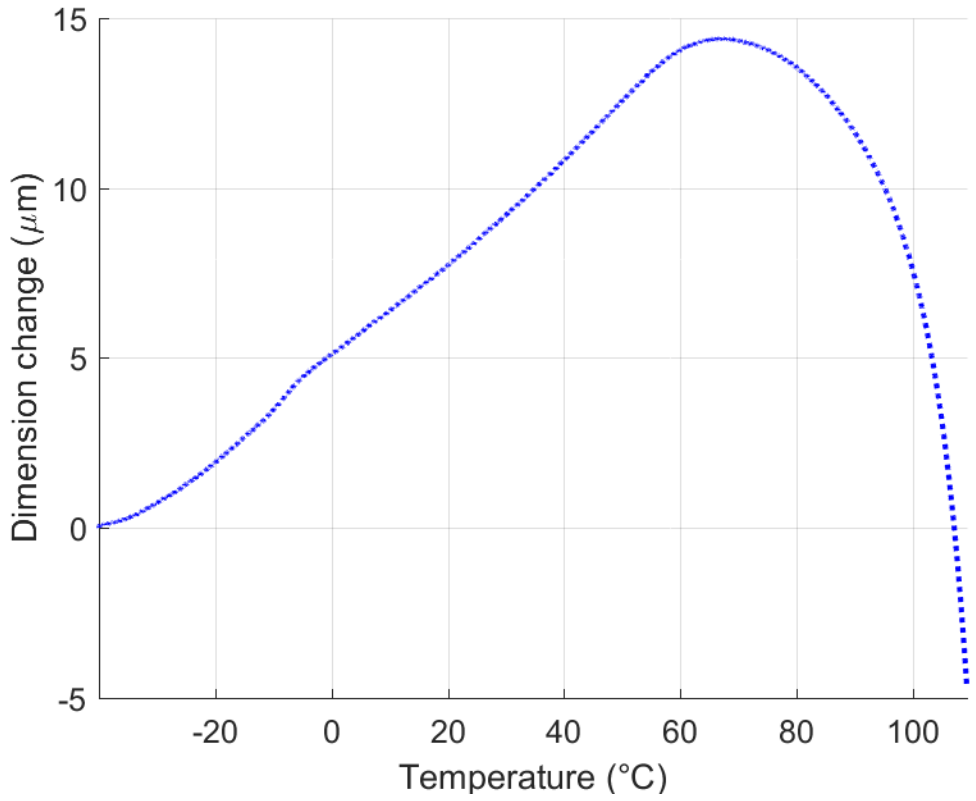

FIG. 4.20. Typical TMA test data (sample 2)

In order to get α_{22} prior to the softening point,the results for temperatures up to 25°C are used in the subsequent analysis. By dividing the dimension change data shown in FIG. 4.20 by the original length of the sample, which in this case was sample 2, the longitudinal strain ε_{22} could be calculated and plotted with MATLAB as a function of temperature as in FIG. 4.21. A custom MATLAB code was used to fit a line through the data using linear regression and plot the data overlaid with the linear fit. Doing this yielded the line segment shown in FIG. 4.21 superimposed on the original data in blue.

The r^2 value of the linear fit to this particular set of data is 0.9949. The CTE can be calculated using Equation (3.10) as the slope of the line segment in FIG. 4.21. For the representative sample whose data is shown in FIG. 4.21, the effective longitudinal CTE α_{22} was found to be approximately 4.74 x 10^{-5} (1/ºC).

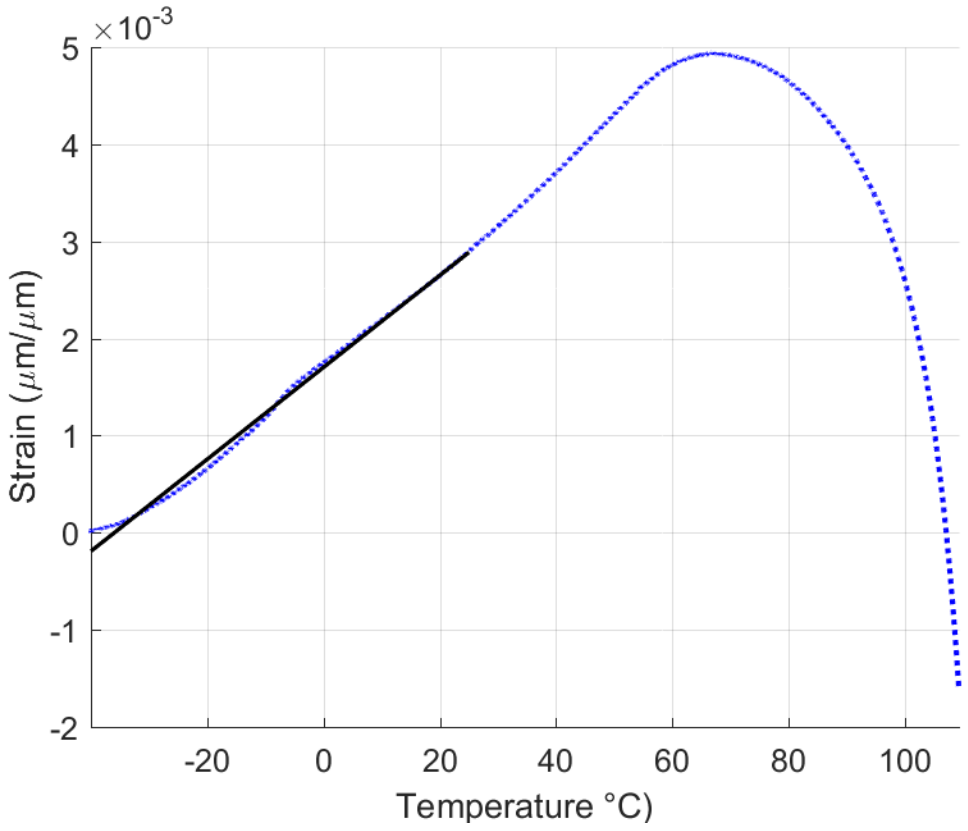

FIG. 4.21. TMA test; original data (blue dots) and linear fit to data (black line)

The test results of six TMA samples, that were prepared for CTE testing as in the above procedure, are given in this thesis. The strain-temperature data for each of these is shown in FIG. 4.22 along with linear fits to the data points up to a temperature of 25ºC. The minimum r^2 value for the linear fits shown in FIG. 4.22 is 0.9859. The maximum and minimum values for α_{22} are 7.01 x 10^{-5} (1/ºC) and 4.46 x 10^{-5} (1/ºC), respectively, and the mean and standard deviation of α_{22} are approximately 5.43 x 10^{-5} (1/ºC) and 1.12

x 10^{-5} (1/ºC), respectively. Dividing the standard deviation by the mean and multiplying by 100% gives a coefficient of variation of 20.65 % for α_{22}. The results of only six TMA tests are reported in this thesis due to the hour long wait for each test.

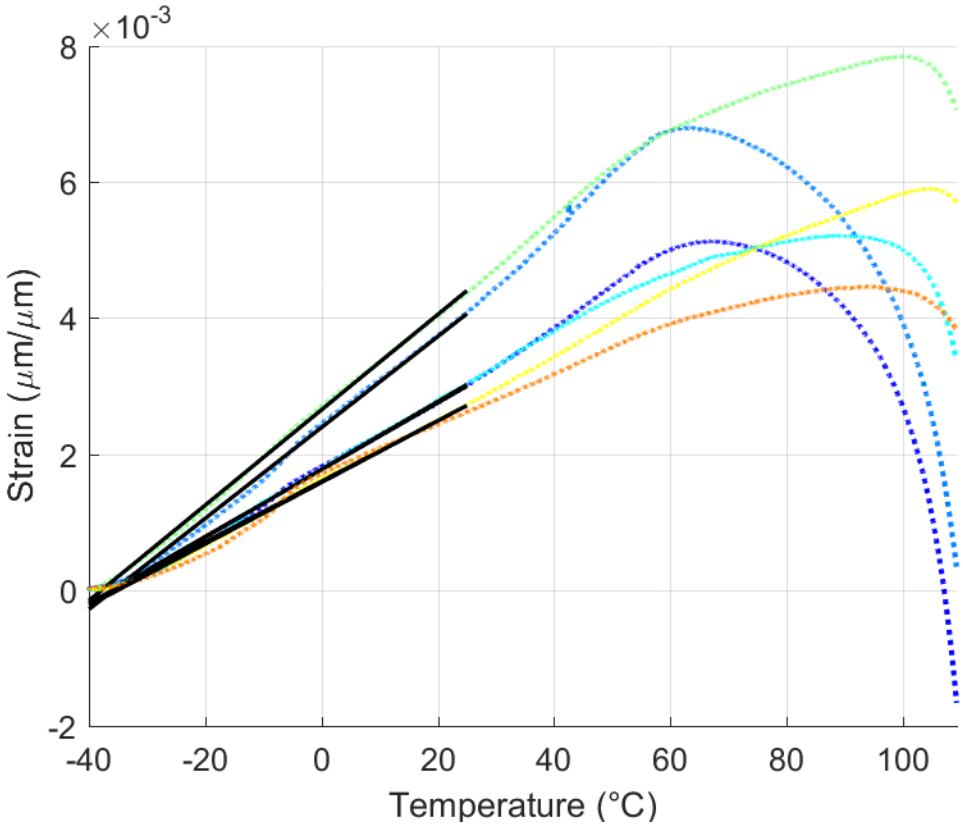

FIG. 4.22. CTE data (colored dots) with linear fits (black lines)

Several factors could have affected the seemingly wide variability in CTE values. One of the major factors could potentially involve human error in preparing the samples. In addition, another source of error could potentially be the fact that the TMA samples were collected from different parts of a bead as shown in FIG. 4.9, since the fiber orientation state could have been slightly different in the samples taken from the sides of a bead as opposed to the center of a bead.

4.7 Comparison of Test and Model Results

The last point addressed in this chapter is the validity of the computational methods used in Chapter Three to predict the experimental results of this chapter. In Chapter Three, four values of the effective longitudinal Young's Modulus were calculated using two different fiber orientation kinematics models with varying levels of fiber interaction and orientation kinematics slowness. Recall, in the above study the Young's modulus was found to be 3.55 GPa (the mean) with a standard deviation of 0.27 GPa from the 33 different test specimens. To quantify the computational results of Chapter Three, an absolute percent relative error is computed as

$$\varepsilon = \left| \frac{(model\ E_{22}) - (experimental\ E_{22})}{(experimental\ E_{22})} \right| \cdot 100\% \tag{4.3}$$

where ε is the absolute percent relative error, $(model\ E_{22})$ is the value of the effective bulk longitudinal modulus calculated by a given model (from Equation (3.8)), and $(experimental\ E_{22})$ is the average value of the effective longitudinal modulus that was measured in this chapter, 3.55 GPa.

Table 4.1. Effective longitudinal Young's modulus, E_{22} – Error

Model Used	E_{22} (GPa)	ε
IRD - $C_I = 0.001$	4.84	36.46 %
IRD - $C_I = 0.01$	4.43	24.82 %
RSC – $C_I = 0.01$, $\kappa = 1/5$	3.90	9.90 %
RSC – $C_I = 0.01$, $\kappa = 1/10$	3.68	3.62 %
RSC – $C_I = 0.01$, $\kappa = 1/30$	3.37	5.10 %

Table 4.1 shows that for obtaining the effective longitudinal Young's Modulus, the most unreasonable of the fiber interaction models, according to the experimental results of this study, appears to be the IRD model with an interaction coefficient of 0.001.

Actually, neither of the IRD models produce results for E_{22} between the minimum and maximum experimental results which are 3.01 GPa and 4.09 GPa, respectively. On the other hand, the RSC models shown in Table 4.1 produce results within this experimental range and the RSC models with $C_I = 0.01$ and $\kappa = \frac{1}{10}, \frac{1}{30}$ even produce results for E_{22} within one standard deviation of the mean, that is, within the range 3.28 – 3.81 GPa. The RSC model with $C_I = 0.01$ and $\kappa = \frac{1}{5}$ lies just outside this range. Thus, one can see that the model that appears to be the most reasonable is the RSC model with an interaction coefficient of 0.01 and a strain reduction factor of 1/10.

A similar table as Table 4.1 can be made to show the absolute percent relative error in the calculated CTE. This is shown in Table 4.2, where the absolute percent relative error is calculated according to the equation

$$\varepsilon = \left| \frac{(model\ \alpha_{22}) - (experimental\ \alpha_{22})}{(experimental\ \alpha_{22})} \right| \cdot 100\% \tag{4.4}$$

where ε is the absolute percent relative error, $(model\ \alpha_{22})$ is the value of the effective longitudinal CTE calculated by a given model (from Equation (3.10)), and $(experimental\ \alpha_{22})$ is the mean value of the effective bulk longitudinal CTE that was measured in this chapter, 5.43 x 10^{-5} (1/°C).

Table 4.2 Effective longitudinal CTE, α_{22} – Error

Model Used	α_{22} (1/°C)	ε
IRD - $C_I = 0.001$	9.61 x 10^{-6}	82.31 %
IRD - $C_I = 0.01$	2.00 x 10^{-5}	63.11 %
RSC – $C_I = 0.01, \kappa = 1/5$	3.79 x 10^{-5}	31.85 %
RSC – $C_I = 0.01, \kappa = 1/10$	4.69 x 10^{-5}	13.64 %
RSC – $C_I = 0.01, \kappa = 1/30$	5.93 x 10^{-5}	8.70 %

It can be seen in Table 4.2 that the CTE predictions are not as good as the Young's Moduli predictions in Table 4.1. Nevertheless, the absolute percent relative error dramatically decreases going down Table 4.2. In addition to being the apparent most unreasonable predictor of E_{22}, the IRD with an interaction coefficient of 0.001 also appears to be the most unreasonable of the models for predicting α_{22}. As was the case for the stiffness predictions, neither of the IRD models predict values within the minimum to maximum experimental range, which was 4.46 x 10^{-5} – 7.01 x 10^{-5} (1/°C) for α_{22}. The RSC model with $C_I = 0.01$ and $\kappa = \frac{1}{5}$ is also, once again, outside one standard deviation from the mean, which is the range 4.31 x 10^{-5} – 6.56 x 10^{-5} (1/°C). Once again, the RSC models with interaction coefficients of 0.01 and strain reduction factors of 1/10 and 1/30 seem to perform the best for predicting the effective longitudinal CTE, and both produce results within one standard deviation from the mean. However, unlike the results for E_{22}, the RSC model with $C_I = 0.01$ and $\kappa = 1/30$ seems to produce slightly more reasonable results than the RSC model with $C_I = 0.01$ and $\kappa = 1/10$.

4.8 Another Method of Computing E_{22}

In Chapter Three, a computational method for calculating E_{22} and α_{22} was presented in which 3 major steps were taken: (1) COMSOL was used to solve for the flow of the polymer build material decoupled from the fiber inclusions, then (2) MATLAB was used to solve for the fiber orientation state and the resulting stiffness and CTE, and then, finally, (3) COMSOL was used again with the newly found stiffness and CTE properties to obtain E_{22} and α_{22}. In Section 4.8 for calculating E_{22}, we present a new computational method in which step 3 is eliminated completely and, instead, E_{22} is calculated with MATLAB in step 2. This is found by integrating the stiffness tensor

across the nozzle exit, dividing by the diameter of the nozzle, and then extracting the desired value E_{22} from the resulting stiffness tensor. In other words, the equation used to find the integrated stiffness across the nozzle exit is given by

$$C_{ijkl}^{exit} = \frac{1}{D}\int_{-D/2}^{D/2} C_{ijkl}(x)dx \tag{4.5}$$

where D is the nozzle diameter at the nozzle exit and C_{ijkl} is the fourth-order stiffness tensor at the nozzle exit, which is a function of x. Once C_{ijkl}^{exit} has been found in MATLAB using the trapezoidal rule, it is converted to contracted notation and inverted to get the contracted compliance tensor S_{ijkl}^{exit}. E_{22} is then found as the (2,2) component of the contracted S_{ijkl}^{exit} tensor raised to the -1 power. Using Equation (4.5), the following results presented in Table 4.3 were found for several different fiber orientation models. The error in this table was calculated using Equations (4.3).

Table 4.3 Integration Method – E_{22} with Error

Model Used	E_{22} (GPa)	ε
IRD - $C_I = 0.001$	4.86	36.97 %
IRD - $C_I = 0.01$	4.44	25.19 %
RSC – $C_I = 0.01$, $\kappa = 1/5$	3.92	10.48 %
RSC – $C_I = 0.01$, $\kappa = 1/10$	3.67	3.51 %
RSC – $C_I = 0.01$, $\kappa = 1/30$	3.37	5.07 %

The results in Table 4.3 closely match those given in Table 4.1. Discrepancies between these results could largely be due to the different numerical methods used in their computations.

4.9 Remarks

It is important to take careful note of all of the assumptions that have been made up to this point in Chapter Three and Four and bear them in mind while assessing the reasonableness of the computational models used in this thesis:

1) The nozzle geometry is modeled as a 2D, planar flow, with no lateral out-of-plane swell accounted for as well as no in-plane die swell accounted for. The upstream section of the nozzle and the turning of the extrudate as it comes into contact with the print bed are neglected and only a simplified geometry of the nozzle at its end is used. The nozzle height and bed speed are neglected.
2) The polymer melt flow is modeled as an isothermal, Newtonian fluid, decoupled from the fibers.
3) The fibers are short, rigid cylinders uniformly dispersed throughout the polymer matrix and are well bonded to the polymer matrix. They all have the same aspect ratio and are small compared to the size of the nozzle and die swell.
4) The fibers and polymer matrix are linearly elastic and their material properties are isotropic.
5) The velocity gradient change over a fiber's length is small.
6) The short-fiber composite at the inlet of the nozzle is isotropic, meaning that the initial fiber orientation state is completely random.
7) When calculating the stress in a tensile bar in order to subsequently calculate an experimental value of E_{22}, the cross-sectional area of the tensile bar is considered to be rectangular.

In this chapter, experimental work was discussed in which the large volume, bead deposition system was described. From this system, carbon fiber filled beads were produced from which tensile bars and TMA samples were taken for testing. The testing results for 33 tensile tests and 6 TMA tests gave average values of E_{22} and α_{22} of 3.55 GPa and 5.43 x 10^{-5} (1/^{o}C), respectively. These values compared well with those found by computational methods in Chapter Three. The RSC model with $C_I = 0.01$ and $\frac{1}{30} \leq \kappa \leq 1/5$ is considered to be the most reasonable predictor of the fiber orientation state within a short carbon fiber ABS composite bead fabricated with a large volume extruder (such as those used in BAAM systems) for the simplified nozzle geometry and the underlying assumptions used in this thesis.

CHAPTER FIVE

Conclusions and Future Work

The first major contribution of this thesis was the completion of a working large scale bead system for fabricating large scale one dimensional beads of carbon fiber filled ABS. This system included a Strangpresse Extruder Model 19 and a translating print bed. The main contribution to complete this system for this study was design, fabrication, and installation of a translating, heated print bed large enough to fabricate 3 foot beads. Repeated processing of beads was done in order to determine acceptable parameters for consistent bead fabrication of the investigated 13% carbon fiber filled ABS pellets. The best quality beads were generated when the extruder was set to 2250 RPM with a range of temperatures from 198°C to 210°C. Beads were fabricated with a nozzle height of 1.5 mm and a print bed speed of 50 mm/s with a print bed temperature of 65^{o}C (although 85^{o}C was seen to produce results that were perhaps even better and more consistent than 65 ^{o}C).

The second major contribution of this thesis was the development of structural and thermal testing procedures for characterizing the performance of the fabricated beads. This work included tensile tests and TMA tests to determine, respectively, the effective longitudinal Young's modulus (E_{22}) and CTE (α_{22}) of a 3D printed, anisotropic, short-fiber composite bead. The tests revealed results for E_{22} of 3.01 – 4.09 GPa from 33 samples and results for α_{22} of 2.72x10^{-5} – 7.01x10^{-5} (1/^{o}C) from 9 samples. A typical effective longitudinal Young's modulus for a sample cut from a bead was 3.55 GPa with

a standard deviation of 0.27 GPa and a typical value for the effective longitudinal CTE was 5.09×10^{-5} (1/°C) with a standard deviation of 1.27×10^{-5} (1/°C).

The third major contribution of this thesis was the implementation of three mathematical models for predicting the spatially varying fiber orientation. These included Jeffery's model [25] for suspensions without fiber interactions, and the Folgar and Tucker Isotropic Rotary Diffusion model [29] and the Reduced Strain Closure model of Wang *et al.* [1] for concentrated suspensions. Jeffery's model was shown to predict periodic oscillations of the fiber orientation state and thus could not predict steady state values of the fiber orientation state expected for the fiber filled ABS system investigated. The IRD model, based on Jeffery's model, accounts for fiber interactions and was shown to dampen the predicted periodic motion so that the fiber orientation state would reach a constant, steady state. The IRD model predicts a very fast approach to steady state which is addressed by the RSC model. The RSC model expands on the IRD model by including a strain-reduction factor to reduce the strain effects on the fiber orientation. The RSC model was seen to effectively slow down the rate at which the fibers achieve a steady orientation state.

The fourth major contribution of this study was the computational method of predicting the material properties of an anisotropic, short-fiber polymer composite bead printed with a large scale bead deposition system. This involved the following steps: (1) a simulation of the polymer melt flow through the large scale FFF nozzle in COMSOL, (2) the computation of the spatially varying fiber orientation state within the flow domain via MATLAB, (3) the calculation of the spatially varying stiffness and CTE tensors via MATLAB, and (4) the prediction of the effective longitudinal Young's modulus and CTE

in COMSOL given the spatially varying stiffness and CTE. To calculate the stiffness and CTE in step (3), the fiber orientation states from step (2) were needed as well as an appropriate micromechanics model. For this study, the micromechanics model chosen was that of Tandon and Weng [63] to determine the transversely isotropic stiffness and CTE. Once the transversely isotropic stiffness tensor was obtained an orientation averaging calculation (also called homogenization) was performed to predict the anisotropic stiffness and CTE tensors. These anisotropic stiffness and CTE tensors were then provided as inputs to a COMSOL models mimicking the physical tensile test and thermomechanical test to obtain, respectively, E_{22} and α_{22}.

The fifth and final contribution of this work is the assessment of the validity of the fiber orientation models. This study suggests the RSC model is the best of the three models that were implemented in this study based on the fact that the material property predictions using the RSC model results for orientation gave stiffness and CTE results within the bandwidth of the experimental results, whereas the IRD model did not. Since the Jeffery model is known to be less accurate than the IRD based on the fact that it discounts fiber interaction, it too lacks sufficient accuracy. It must be noted that the accuracy of the material property predictions also depend on the micromechanics model used. Thus, the accuracy of the predictions cannot be wholly attributed to (or blamed on) the fiber orientation model implemented.

In the future, there are several ways in which the accuracy of the computational methods used in this study could be improved upon. One is the coupling of the viscous polymer flow with the internal fiber orientation state as this study assumed that these were decoupled. In addition, the geometry of the polymer melt flow needs to be better

defined before high accuracy in the fiber orientation state predictions can be obtained. Including the die swell after the melt leaves the extruder and is deposited on the moving platen will modify the actual orientation state. This would be a rather significant two step process, the first would be performing the analysis on a simplified 2D domain, and the second would be to extend the work to three dimensions. A third future piece of work involves directly measuring the fiber orientation state of actual beads. This could be done with the help of an etcher and an SEM microscope. With the ability to measure the fiber orientation state directly, one could assess the validity of the fiber orientation models directly as opposed to observing the material property predictions which are also dependent on the micromechanics model used and are thus an indirect method.

BIBLIOGRAPHY

[1] Wang, J., O'Gara, J. F., and Tucker, C. L., 2008, "An Objective Model for Slow Orientation Kinetics in Concentrated Fiber Suspensions: Theory and Rheological Evidence," J. Rheol., **52**(5), pp. 1179–1200.

[2] "What Is Additive Manufacturing? | Wohlers Associates" [Online]. Available: https://wohlersassociates.com/additive-manufacturing.html. [Accessed: 31-Aug-2017].

[3] Jiang, D., 2017, "Three Dimensional Topology Optimization with Orthotropic Material Orientation Design for Additive Manufacturing Structures," Thesis, Baylor University.

[4] Love, L. J., Kunc, V., Rios, O., Duty, C. E., Elliott, A. M., Post, B. K., Smith, R. J., and Blue, C. A., 2014, "The Importance of Carbon Fiber to Polymer Additive Manufacturing," J. Mater. Res. Warrendale, **29**(17), pp. 1893–1898.

[5] Stansbury, J. W., and Idacavage, M. J., 2016, "3D Printing with Polymers: Challenges among Expanding Options and Opportunities," Dent. Mater., **32**(1), pp. 54–64.

[6] 2017, "Wohlers Report 2017 Shows Vibrant New Business Activity In 3D Printing With Slower Worldwide Growth," Jeffs MCAD Blogging [Online]. Available: https://www10.mcadcafe.com/blogs/jeffrowe/2017/05/25/wohlers-report-2017-shows-vibrant-new-business-activity-in-3d-printing-with-slower-worldwide-growth/. [Accessed: 16-Jun-2017].

[7] Sarah Anderson Goehrke, 2017, "Wohlers Report 2017: The Real Authority on 3D Printing," 3DPrintcom Voice 3D Print. Addit. Manuf.

[8] Campbell, I., Bourell, D., and Gibson, I., 2012, "Additive Manufacturing: Rapid Prototyping Comes of Age," Rapid Prototyp. J., **18**(4), pp. 255–258.

[9] Hoglund, R. M., 2016, "An Anisotropic Topology Optimization Method For Carbon Fiber-Reinforced Fused Filament Fabrication," Masters, Baylor University.

[10] Bendsoe, M. P., and Sigmund, O., 2013, *Topology Optimization: Theory, Methods, and Applications*, Springer Science & Business Media.

[11] Sigmund, O., 2001, "A 99 Line Topology Optimization Code Written in Matlab," Struct. Multidiscip. Optim., **21**(2), pp. 120–127.

[12] Orme, M. E., Gschweitl, M., Ferrari, M., Vernon, R., Madera, I. J., Yancey, R., and Mouriaux, F., 0, “Additive Manufacturing of Lightweight, Optimized, Metallic Components Suitable for Space Flight,” J. Spacecr. Rockets, **0**(0), pp. 1–10.

[13] Rengier, F., Mehndiratta, A., Tengg-Kobligk, H. von, Zechmann, C. M., Unterhinninghofen, R., Kauczor, H.-U., and Giesel, F. L., 2010, “3D Printing Based on Imaging Data: Review of Medical Applications,” Int. J. Comput. Assist. Radiol. Surg., **5**(4), pp. 335–341.

[14] Navarrete, J. I. M., Hidalgo-Salazar, M. A., Nunez, E. E., and Arciniegas, A. J. R., 2017, “Thermal and Mechanical Behavior of Biocomposites Using Additive Manufacturing,” Int. J. Interact. Des. Manuf. IJIDeM, pp. 1–10.

[15] Jones, R. M., 1998, *Mechanics Of Composite Materials*, CRC Press, Philadelphia, PA.

[16] Holshouser, C., Newell, C., Palas, S., Love, L. J., Kunc, V., Lind, R. F., Lloyd, P. D., Rowe, J. C., Blue, C. A., Duty, C. E., Peter, W. H., and Dehoff, R. R., 2013, “Out of Bounds Additive Manufacturing,” Adv. Mater. Process., **171**(3), pp. 15–17.

[17] “2017 Best 3D Printer Guide,” 3D Hubs [Online]. Available: https://www.3dhubs.com/best-3d-printer-guide. [Accessed: 29-Jun-2017].

[18] “BAAM,” Cincinnati Inc. [Online]. Available: https://www.e-ci.com/baam/. [Accessed: 29-Jun-2017].

[19] “AmericaMakes - Numerical Simulation of Big Area Additive Manufacturing (3D Printing) of a Full Size Car” [Online]. Available: https://www.americamakes.us/news-events/industry-news/item/781-numerical-simulation-of-big-area-additive-manufacturing-3d-printing-of-a-full-size-car. [Accessed: 13-Jun-2017].

[20] “BAAM 3D Printed Projects,” Cincinnati Inc. [Online]. Available: https://www.e-ci.com/baam-3d-printed-projects/. [Accessed: 29-Jun-2017].

[21] Spinnie, N., 2016, “LARGE SCALE FUSED DEPOSITION MODELING: THE EFFECT OF PROCESSING PARAMETERS ON BEAD GEOMETRY.”

[22] Spinnie, N. K., 2016, “Large Scale Fused Filament Fabrication: The Effects of Process Parameters on Bead Geometry,” Masters, Baylor University.

[23] Heller, B. P., 2015, “Effects of Nozzle Geometry and Extrudate Swell on Fiber Orientation in Fused Deposition Modeling Nozzle Flow.,” Thesis.

[24] Heller, B. P., Smith, D. E., and Jack, D. A., 2016, “Effects of Extrudate Swell and Nozzle Geometry on Fiber Orientation in Fused Filament Fabrication Nozzle Flow,” Addit. Manuf., **12**, pp. 252–264.

[25] Jeffery, G. B., 1922, “The Motion of Ellipsoidal Particles Immersed in a Viscous Fluid,” Proc. R. Soc. Lond. Ser. Contain. Pap. Math. Phys. Character, **102**(715), pp. 161–179.

[26] Sillem, A., 2010, “Fundamental Theory and Implementation of the Wang-O’Gara-Tucker Model for the Modeling of Fiber Orientation in Fiber Filled Injection Molded Thermoplastics.”

[27] Trevelyan, B. J., and Mason, S. G., 1951, “Particle Motions in Sheared Suspensions. I. Rotations,” J. Colloid Sci., **6**(4), pp. 354–367.

[28] Advani, S. G., and Tucker, C. L., 1987, “The Use of Tensors to Describe and Predict Fiber Orientation in Short Fiber Composites,” J. Rheol., **31**(8), pp. 751–784.

[29] Folgar, F., and Tucker, C. L., 1984, “Orientation Behavior of Fibers in Concentrated Suspensions,” J. Reinf. Plast. Compos., **3**(2), pp. 98–119.

[30] Cintra, J. S., and Tucker, C. L., 1995, “Orthotropic Closure Approximations for Flow-induced Fiber Orientation,” J. Rheol., **39**(6), pp. 1095–1122.

[31] Eberle, A. P. R., Vélez-García, G. M., Baird, D. G., and Wapperom, P., 2010, “Fiber Orientation Kinetics of a Concentrated Short Glass Fiber Suspension in Startup of Simple Shear Flow,” J. Non-Newton. Fluid Mech., **165**(3), pp. 110–119.

[32] Chung, D. H., and Kwon, T. H., 2002, “Fiber Orientation in the Processing of Polymer Composites,” Korea-Aust. Rheol. J., **14**(4), pp. 175–188.

[33] Phelps, J. H., and Tucker, C. L., 2009, “An Anisotropic Rotary Diffusion Model for Fiber Orientation in Short- and Long-Fiber Thermoplastics,” J. Non-Newton. Fluid Mech., **156**(3), pp. 165–176.

[34] Einstein, A., 1906, “Eine Neue Bestimmung Der Moleküldimensionen,” Ann. Phys., **324**, pp. 289–306.

[35] Zhang, D., E. Smith, D., A. Jack, D., and Montgomery-Smith, S., 2011, “Numerical Evaluation of Single Fiber Motion for Short-Fiber-Reinforced Composite Materials Processing,” J. Manuf. Sci. Eng., **133**(5), pp. 051002-051002-9.

[36] Jack, D. A., 2006, “Advanced Analysis of Short-Fiber Polymer Composite Material Behavior,” Thesis, University of Missouri--Columbia.

[37] Jack, D. A., and Smith, D. E., 2004, “Assessing the Use of Tensor Closure Methods with Orientation Distribution Reconstruction Functions,” J. Compos. Mater., **38**(21), pp. 1851–1871.

[38] Montgomery-Smith, S., Jack, D. A., and Smith, D. E., 2010, “A Systematic Approach to Obtaining Numerical Solutions of Jeffery’s Type Equations Using Spherical Harmonics,” Compos. Part Appl. Sci. Manuf., **41**(7), pp. 827–835.

[39] Jack, D. A., and Smith, D. E., 2008, “Elastic Properties of Short-Fiber Polymer Composites, Derivation and Demonstration of Analytical Forms for Expectation and Variance from Orientation Tensors,” J. Compos. Mater., **42**(3), pp. 277–308.

[40] Advani, S. G., 1987, “Prediction of Fiber Orientation during Processing of Short Fiber Composites,” Ph.D., University of Illinois at Urbana-Champaign.

[41] Doi, M., 1981, “Molecular Dynamics and Rheological Properties of Concentrated Solutions of Rodlike Polymers in Isotropic and Liquid Crystalline Phases,” J. Polym. Sci. Polym. Phys. Ed., **19**(2), pp. 229–243.

[42] Hand, G. L., 1962, “A Theory of Anisotropic Fluids,” J. Fluid Mech., **13**(1), pp. 33–46.

[43] Jack, D. A., and Smith, D. E., 2007, “The Effect of Fibre Orientation Closure Approximations on Mechanical Property Predictions,” Compos. Part Appl. Sci. Manuf., **38**(3), pp. 975–982.

[44] Jack, D. A., and Smith, D. E., 2004, “Assessing the Use of Tensor Closure Methods with Orientation Distribution Reconstruction Functions,” J. Compos. Mater., **38**(21), pp. 1851–1871.

[45] Wetzel, E. D., 1999, “Modeling Flow-Induced Microstructure of Inhomogeneous Liquid-Liquid Mixtures,” Ph.D., University of Illinois at Urbana-Champaign.

[46] VerWeyst, B. E., Tucker, C. L., Foss, P. H., and O’Gara, J. F., 1999, “Fiber Orientation in 3-D Injection Molded Features,” Int. Polym. Process., **14**(4), pp. 409–420.

[47] Verleye, V., Couniot, A., and Dupret, F., 1994, “Numerical Prediction Of Fibre Orientation In Complex Injection-Moulded Parts,” WIT Trans. Eng. Sci., **4**, p. 10.

[48] Montgomery-Smith, S., Jack, D., and Smith, D. E., 2011, “The Fast Exact Closure for Jeffery’s Equation with Diffusion,” J. Non-Newton. Fluid Mech., **166**(7), pp. 343–353.

[49] Yamane, Y., Kaneda, Y., and Dio, M., 1994, “Numerical Simulation of Semi-Dilute Suspensions of Rodlike Particles in Shear Flow,” J. Non-Newton. Fluid Mech., **54**, pp. 405–421.

[50] Bay, R. S., 1991, “Fiber Orientation in Injection-Molded Composites: A Comparison of Theory and Experiment,” Ph.D., University of Illinois at Urbana-Champaign.

[51] Chung, D. H., and Kwon, T. H., 2002, “Invariant-Based Optimal Fitting Closure Approximation for the Numerical Prediction of Flow-Induced Fiber Orientation,” J. Rheol., **46**(1), pp. 169–194.

[52] Wang, J., and Jin, X., 2010, “Comparison of Recent Fiber Orientation Models in Autodesk Moldflow Insight Simulations with Measured Fiber Orientation Data,” Polym. Process. Soc. 26th Annu. Meet.

[53] Tucker, C. L., and Liang, E., 1999, “Stiffness Predictions for Unidirectional Short-Fiber Composites: Review and Evaluation,” Compos. Sci. Technol., **59**(5), pp. 655–671.

[54] Eshelby, J. D., 1957, “The Determination of the Elastic Field of an Ellipsoidal Inclusion, and Related Problems,” Proc. R. Soc. Lond. Ser. Math. Phys. Sci., **241**(1226), pp. 376–396.

[55] Mori, T., and Tanaka, K., 1973, “Average Stress in Matrix and Average Elastic Energy of Materials with Misfitting Inclusions,” Acta Metall., **21**(5), pp. 571–574.

[56] Benveniste, Y., 1987, “A New Approach to the Application of Mori-Tanaka’s Theory in Composite Materials,” Mech. Mater., **6**(2), pp. 147–157.

[57] Weng, G. J., 1992, “Explicit Evaluation of Willis’ Bounds with Ellipsoidal Inclusions,” Int. J. Eng. Sci., **30**(1), pp. 83–92.

[58] Cox, H. L., 1952, “The Elasticity and Strength of Paper and Other Fibrous Materials,” Br. J. Appl. Phys., **3**(3), p. 72.

[59] Hill, R., 1965, “A Self-Consistent Mechanics of Composite Materials,” J. Mech. Phys. Solids, **13**(4), pp. 213–222.

[60] Budiansky, B., 1965, “On the Elastic Moduli of Some Heterogeneous Materials,” J. Mech. Phys. Solids, **13**(4), pp. 223–227.

[61] Halpin, J. ., Affdl, J. C. H., and Kardos, J. ., 1976, “The Halpin-Tsai Equations: A Review,” Polym. Eng. Sci., **16**(5), pp. 344–352.

[62] Hill, R., 1963, “Elastic Properties of Reinforced Solids: Some Theoretical Principles,” J. Mech. Phys. Solids, **11**(5), pp. 357–372.

[63] Tandon, G. P., and Weng, G. J., 1984, “The Effect of Aspect Ratio of Inclusions on the Elastic Properties of Unidirectionally Aligned Composites,” Polym. Compos., **5**(4), pp. 327–333.

[64] Zhang, C., 2011, “Modeling of Flexible Fiber Motion and Prediction of Material Properties,” Masters, Baylor University.

[65] Lielens, G., Pirotte, P., Couniot, A., Dupret, F., and Keunings, R., 1998, “Prediction of Thermo-Mechanical Properties for Compression Moulded Composites,” Compos. Part Appl. Sci. Manuf., **29**(1), pp. 63–70.

[66] Lewis, T. B., and Nielsen, L. E., 1970, “Dynamic Mechanical Properties of Particulate-Filled Composites,” J. Appl. Polym. Sci., **14**(6), pp. 1449–1471.

[67] Nielsen, L. E., 1970, “Generalized Equation for the Elastic Moduli of Composite Materials,” J. Appl. Phys., **41**(11), pp. 4626–4627.

[68] Ingber, M. S., and Papathanasiou, T. D., 1997, “A Parallel-Supercomputing Investigation of the Stiffness of Aligned, Short-Fiber-Reinforced Composites Using the Boundary Element Method,” Int. J. Numer. Methods Eng., **40**(18), pp. 3477–3491.

[69] Camacho, C. W., Tucker, C. L., Yalvaç, S., and McGee, R. L., 1990, “Stiffness and Thermal Expansion Predictions for Hybrid Short Fiber Composites,” Polym. Compos., **11**(4), pp. 229–239.

[70] Schapery, R. A., 1968, “Thermal Expansion Coefficients of Composite Materials Based on Energy Principles,” J. Compos. Mater., **2**(3), pp. 380–404.

[71] Halpin, J. C., 1969, “Stiffness and Expansion Estimates for Oriented Short Fiber Composites,” J. Compos. Mater., **3**(4), pp. 732–734.

[72] Stair, S., and Jack, D. A., 2015, “Comparison of Experimental and Modeling Results for Cure Induced Curvature of a Carbon Fiber Laminate,” Polym. Compos., p. n/a-n/a.

[73] “Strangpresse Extruders | Strangpresse.”

[74] Tucker III, C. L., 2005, “Personal Communication.”

[75] “Modulus of Elasticity or Young’s Modulus - and Tensile Modulus for Common Materials” [Online]. Available: http://www.engineeringtoolbox.com/young-modulus-d_417.html. [Accessed: 02-Aug-2017].

[76] “Coefficients of Linear Thermal Expansion” [Online]. Available: http://www.engineeringtoolbox.com/linear-expansion-coefficients-d_95.html. [Accessed: 02-Aug-2017].

[77] “Specifications for Common Plastic Molding Design Material | Engineers Edge” [Online]. Available: http://www.engineersedge.com/plastic/materials_common_plastic.htm. [Accessed: 02-Aug-2017].

[78] “PolyOne Stat-Tech™ AS-13CF/000 Black Acrylonitrile Butadiene Styrene (ABS)” [Online]. Available: http://www.matweb.com/search/datasheet.aspx?matguid=59f0e0a398da4c99b6039a46bfcf93d1&ckck=1. [Accessed: 02-Aug-2017].

[79] “Volume-Weight Fraction - Calculators - NetComposites Now” [Online]. Available: http://netcomposites.com/guide-tools/tools/calculators/volume-weight-fraction/. [Accessed: 02-Aug-2017].

[80] Ehrenstein, G. W., 2001, *[(Polymeric Materials: Structure - Properties - Applications)]*, Hanser Gardner Publications.

[81] “Density, Weight and Volume Fractions - CompositeMaterialsDesign” [Online]. Available: https://sites.google.com/site/compositematerialsdesign/home/weight-and-volume-fractions. [Accessed: 02-Aug-2017].

[82] George, C., 2017, “Personal Communication.”